BIOSYNTHETIC MATERIALS FOR PRO-REGENERATIVE IMMUNE MODULATION

A Dissertation
Presented to
The Academic Faculty

by

Jack R. Krieger

In Partial Fulfillment
of the Requirements for the Degree
Doctor of Philosophy in the
Wallace H. Coulter Department of Biomedical Engineering

Georgia Institute of Technology
Emory University
August 2017

BIOSYNTHETIC MATERIALS FOR PRO-REGENERATIVE IMMUNE MODULATION

Approved by:

Dr. Edward Botchwey, Advisor
Wallace H. Coulter Department of
Biomedical Engineering
Georgia Institute of Technology

Dr. Johnna Temenoff
Wallace H. Coulter Department of
Biomedical Engineering
Georgia Institute of Technology

Dr. Steven Goudy
Department of Otolaryngology in the
School of Medicine
Emory University

Dr. Gabe Kwong
Wallace H. Coulter Department of
Biomedical Engineering
Georgia Institute of Technology

Dr. Luke Mortensen
Regenerative Bioscience Center
University of Georgia

Date Approved: 23 May 2017

ACKNOWLEDGMENTS

I want to start by thanking my thesis advisor, Edward Botchwey, for accepting a green 22-year-old with a physics degree, minimal training in bioscience research, and no funding. I will always be grateful to Ed for giving me the trust, patience, and support that enabled this accomplishment. I am thankful for the many ways Ed helped me grow intellectually and professionally. My favorite characteristic of Ed's lab is his emphasis on team-mindedness and collaboration, which makes the long hours more enjoyable and the research more effective. I was lucky to collaborate with Dr. Molly Ogle, whose invaluable mentorship helped me turn the corner in my graduate career. I want to thank the rest of the current Botchwey lab—Claire Olingy, Cheryl San Emeterio, Nathan Chiappa, Caitlin Sok, Jada Selma, Dr. Hannah Song—for their smart conversations and advice, their generosity with assistance and snacks, their willingness to listen to me complain, and their patience with my inability to find anything ever. I thank the relentlessly-cheery alumna Tiffany Wang as well as the impeccably-dressed alumnus Dr. Tony Awojoodu, whose counsel helped me land an offer at my dream first job.

I want to thank my thesis committee—Drs. Johnna Temenoff, Gabe Kwong, Luke Mortensen, and Steve Goudy—for their time, insight, and constructive feedback. I want to express particular appreciation to Dr. Temenoff for being an excellent collaborator and complementing our style perfectly. Thanks to Liane Tellier and Jennifer McFaline-Figueroa of the Temenoff lab for their willingness to share ideas, techniques, and subtle jokes.

Thanks to the staff in BME, PRL, and IBB for allowing our research community to operate smoothly. In particular, I want to acknowledge Nadia Bogulslavsky and Andrew Shaw for their training and support in the flow cytometry and microscopy core facilities, where I spent innumerable hours in the dark. Special thanks to the ebullient Michelle Wong for generously coaching me through job interview preparation.

Lastly, I want to thank the people who make life worth living—my family and friends. I owe everything to my parents, whose genes, values, and love helped shaped me into a man I am proud to see in the mirror. Thanks to my dad for guiding my intellectual passion toward science, and to my mom for instilling perseverance that is critical to research. My older siblings were a constant source of love and fun growing up. Special thanks to my brother Ben for being my best friend and trusted confidante, and to my sister Sarah for being a source of family love in Atlanta. Thanks to my girlfriend, Megan Larsh, who makes me laugh and smile every day, sympathizes with my frustrations, and builds me up when I am down. Lastly, thank you to the crew at 1208 W. Peachtree—Michael Spear, Jay Clark, and Olivia Leach—for showing me what profound friendship feels like.

TABLE OF CONTENTS

LIST OF FIGURES

LIST OF SYMBOLS AND ABBREVIATIONS

FKN	Fractalkine
SDF-1α	Stromal derived factor-1α
ELISA	Enzyme linked immunosorbent assay
S1P	Sphingosine 1-phosphate
S1PR3	Sphingosine 1-phoshpate receptor 3
PEGDA	Poly(ethylene glycol) diacrylate
Hep^{-N}	N-desulfated heparin
APS	Ammonium persfulate
TEMED	N,N,N',N'-trimethylene diamine
CS	Complementary sequence
IHC	Immunohistochemistry
MP	Mononuclear phagocyte
MΦ	Macrophage
MO	Monocyte
DC	Dendritic cell
T_H	Helper T lymphocyte
T_{reg}	Regulatory T lymphocyte
Clod-lip	Clodronate liposomes
GFP	Green fluorescent protein
RCT	Rotator cuff tear
SS	Supraspinatus
TT	Tendon transection

DN	Denervation
IGF-1	Insulin-like growth factor-1
bFGF	Basic fibroblast growth factor

SUMMARY

The mononuclear phagocyte system underlies the host response to myriad tissue injuries and thus represents a powerful therapeutic target to potentially augment healing in numerous clinical indications with unmet need. Mononuclear phagocytes, particularly monocytes and macrophages that infiltrate sites of sterile injury, are comprised of highly heterogeneous subpopulations with distinct functions and infiltration kinetics. Classical monocytes and classically-activated "M1" macrophages are generally "inflammatory" subpopulations that accumulate early, whereas non-classical monocytes and alternatively-activated "M2" macrophages accumulate later and are generally "regenerative. Although M2 macrophages have received considerable attention as regenerative mediators, non-classical monocytes are a novel cellular target for regenerative therapies.

Our overarching goal is to effectively control the trafficking and function of circulating non-classical monocytes to enhance tissue repair. The objectives of this research are (i) to enhance the recruitment of non-classical monocytes to stimulate angiogenesis and arteriogenesis, processes critical to regeneration of vascularized tissues; (ii) to investigate synergy between immune-modulating molecules in non-classical monocyte recruitment and tissue vascularization; and (iii) to investigate the relationship between immune cell infiltration and rotator cuff injury-induced muscle degeneration. Implantable biosynthetic materials are powerful tools to achieve these objectives by enabling control over the spatial and temporal presentation of immune-modulating factors within an injury site.

To accomplish aim (i), we develop two novel PEGDA-based materials that control distinct chemokine signals locally within skin wounds. We show that PEGDA hydrogels functionalized with fractalkine-specific DNA aptamers can enrich endogenous fractalkine and increase accumulation of non-classical monocytes and M2 macrophages within skin wounds. Moreover, PEGDA hydrogels functionalized with a heparin derivative can encapsulate and release stromal derived factor-1a to achieve highly localized recruitment of non-classical monocytes and enhancement of tissue vasclarization. In aim (ii), we show that dual release of stromal derived factor-1α and the sphingosine analog FTY720 from heparin-PEGDA hydrogels causes synergistic accumulation of M2 macrophages and arteriogenesis. To achieve aim (iii), we use a murine model of severe rotator cuff injury to show that mononuclear phagocytes, particularly non-classical subpopulations, infiltrate supraspinatus muscle after injury, and that circulating monocytes contribute to supraspinatus degeneration. In contrast to results from aim (ii), we show that local delivery of FTY720 recruits inflammatory subpopulations of mononuclear phagocytes.

The research presents novel biosynthetic materials that may aid soft tissue regeneration by recruiting pro-regenerative subpopulations of mononuclear phagocytes and stimulating vascularization. The work helps elucidate the role of chemokine signals in the recruitment and function of mononuclear phagocytes in soft tissue wounds. The study is the first to quantitatively analyze the infiltration of immune cell subpopulations after rotator cuff injury and demonstrate the role of monocytes in rotator cuff muscle degeneration.

1. INTRODUCTION AND SPECIFIC AIMS

Harnessing endogenous immune-mediated mechanisms of repair is a promising strategy to augment healing after traumatic or ischemic injury to myriad tissues. The innate immune system's response to tissue injury is characterized by infiltration of mononuclear phagocytes, which orchestrate repair by clearing debris, remodeling extracellular matrix, facilitating growth of new and existing blood vessels, and signaling to circulating and parenchymal cells that help restore the native tissue composition. Mononuclear phagocytes are comprised of highly heterogeneous subpopulations that exert divergent effects on injured tissue during pathogenesis and regeneration. Dominant presence of non-classical monocytes and alternatively-activated M2 macrophages over classical monocytes and classically-activated M1 macrophages is associated with superior healing outcomes.

Implantable drug-eluting biomaterials represent promising platforms for immune-regenerative strategies because controlled drug delivery can facilitate spatial and temporal control over presentation of biological factors within injured tissue. The *overarching goal* of this research is to develop implantable materials that induce pro-regenerative immune cell responses within injured tissue by controlling the recruitment and activity of non-classical monocytes. The *overarching hypothesis* of this research is that biomaterial-mediated recruitment of non-classical monocytes enhances soft tissue repair. We evaluate the ability of two novel hydrogel platforms to enhance monocyte-assisted angiogenesis using the dorsal skin window chamber model of excisional skin injury, which enables concomitant assessment of immune cell recruitment and vascular remodeling. Moving toward a musculoskeletal indication with significant unmet clinical need, we investigate

the role of mononuclear phagocytes in rotator cuff muscle degeneration and evaluate the ability of drug delivery strategies to generate pro-regenerative immune responses and inhibit muscle degeneration.

Aim 1. Evaluate monocyte recruitment and vascularization of injured skin in response to manipulation of chemokine signals using biosynthetic materials.

Non-classical monocytes express high surface levels of CX3CR1 and CXCR4 chemokine receptors compared to classical monocytes and thus migrate up gradients of the cognate ligands fractalkine (FKN) and stromal derived factor-1α (SDF-1α). The objective of this aim is to develop and evaluate biosynthetic materials to harness the FKN-CX3CR1 and SDF-1α-CXCR4 signaling axes to recruit non-classical monocytes. First, we *hypothesize* that PEGDA hydrogels functionalized with FKN-specific DNA aptamers enrich endogenous FKN and recruit non-classical monocytes to injured skin. To address the hypothesis, aptamers and aptamer-functionalized hydrogels ("aptagels") are evaluated for their ability to bind and release mouse FKN *in vitro* using surface plasmon resonance and ELISA. To evaluate effects *in vivo*, aptagels are implanted in the mouse dorsal skin window model. Endogenous FKN enrichment is measured by ELISA, and mononuclear phagocyte recruitment is measured by flow cytometry and confocal intra-vital microscopy. Next, we *hypothesize* that on-site SDF-1α delivery from N-desulfated heparin-functionalized PEGDA hydrogels (Hep^{-N}-PEGDA) recruits non-classical monocytes and stimulates angiogenesis in injured skin. Hep^{-N} functionalization combines the growth factor sequestration and protection activity of heparin with the reduced anticoagulant activity afforded by N-desulfation. After assessing bioactivty of SDF-1α released from Hep^{-N}-

PEGDA hydrogels *in vitro*, gels are implanted in the mouse dorsal skin window model. Early recruitment of bone marrow-derived cells is assessed using GFP^+ bone marrow chimeras and whole mount immunofluorescence. Mononuclear phagocyte recruitment is evaluated at multiple time points using complementary methods including flow cytometry, intra-vital microscopy, and whole-mount immunofluorescence. Concomitant angiogenesis and arteriolar expansion are assessed using whole-mount immunofluorescence and intra-vital brightfield microscopy.

Aim 2. Investigate synergy between chemokine and sphingolipid signals in achieving non-classical monocyte recruitment and vascularization of injured skin.

Previous results from our lab and others suggest that dual stimulation of CXCR4 and S1PR3 signaling axes may act synergistically to enhance the migration and pro-regenerative activity of non-classical monocytes/macrophages. To investigate suspected synergy, we engineered a dual-affinity heparin-based biosynthetic hydrogel to co-release SDF-1α and the S1PR3-targeted small molecule FTY720. The hydrogel exploits the growth factor binding activity of heparin in tandem with the lipid chaperone activity albumin to encapsulate two molecules with disparate physicochemical properties. We *hypothesize* that dual release of SDF-1α and FTY720 from Hep^{-N}-PEGDA hydrogels synergistically enhances non-classical monocyte recruitment and tissue vascularization. First, we assess migration of bone marrow-derived cells toward SDF-1α and FTY720 released from Hep^{-N}-PEGDA hydrogels *in vitro*. Gels are implanted in the mouse dorsal skin window model as in Aim 1. Mononuclear phagocyte recruitment is evaluated at multiple time points using complementary methods including flow cytometry, intra-vital

microscopy, and whole-mount immunofluorescence. Concomitant angiogenesis and arteriolar expansion are assessed using whole-mount immunofluorescence and intra-vital brightfield microscopy.

Aim 3. Investigate the relationship between immune cell infiltration and rotator cuff muscle degeneration.

Muscle degeneration caused by rotator cuff injury is a significant clinical problem that lacks effective treatments and understanding of the underlying pathogenesis. Growing evidence suggests that immune cell infiltration may contribute to rotator cuff muscle degeneration. The *objective* of this aim is two-fold: to elucidate the role of immune cell infiltration in supraspinatus degeneration, and to evaluate drug delivery strategies for generating a protective immune response. We *hypothesize* that infiltration of classical mononuclear phagocyte subpopulations contributes to muscle degeneration after rotator cuff injury. To address the hypothesis, we utilize a murine model of severe rotator cuff injury. Infiltration of innate and adaptive immune cell subpopulations are measured by flow cytometry and the cytokine milieu is assessed by multiplex immunoassay. The role of circulating monocytes in supraspinatus degeneration is evaluated by depleting monocytes with liposomal clodronate. Lastly, we locally deliver SDF-1α and FTY720 to injured supraspinatus and assess the effect on immune cell recruitment, cytokine production, and muscle degeneration.

2. BACKGROUND

2.1. The mononuclear phagocyte system underlies the host response tissue injury

The innate immune system plays a central role in the body's response to numerous, diverse injuries that cost lives, decrease quality of life, and burden the healthcare economy. Development of novel therapeutic interventions that leverage endogenous immune-mediated mechanisms of repair may accelerate or augment healing after traumatic injury to musculoskeletal[1], nervous[2-5], and cutaneous tissues[6, 7] and ischemic injury to cardiac[8] and nervous tissues[9]. The immune response to sterile injury and tissue trauma is characterized by the infiltration of mononuclear phagocytes to clear debris, remodel extracellular matrix and vasculature, and signal to circulating and parenchymal cells that help restore the native cellular and matrix composition[10, 11]. Loss of function studies show that early mononuclear phagocyte input is necessary for regeneration of amputated salamander limbs[12] and zebrafish tail fins[13], suggesting that mononuclear phagocytes orchestrate complex regeneration programs requiring the coordination of multiple tissues types.

2.2. Origin of mononuclear phagocytes in tissue injury

Sterile injury causes inflammation and the associated accumulation of macrophages. Expansion of the macrophage pool during inflammation is driven by differentiation from infiltrating monocytes[14, 15] and/or proliferation of tissue-resident macrophages[16, 17]. Tissue-resident macrophages are derived from either adult monocytes during homeostasis,

or embryonic origins[18]. Embryonically-sourced macrophages may stem from yolk-sac endothelium, fetal liver monocytes, and erythroid-myeloid progenitors and have been identified in heart, lung, brain, skin, and liver. Origins of macrophage populations during inflammation are highly context dependent. T_H2-linked infection is characterized by proliferation of tissue-resident macrophages rather than monocyte recruitment[16], whereas macrophage accumulation in damaged muscle is supplied by infiltrating monocytes[1]. The relationship between macrophage origin and function is minimally understood, but recent studies highlight functional differences that may inform future design of immune-regenerative strategies. Alternatively-activated macrophages derived from monocytes, but not those derived from tissue-resident pools, drive differentiation of $CD4^+$ T lymphocytes to Foxp3+ regulatory T lymphocytes[19], which are implicated in skeletal muscle regeneration[20]. Monocyte-derived macrophages may possess increased reparative potential compared to tissue-resident macrophages.

2.3. Mononuclear phagocyte subpopulations and effector functions

The mononuclear phagocyte system's responses to sterile injury primarily involves monocytes and macrophages, both of which are comprised of highly heterogeneous subpopulations that exert divergent effects on injured tissue during pathogenesis and regeneration. Macrophage phenotype and function is described as spectrum of M1 "inflammatory" to M2 "alternatively-activated" or "regenerative" macrophages[11]. M1 polarization from naive macrophages *in vitro* is accomplished by stimulation with IFNγ, lipopolysaccharide, and/or TNFα[21]. M1 produce reactive oxygen species and many inflammatory cytokines that support necrotic tissue clearance, and growth factors such as

VEGF and FGF2[22-25] upon stimulation. Over-activation or excessive persistence of M1 macrophages can contribute to tissue damage[11].

M2 macrophages can be further subdivided into M2a, M2b, and M2c. M2a polarization requires IL-4 and/or IL-13 in vitro. M2a (CD206 high) support extracellular matrix deposition and epithelial wound closure via high expression of arginase-1, which allows them to generate precursors for collagen and fibroblast stimulating factor[11]. M2b polarization requires immune complexes combined with toll-like receptor (TLR) or IL-1R ligands, whereas M2c macrophages arise via IL-10 stimulation[26]. M2b and M2c contribute to suppressing inflammation through secretion of IL-10. Due to macrophage plasticity *in vivo* and lack of distinguishing biomarkers, specific functions of M2a-c subtypes in tissue repair remain poorly understood. Nevertheless, the dominant presence of M2 versus M1 macrophages is associated with positive healing outcomes in numerous contexts[2, 6, 10, 27, 28].

Circulating blood monocytes are comprised of at least two functionally distinct subsets. Classical "inflammatory" monocytes are characteristically $Ly6C^{hi}$ $CCR2^{hi}$ $CX3CR1^{lo}$ in mice and $CD14^{+}CD16^{-}$ in humans. Non-classical "anti-inflammatory: monocytes are $Ly6C^{lo}$ $CCR2^{lo}$ $CX3CR1^{hi}$ in mice and $CD14^{lo}CD16^{+}$ in humans. Classical monocytes predominate the acute phases of injury, secrete inflammatory cytokines such as IL-6, iNOS, and TNFα[29], produce high levels of matrix metalloproteinases and cathepsins, and phagocytose debris[8], whereas non-classical monocytes predominate in later phase inflammation, secrete higher levels of VEGF, TGFβ, and IL-10 and lower levels of TNFα and IL-1β, and promote angiogenesis and matrix deposition[8, 30]. While studies of toxin-induced muscle injury[1], acute liver injury[31], and autoimmune disease[32]

show that classical monocytes are recruited from circulation and subsequently convert *in situ* into non-classical monocytes and M1 or M2 macrophages, other studies in myocardial infarction[8] and excisional skin injury[6] indicate that non-classical monocytes can be recruited directly from blood. Until recently, it was unknown whether non-classical versus classical monocytes give rise to distinct macrophage phenotypes. Our group is the first to show that non-classical monocytes recruited from blood may serve as biased progenitors of M2 macrophages[33].

2.4. Monocyte trafficking

At steady state, classical monocytes persist for approximately 19 hours before converting to non-classical monocytes, which persist for approximately 2 days. One study suggests that differentiation is unidirectional and non-classical monocytes do not give rise to classical monocytes[34]. Non-classical monocytes "patrol" the endothelium during homeostasis owing to their unique adhesion molecule signature, including low CD62L (L-selectin)[35] and high LFA-1 (αLβ2 integrin)[36, 37]. In contrast, classical monocytes are sparsely present on the endothelium during homeostasis. Following tissue injury, classical monocytes rapidly mobilize from the spleen and/or bone marrow into blood circulation using the CCR2 chemokine receptor[38, 39]. Classical monocytes adhere to inflamed endothelium using their high expression of CD62L, Mac-1 (αMβ2 integrin), and VLA-4 (α4β1 integrin), and then migrate up gradients of inflammatory chemokines such as MCP-1 (CCL2) using high expression of CCR2 and CCR5 chemokine receptors[35-37, 40, 41].

Differential expression of chemokine receptors between monocyte subpopulations represents a therapeutic lever for selecting recruiting non-classical monocytes. Non-

classical monocytes exhibit higher expression of CX3CR1[34, 42], C-X-C chemokine receptor type 4 (CXCR4)[27, 42], and sphingosine 1-phosphate receptor 3 (S1PR3)[6] compared to classical monocytes. As such, non-classical monocytes exhibit greater *in vitro* chemotaxis toward fractalkine (CX3CL1)[42], the cognate ligand of CX3CR1, and stromal derived factor 1-alpha (SDF-1α)[6], the ligand of CXCR4. Moreover, SDF-1α-induced chemotaxis of non-classical monocytes is enhanced by pretreatment with the S1PR3-targeting small molecule FTY720. Local delivery of FTY720 selectively increases recruitment of non-classical monocytes to injured skin[6]. Whether the CXCR4 and CX3CR1 signaling axes can also be harnessed to recruit non-classical monocytes is the subject of the present studies.

2.5. Role of mononuclear phagocytes in musculoskeletal wound healing

2.5.1. Leukocyte-assisted angiogenesis and arteriogenesis

Mononuclear phagocytes support vascular network growth and remodeling during development, homeostasis, and repair[6, 43-53]. Loss-of-function studies show that depletion of monocytes/macrophages inhibits arteriogenic recovery of perfusion following hindlimb ischemia[43], and bone-marrow deletion of CCR2, a monocyte chemokine receptor critical for mobilization, inhibits arteriolar remodeling in the dorsal skin window model[44]. Gain-of-function studies show that local delivery of CCL2, CXCL1, or exogenous macrophages increases the local pool of mononuclear phagocytes and enhances arteriogenesis and recovery of perfusion in the ischemic hindlimb[45-47]. In the context of angiogenesis, loss-of-function studies show that mononuclear phagocytes promote

vascular anastomosis[48, 49] and vessel outgrowth[50, 54]. During vascular remodeling, mononuclear phagocytes are recruited to perivascular positions that may facilitate their pro-angiogenic and pro-arteriogenic interactions with the vasculature[30, 48, 55]. Perivascular monocytes and macrophages contribute paracrine signals to the remodeling vasculature, including secretion of growth factors such as platelet-derived growth factor (PDGF) and VEGF, as well as matrix-remodeling enzymes such as MMPs that create paths for new vessels[8, 30, 45, 48, 50, 51, 55]. Although it remains controversial whether monocyte/macrophage subpopulations differentially impact vascular remodeling[22, 23, 56], literature generally associates augmented arteriogenesis and angiogenesis with recruitment of Ly-6C^{lo} non-classical monocytes and M2-like macrophages[6, 10, 26, 52, 57].

2.5.2. Mononuclear phagocytes orchestrate muscle repair

Regeneration of injured skeletal muscle is accomplished by muscle progenitor cells ("satellite cells") that differentiate into muscle fibers in a process dependent on cues from mononuclear phagocytes[58]. Skeletal muscle possesses few tissue-resident macrophages and expansion of the mononuclear phagocyte pool within injured muscle requires input from circulating monocytes[1]. Monocytes and macrophages are recruited acutely to damaged muscle where they remain until completion of repair[1, 59, 60]. Monocyte recruitment is required for natural muscle repair; multiple studies show that depletion of circulating monocytes causes incomplete and fibrotic healing of skeletal muscle after toxin-induced injury[1, 59, 60].

Monocyte subpopulations infiltrate injured muscle in sequential phases. Classical Ly6C^{hi} monocytes accumulate early and peak in number around one day after injury, whereas non-classical Ly6C^{lo} monocyte numbers rise thereafter and return to baseline upon completion of regeneration[1]. Monocytes may execute effector functions as bona-fide monocytes or as monocyte-derived macrophages[1, 24, 30, 61]. M1-like macrophages predominate the early phase, respond to tissue damage signals, and upregulate genes associated with alarmins and acute inflammatory-phase proteins[62]. M2-like macrophages predominate the later phase, supply insulin-like growth factor (IGF-1) required for muscle regeneration[63], and highly express genes governing extracellular matrix (ECM) proteins and ECM remodeling proteins[62]. Macrophage subpopulations exert differential, complementary effects on myogenic precursor cells *in vitro* via paracrine mechanisms[61]. M1-like macrophages secrete factors that stimulate myogenic precursor cell proliferation and migration, whereas M2-like macrophages stimulate myogenic differentiation and myotube fusion[1, 61]. Taken together, these results suggest that coordination between subpopulations of monocytes/macrophage orchestrates skeletal muscle repair.

2.5.3. Mononuclear phagocytes may regulate rotator cuff muscle pathogenesis

Evidence from RCT and chronic muscle pathologies suggests that inflammation, particularly mononuclear phagocyte (MP) infiltration, contributes to muscle degeneration. Pro-inflammatory cytokines such as TNFα and IL-6 stimulate apoptosis of myocytes and catabolism of intramyocellular proteins[64, 65], thus causing muscle atrophy in cancer

cachexia and autoimmune disorders. Classical "pro-inflammatory" subpopulations of mononuclear phagocytes secrete more pro-inflammatory cytokines compared to non-classical alternatively-activated subpopulations[8, 11, 22-24], suggesting that intramuscular infiltration of classical subtypes may promote chronic muscle degeneration. Indeed, in the *mdx* mouse model of Duchenne muscular dystrophy, chronic muscle degeneration is in part caused by the classical pro-inflammatory Ly6C^{hi} subset of circulating monocytes (MO)[66]. Human and rodent muscles undergoing fatty degeneration after RCT show dramatic co-localization of fat-rich regions with macrophages (MΦ) that contain intracellular lipid droplets[67, 68]. Rotator cuff muscle degeneration is exacerbated by administration of lysophosphatidic acid, whereby MΦ accumulation and TNFα expression are increased[69]. Taken together, these studies suggest that pro-inflammatory mononuclear phagocytes promote chronic muscle degeneration.

3. MONOCYTE RECRUITMENT AND VASCULARIZATION OF INJURED SKIN IN RESPONSE TO MANIPULATION OF CHEMOKINE SIGNALS USING BIOSYNTHETIC MATERIALS[1]

3.1. Abstract

3.2. Introduction

Anti-inflammatory and regenerative effects of non-classical monocytes ($Ly6C^{lo}CX3CR1^{hi}$) and M2-like macrophages ($CD206^{+}$) have been described in numerous and diverse contexts including myocardial infarction[8], vascular network expansion[6, 26, 52, 57], musculoskeletal injury[1], dermal wounds[7], central and peripheral nervous system injury[2-5, 70-72], and integration of cell, tissue, and biomaterial constructs[10, 73, 74]. Approaches to promote regenerative responses via mononuclear phagocytes can include polarizing macrophages towards an M2-like phenotype with cytokines (e.g. IL-4, IL-10)[2, 75], stimulating proliferation of tissue-resident M2-like macrophages, or recruiting circulating non-classical monocytes which differentiate preferentially into M2-like macrophages[33]. The present study evaluates novel biomaterial-based strategies to selectively recruit non-classical monocytes by leveraging their high surface expression of the chemokine receptors CX3CR1 and CXCR4[34, 76, 77].

CX3CR1 is the cognate receptor of fractalkine (FKN; CX3CL1), a 373 amino-acid cytokine with a small (8.6 kD) soluble chemotactic domain that can dissociate and signal

[1] Adapted from: J.R. Krieger, M.E. Ogle, J. McFaline-Figueroa, C.E. Segar, J.S. Temenoff, E.A. Botchwey, Spatially localized recruitment of anti-inflammatory monocytes by SDF-1alpha-releasing hydrogels enhances microvascular network remodeling, Biomaterials 77 (2016) 280-90. Reprinted by permission of Elsevier.

through CX3CR1[78]. Elevated FKN and CX3CR1^{+} cell recruitment[70] are associated with improved healing after brain injury in rodents[79, 80] and humans[81, 82]. To target the FKN-CX3CR1 axis via engineered enrichment of FKN within injured tissue, we designed aptamer-functionalized hydrogels ("aptagels") that catch and release endogenous FKN. Aptamers are single-stranded DNA or RNA oligomers that specifically bind biomolecular targets via non-covalent interactions[83]. Aptamers can be easily modified to tune binding kinetics, enable immobilization onto a surface, and mitigate enzyme-mediated degradation[84-88]. Aptamers are versatile tools used in the diagnosis and treatment of diseases, and employed in the identification and purification of targets[89-93]. Multiple clinical trials of aptamer-based therapeutics are underway and demonstrate promising safety profiles[94-96]. In this study, FKN-aptamer binding kinetics with FKN variants are assessed and aptagels are fabricated by immobilizing modified aptamers to poly(ethylene glycol) diacrylate (PEGDA). Aptagels are tested for their ability to catch and release FKN *in vitro* and recruit non-classical monocytes and M2-like macrophages to injured tissue *in vivo*.

Delivery of exogenous FKN has been attempted previously to modulate inflammation[79, 97-99]. However, delivery of exogenous proteins poses problems of short half-life[100-103], suboptimal efficacy[104], risk of immune reactions[105-107], batch-to-batch variabilities, and high costs. Enrichment of endogenous FKN may circumvent these critical hurdles to clinical translation by concentrating therapeutic proteins at the injury site, exploiting the efficacy of endogenous signaling pathways, not introducing anomalous structures or glycosylation patterns; and mitigating cost, manufacturing and regulatory hurdles.

CXCR4 is the cognate receptor of stromal derived factor-1α (SDF-1α; CXCL12), a CXC family chemokine that is increased in tissue after injury and mediates the recruitment of innate immune cells that directly and indirectly participate in the growth of microvascular networks. CXCR4 is highly expressed on immune cells and several known adult stem/progenitor cell sources, including mesenchymal stem cells, hematopoietic stem cells, and endothelial progenitor cells among others[108-110]. Previous reports suggest a prominent role for the cell surface receptor CXCR4 in regulating monocyte retention and tissue distribution following tissue damage[30, 111, 112]. We have also observed that non-classical monocytes in particular may be functionally distinguished from classical monocytes by their increased CXCR4-mediated chemotaxis and that selective recruitment of non-classical monocytes along peri-implant arterioles promotes growth and maturation of microvessel networks in both skin and muscle injury models[6, 53].

In this study, we investigate how localized presentation of SDF-1α from engineered hydrogels impacts the recruitment and strategic distribution of circulating monocytes populations during sterile inflammatory wound healing and vascular remodeling. We have shown previously that particular derivatives of the glycosaminoglycan (GAG) heparin can protect growth factors such as BMP-2 from denaturing conditions, and that heparin-based biomaterials enable sustained presentation of biomolecular cargo and decrease the amount of growth factor necessary to achieve the same physiological response as bolus delivery[113-115]. Heparin enhances the loading of growth factor cargo into biomaterials and increased heparin content in the material can enhance the amount of growth factor released, likely by preventing denaturation of the growth factor within the carrier[115].

Thus, heparin derivatives are an excellent choice for sustained delivery of heparin-binding proteins such as SDF-1α[116]. To enable safe *in vivo* use of heparin-based biomaterials in present and future studies, we employed a desulfated heparin formulation that exhibits very low anticoagulant activity and extends the half-life of growth factors in solution and in delivery systems[114, 115, 117-122]. In this study, PEGDA hydrogels functionalized with N-desulfated heparin (Hep^{-N}) are loaded with SDF-1α in the presence of albumin as a stabilizing factor[123, 124].

We utilize the murine dorsal skinfold window chamber, a model of excisional skin injury, to test longitudinally the effects of FKN aptagels and SDF-1α-releasing heparin hydrogels on recruitment of non-classical monocytes and associated angiogenesis *in vivo*. Multiple modes of analysis, including intra-vital microscopy, flow cytometry, and whole-mount immunostaining of dorsal skin tissues are used.

3.3. Results

3.3.1. Fractalkine aptamers exhibit desirable binding kinetics with mouse fractalkine

The present study utilizes the FKN-aptamer sequence (FKN-S2) discovered by Waybrant *et al[125]* that was selected against human FKN (hFKN) through Selective Enrichment of Ligands via EXponential enrichment (SELEX). Mouse FKN (mFKN) possesses 78% homology to hFKN. Binding activity and kinetics of FKN- and SCR-aptamers to hFKN and mFKN were measured via surface plasmon resonance (SPR). In initial screening studies, FKN-aptamers bound to the mFKN surface with a ten-fold weaker

binding response compared to the hFKN surface, as expected (**Figure 1a,b**). No interaction was observed with the SCR-aptamers or the MSA surface for either aptamer (**Figure 1a-c**). Kinetic measurement revealed that the FKN-aptamers bound mFKN with an affinity (K_d = 1220 nM) that is approximately four-fold weaker than that observed for the hFKN (K_d = 340 nM) (**Figure 2c**). Interestingly, the observed difference in affinity is almost entirely accounted for in the dissociation kinetics as the mFKN interaction demonstrates marginally faster association kinetics but four-fold faster dissociation kinetics (k_{on} = 1.34 x 10^5 $M^{-1}s^{-1}$, k_{off} = 0.163 s^{-1}) when compared to the hFKN complex (k_{on} = 1.25 x 10^5 $M^{-1}s^{-1}$, k_{off} = 0.043 s^{-1}) (**Figure 2c**). These results indicate that the FKN-aptamer sequence is an appropriate candidate for attempting endogenous enrichment of mFKN.

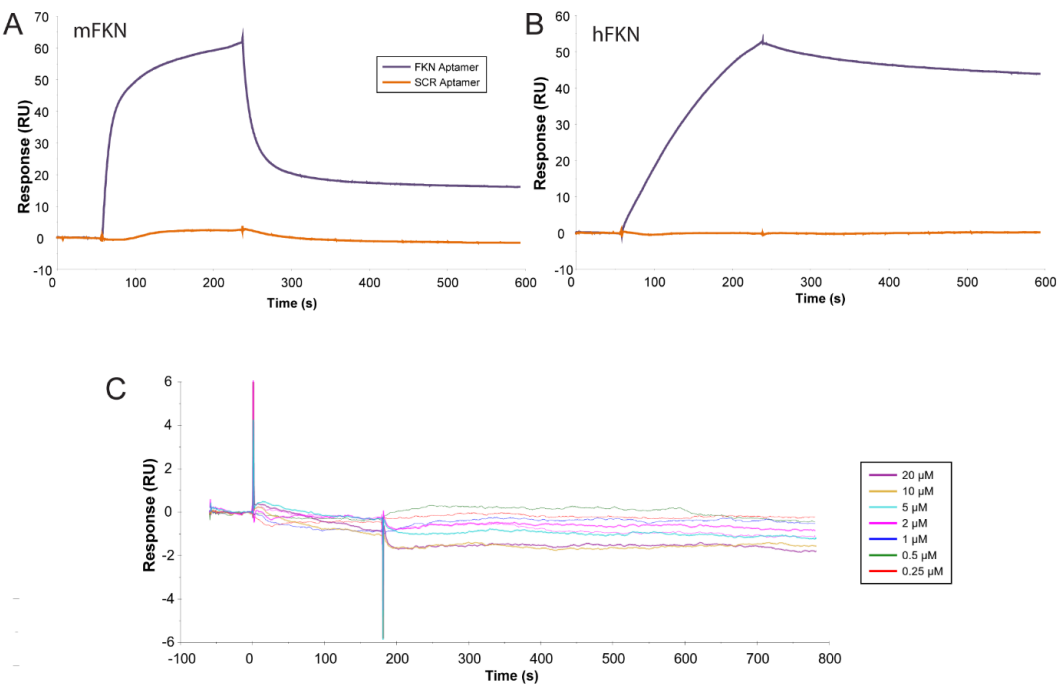

Figure 1. Preliminary binding analysis via surface plasmon resonance. Sensor chip was immobilized with a high amount of (A) mouse FKN (mFKN) or (B) human FKN (hFKN) followed by binding and release of either FKN-aptamers (blue) or SCR-aptamers (orange). (C) Sensor chip immobilized with mouse serum albumin demonstrated negligible binding towards FKN-aptamers.

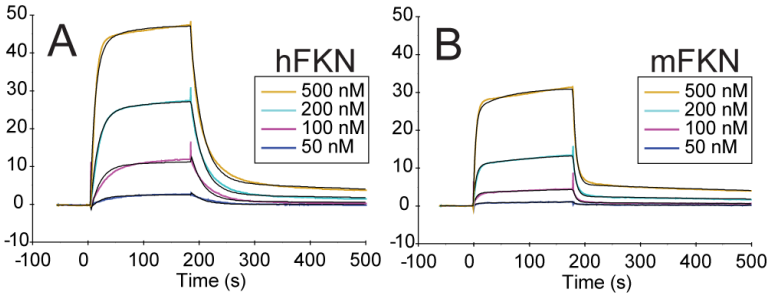

C

	hFKN		mFKN
	$1.247*10^5$ $M^{-1}s^{-1}$	k_{on}	$1.439*10^5$ $M^{-1}s^{-1}$
	0.0427 s^{-1}	k_{off}	0.1757 s^{-1}
	342.3 nM	K_d	1.221 µM

Figure 2. Surface plasmon resonance to study the kinetics of aptamer-FKN interactions. Response curve of a range of concentrations of FKN-aptamer flowed across immobilized (A) hFKN and (B) mFKN. (C) Binding kinetics demonstrated equivalent k_{on} rates but mFKN displayed faster k_{off} rates.

3.3.2. Acrydite-modified aptamers can be integrated with PEGDA to form aptagels

To conjugate the FKN- or SCR-aptamers with a PEGDA hydrogel backbone, a phosphoramidite group, Acrydite, was added to the 5' end of the aptamers and was expected to minimally affect kinetics[126]. As aptagel formulation precluded SPR assessment of potential perturbation of binding kinetics, functional testing was performed after aptagel synthesis. The Acrydite-modified aptamers were conjugated to PEGDA via free-radical polymerization initiated by APS and catalyzed by TEMED (**Figure 3a**). Soft and translucent hydrogels (aptagels) formed at a concentration of 5% PEGDA in a 0.5-mm thick glass mold and were punched out with a 2-mm biopsy (**Figure 3b**). Successful

covalent integration of Acrydite-modified aptamers with PEGDA was confirmed by incubating the aptagels with fluorescently-tagged complementary sequence (fCS) and comparing fluorescence to aptagels fabricated using unmodified aptamers or no aptamers (**Figure 3c**). A stark difference in fluorescence was appreciated in the Acrydite-modified aptagel group compared to either controls. Alternative chemistries were tested for potential application of endogenous enrichment to various scenarios *in vivo*. Amino-modified aptamers also successfully conjugated to N-hydroxysuccinimide (NHS) activated agarose beads, as determined by fCS. Fluorescence intensity correlated with the amount of aptamer conjugated (**Figure 3d**).

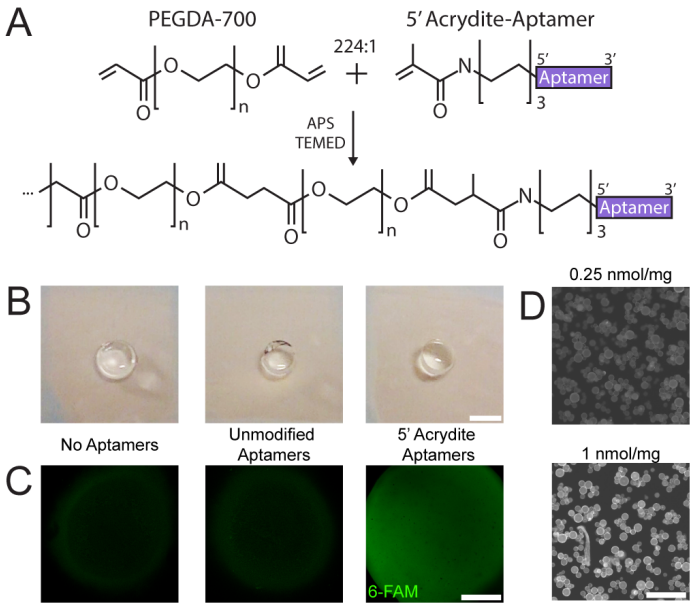

Figure 3. Chemistry and synthesis of aptagels. (A) Schematic of aptamer conjugation chemistry. (B) Bulk aptamer-functionalized PEGDA hydrogels (aptagels). (C) Staining with 6-carboxyfluorescein-labelled complementary sequence. (D) Alternate chemistry (NH_2 modified aptamers with NHS-activated agarose beads) for generating "aptabeads". The amount of aptamer conjugated correlated with the level of fluorescence staining.

3.3.3. Aptagels enrich and passively release fractalkine for at least 1 week in vitro

Aptagel functionality was assessed *in vitro* by measuring sequestration (indirectly, Day 0) and release (directly, Day 1 and onwards) of FKN after 24 h of incubation with either FKN- or SCR-aptagels (**Figure 4a**). Preliminary studies with rat FKN (rFKN) demonstrated that FKN-aptagels attract at least 40% of rFKN from high concentration incubations (1 μg/mL) (**Figure 5a**). Studies with aptabeads demonstrated immediate release of rFKN with the addition of complementary sequence (CS; 1 nmol) and equivalent passive release over 24 hours with the non-homologous CS, corroborating the fast k_{off} rates observed with SPR (**Figure 5b**). At least two washes were necessary to exclude non-specifically bound FKN from passive release data (**Figure 5c**). Because endogenous FKN concentrations range from hundreds of picograms to nanograms per milliliter[127], formal studies with mFKN were then performed using a lower concentration (50 ng/mL).

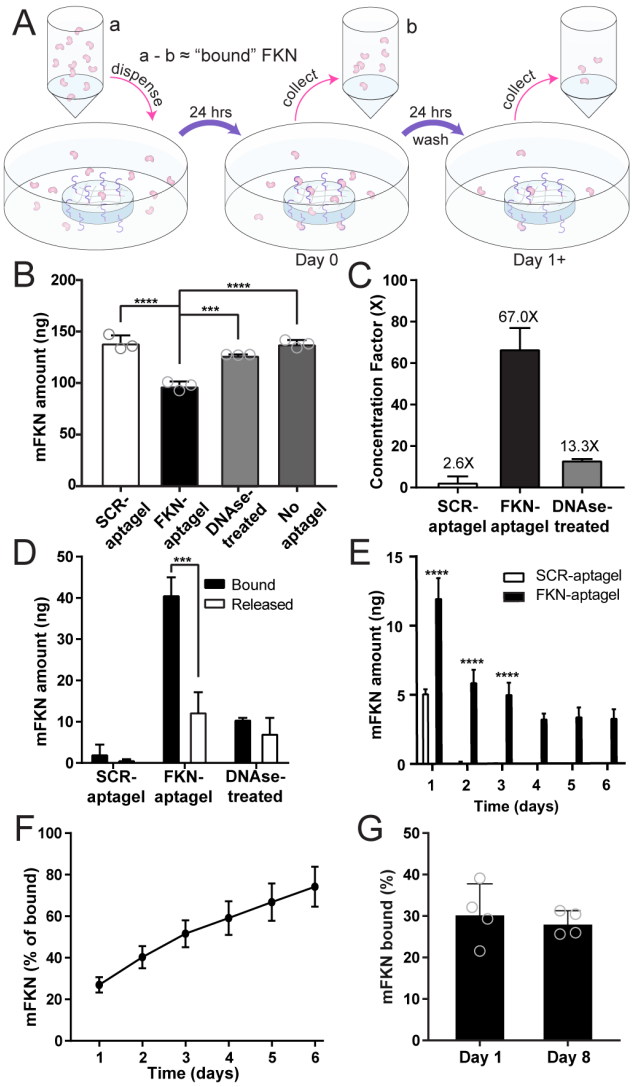

Figure 4. Aptagel functionality *in vitro*. (A) Schematic of methodology. (B) Amount of mFKN remaining in bath surrounding aptagels (n = 3; $P < 0.01$). (C) Concentration of mFKN in aptagels compared to bath. (D) Calculated 'bound' mFKN and Day 1 release (n = 3; ***$P < 0.001$) (E) Amount of mFKN released daily from aptagels. (n = 4; ****$P <$ 0.0001 compared to Day 6 FKN-aptagel release) (F) Cumulative mFKN release from FKN-aptagel (n = 4; P at least < 0.001 for each comparison) (F) Functionality was assessed after 7 days of testing. All graphs depict mean and standard deviation. One-way and repeated measures ANOVAs were used.

Day 0 samples demonstrated reduced mFKN levels in the bath surrounding FKN-aptagels, indicating sequestration of mFKN onto the aptagels (**Figure 4b**). No change was observed around SCR-aptagels (**Figure 4b**). Pre-treatment of the aptagels with 25 units of DNAse dampened FKN binding, indicating aptamer-protein interactions (**Figure 4b-d**). The FKN- and SCR-aptagels sequestered ~30% (40.8 ng ± 4.2 ng) and <0.1% (2.2 ± 2.2 ng) respectively from the initial amount of mFKN in the baths (138.1 ± 3.7 ng) (**Figure 4b,d**). Relative to the unbound FKN, the FKN-aptagels were 67X concentrated while the SCR-aptagels 2.6X concentrated (**Figure 4c**). After washes and transferring the aptagels to fresh baths, FKN-aptagels passively released 30% (12.4 ± 4.8 ng) of the sequestered amount over 24 h (**Figure 4d**). These methods were iterated daily, and 72.5% of mFKN was passively released over seven days (**Figure 4e,f**). After this period, FKN-aptagels were still able to sequester 28% of FKN from a fresh incubation, indicating near-full functionality (**Figure 4g**). Increasing BSA concentration five-fold reduced mFKN binding to FKN-aptagels (**Figure 5d,e**), still greater than SCR-aptagels, and demonstrated sustained release for at least 2 days (**Figure 5f**). These results demonstrate that FKN-aptagels can catch mFKN from the environment and passively release it while SCR-aptagels have no specific effect on mFKN.

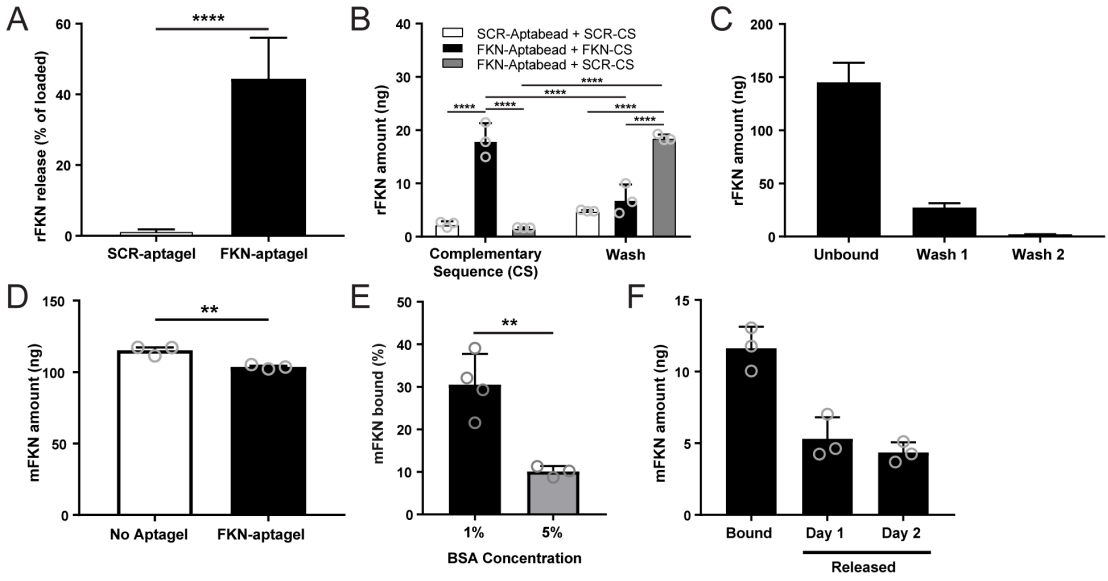

Figure 5. Supplementary analysis of aptagel functionality *in vitro*. (A) FKN-aptagels demonstrated significant binding and release of rFKN (n = 3, ****P < 0.0001). (B) Incubation of homologous CS with FKN-aptabeads resulted in release of rFKN while non-homologous CS failed to evoke the response. A wash with wash media (1% BSA and PBS) resulted in the release of rFKN that previously failed to release, indicating fast off-kinetics (n = 3). (C) After obtaining the "unbound" sample, three washes were sufficient to remove non-specifically bound FKN (n = 3). (D) FKN-aptagels captured mFKN from media with elevated (5%) BSA (n = 3, **P < 0.01). (E) FKN-aptagels incubated in 5% BSA bound less mFKN than those incubated in 1% BSA (n = 3, **P < 0.01). (F) FKN-aptagels incubated in 5% BSA released mFKN for at least 2 days (n = 3).

3.3.4. Aptagels enrich endogenous fractalkine and M2-like macrophages in vivo

To assess the ability of aptagels to enrich anti-inflammatory subpopulations of monocytes and macrophages, aptagels were implanted in the mouse dorsal skin window, a model of excisional skin injury. One week after injury and gel implantation, enrichment of endogenous FKN within the hydrogel was quantified by ELISA, and immune cell infiltration was analyzed via flow cytometry, t-Distributed Stochastic Neighbor Embedding (t-SNE) high-dimensional analysis, and intra-vital imaging (**Figure 6a**). FKN-

aptagels contained 3.7-fold more endogenous FKN than SCR-aptagels (**Figure 6g)**, indicating that FKN-aptagels successfully enrich FKN *in vivo*. To assess spatial localization of effects on immune cell infiltration, biopsies were collected from tissue underneath the gel ("near" region) and from tissue at the opposite side of the window ("far" region) (**Figure 6a**). FKN-aptagels increased the number of $CD206^+$ macrophages in the near tissue 3.8-fold compared to far tissue and 13.2-fold compared to tissue near the SCR-aptagels (**Figure 6c)**. Neither FKN-aptagels nor SCR-aptagels affected total macrophage count with statistical significance (**Figure 7a**). FKN-aptagels increased and SCR-aptagels decreased the proportion of macrophages expressing the $CD206^+$ alternatively-activated, M2-like phenotype in near tissue compared to far tissue (**Figure 6d**). FKN-aptagels increased the number of non-classical monocytes in near tissue 3.0-fold compared to far tissue and 6.4-fold compared to tissue near the SCR-aptagels (**Figure 6e**). Neither SCR- nor FKN-aptagels significantly affected the total number of monocytes or the frequency of non-classical monocytes out of total monocytes compared to the far region (**Figure 7b-d**). No significant differences were observed in neutrophil populations at day 7 either (**Figure 7e**). These results indicate that FKN-aptagels dramatically enhance accumulation of non-classical monocytes and M2-like macrophages in injured tissue near the implant.

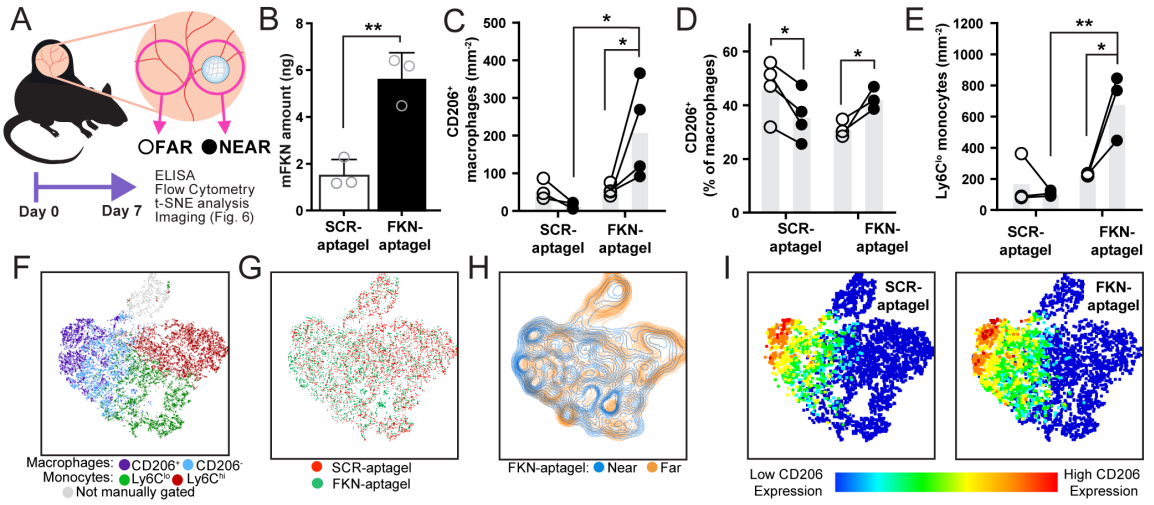

Figure 6. Aptagel immune modulation *in vivo*. (A) Experimental design. (B) Amount of mFKN released from explanted aptagels over 24 hours (n = 3, $^{**}P < 0.01$, t-test). Flow cytometry analysis of (C) $CD206^+$ M2-like macrophage count, (D) polarization of macrophages towards expression of CD206, and (E) $Ly6C^{lo}$ non-classical monocyte count (n = 4, $^{*}P < 0.05$, $^{**}P < 0.01$, two-way ANOVA). (F) tSNE analysis applied to (F) $CD45^+CD11b^+$ cells collected from both tissue regions in both aptagel groups, (G) $CD45^+CD11b^+$ cells from near tissue regions, and (H) $CD45^+CD11b^+$ cells from tissue in FKN-aptagel group. (I) t-SNE map color coded per CD206 expression in near tissue region of SCR-aptagel (left) or FKN-aptagel (right) groups.

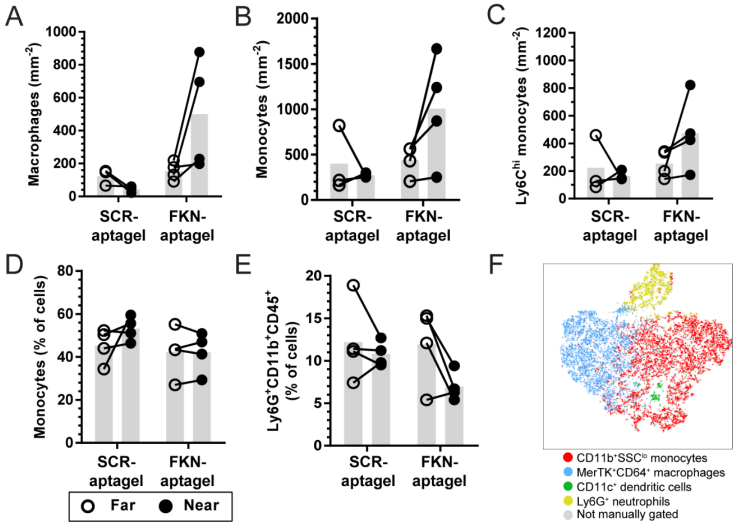

Figure 7. Supplementary analysis of aptagel immune modulation *in vivo*. Flow cytometry analysis of (A) total macrophage count, (B) total monocyte count, (C) $Ly6C^{hi}$

classical monocyte count, (D) frequency of monocytes out of total cells, and (D) frequency of neutrophils out of total cells (n = 4). (F) tSNE analysis applied to $CD45^{+}CD11b^{+}$ cells collected from dorsal tissue surrounding SCR or FKN aptagels (both far and near regions).

3.3.5. $CX3CR1^{+}$ cells demonstrate decreased motility by day 7 around FKN-aptagels

To assess whether chemotaxis of monocytes and macrophages towards aptagels persisted to day 7, time-lapse videos of $CX3CR1^{+}$ cell migration were acquired by confocal intra-vital microscopy in $CX3CR1^{gfp/+}$ transgenic mice (Error! Reference source not found.**a,b**), in which monocytes and macrophages are visualized by GFP expression[6, 34, 128]. Cell migrations paths (Error! Reference source not found.**c,d**) and displacement vectors (Error! Reference source not found.**e,f**) were rendered and $CX3CR1^{+}$ cell migration in the tissue surrounding FKN-aptagels exhibited decreased speed, increased path length, and decreased displacement length compared to SCR-aptagels (**Figure 8g-i**). These data demonstrate that by day 7, directional motility of $CX3CR1^{+}$ cells in the tissue around FKN-aptagels is reduced compared to SCR-aptagels.

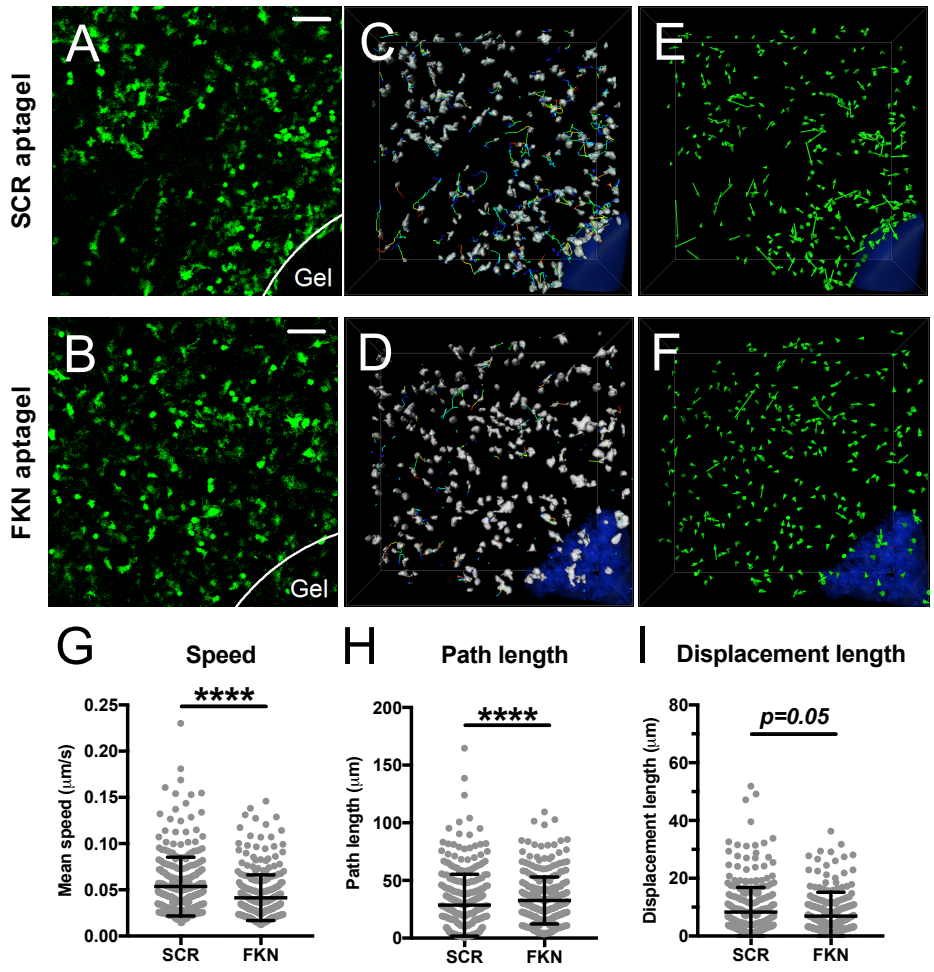

Figure 8. Time-lapse imaging of CX3CR1^{+} cell migration near aptagel edges via confocal intra-vital microscopy in CX3CR1$^{gfp/+}$ mice. (A-B) 3D projection of CX3CR1^{+} cell distribution. (C-D) 4D rendering of cell migration paths. (E-F) Displacement vectors of CX3CR1^{+} cell migration. Metrics of cell migration dynamics include (A) displacement length, (B) path straightness, (C) mean speed, and (D) path length. All graphs depict mean and standard deviation. (n = 300 cells across 3 animals per group, *$P < 0.05$, ****$P <$ 0.0001, t-test).

3.3.6. aHep^{-N}-SDF hydrogels sustain release of bioactive SDF-1α in vitro

A selectively desulfated heparin PEG-DA hydrogel (Hep^{-N}) was engineered to utilize the natural capacity of heparin to protect, sequester, and release growth factors as a

novel strategy to produce a localized *in vivo* gradient of SDF-1α[113-115, 117, 121]. Fabrication and composition of heparin-containing hydrogels is illustrated in **Figure 9a**. SDF-1α release from Hep^{-N} gels incorporating albumin was superior to release from either unmodified PEG-DA, Hep^{-N}-PEG-DA, or albumin-PEG-DA gels (**Figure 10**); therefore, in subsequent experiments, albumin was included in the Hep^{-N}-PEG-DA hydrogels ($aHep^{-N}$) to improve release of SDF-1α. The albumin may help stabilize the protein from denaturation within the gel and since albumin is also negatively charged at neutral pH, may reduce growth factor binding to the gel and thus promote release[123, 124]. The albumin-containing, N-desulfated heparin-based hydrogels ($aHep^{-N}$) chosen for this study released 9.8 ± 0.1% of the loaded SDF-1α by 5h, 19.2 ± 0.1% by 24h, 23.1 ± 0.1% by day 3, and 23.8 ± 0.0% by day 7 *in vitro* (**Figure 9b**). Chemotaxis of primary murine bone marrow cells toward hydrogel conditioned media was analyzed to test the bioactivity of SDF-1α released from the hydrogels. Media conditioned for 24h with $aHep^{-N}$-SDF gels induced a statistically significant increase in directional chemotaxis (27.22 ± 9.5%) compared to

release media from the same gels with no SDF-1α (aHep^{-N}), indicating that SDF-1α bioactivity is retained after release from aHep^{-N} hydrogels (**Figure 9c**).

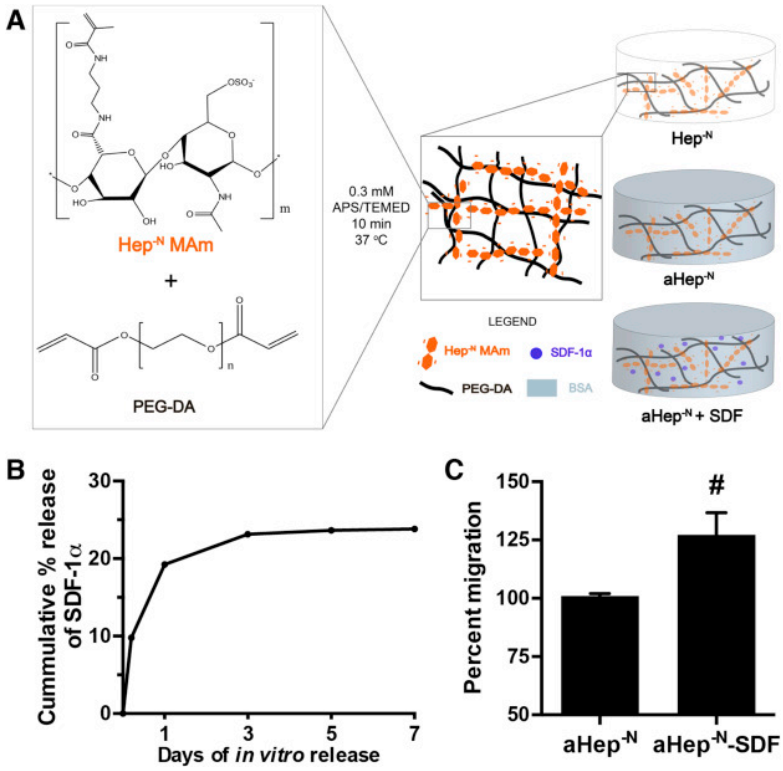

Figure 9. aHep^{-N} hydrogel provides sustained release of bioactive SDF-1α. (A) Hydrogels were fabricated by thermal cross-linking of N-desulfated heparin methacrylamide and PEG-DA. Hydrogel formulations used in this study were: unloaded (Hep^{-N}) internal controls, albumin loaded (aHep^{-N}), or SDF-1α and albumin loaded (aHep^{-N}-SDF). (B) SDF-1α release from aHep^{-N}-SDF hydrogels is sustained over 3 days *in vitro* (n=3, mean ± SD) and (C) stimulates chemotaxis of mouse bone marrow cells *in vitro* (#p<0.05, unpaired t-test, n=4, mean ± SEM).

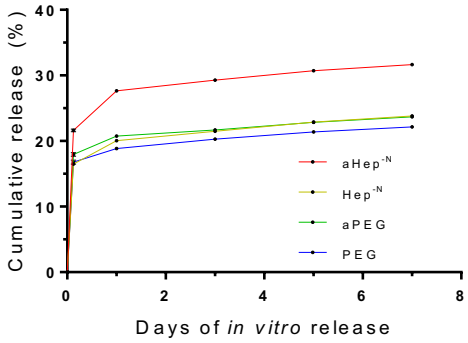

Figure 10. Effect of albumin on SDF-1α release. Cumulative release of SDF-1α from hydrogels composed of PEG-DA only (PEG, blue line), PEG-DA with albumin (aPEG, green line), PEG-DA with N-desulfated heparin methacrylamide (Hep^{-N}, yellow line), and PEG-DA with both N-desulfated heparin methacrylamide and albumin (aHep^{-N}, red line). (n=4, mean ± SD).

3.3.7. aHep^{-N}-SDF hydrogels locally recruit marrow derived cells in vivo

The murine dorsal skinfold window chamber ("backpack") model enables longitudinal spatiotemporal intravital imaging of host responses to biomaterial implants including remodeling of vessel networks and coupled innate immune response[6, 53]. To evaluate the *in vivo* recruitment of circulating cells to the gels, we generated mouse chimeras whose bone marrow-derived hematopoietic lineage cells express a constitutive enhanced green fluorescent protein (EGFP) transgene. Chimeric mice fitted with dorsal skinfold windows permit the tracking of cells originating from the bone marrow and arriving at the injury niche. The experimental design was internally controlled to evaluate a localized biological response around the gel by implanting one aHep^{-N}-SDF ("experimental") gel and one Hep^{-N} ("internal control") hydrogel into opposite sides of the same window (less than 8mm separation between center of each gel) (**Figure 11a**). Whole

mount immunofluorescence microscopy analysis of dorsal skinfold tissue 2 days after surgical tissue disruption and hydrogel implantation showed that the aHep^{-N}-SDF hydrogel appeared to recruit more bone marrow-derived (EGFP^{+}) circulating cells than internal control hydrogels in the same dorsal skinfold window chamber (**Figure 11b**). Moreover, the spatial distribution of recruited bone marrow-derived cells was localized to the SDF-1α implant niche, as indicated by higher trend in EGFP fluorescence underneath the SDF-1α-releasing gels compared to paired internal controls in all 3 animals (p=0.1; **Figure 11c**).

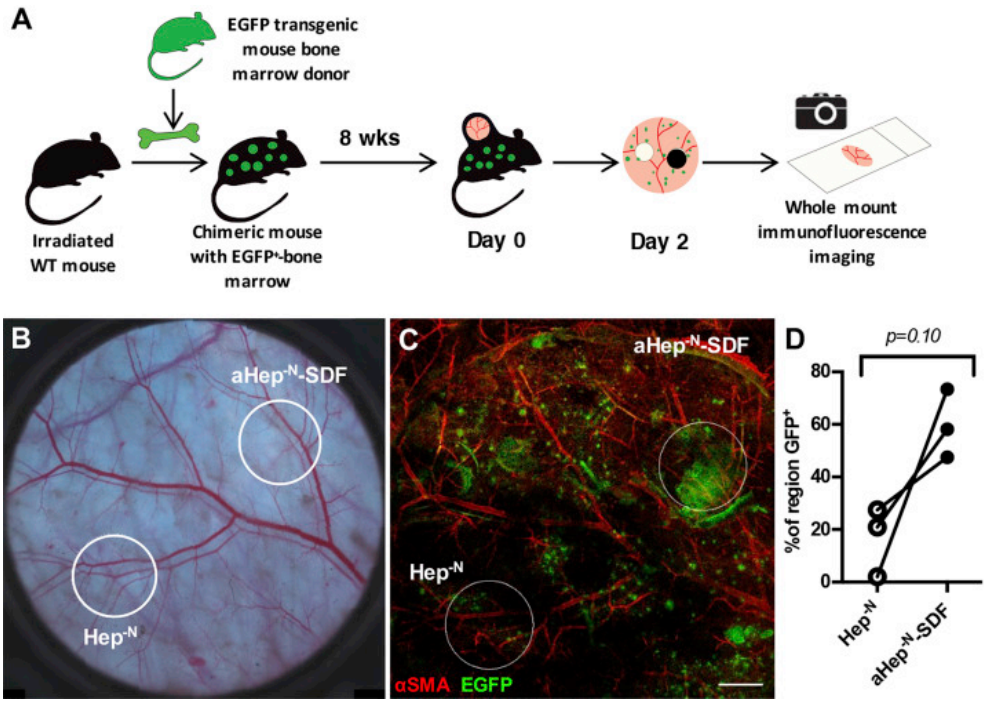

Figure 11. SDF-1α recruits bone marrow-derived cells to the hydrogel implant niche. (A) Chimeric mice were generated as illustrated by irradiation and bone marrow transplantation from an EGFP transgenic mouse. (B) Brightfield tiled image of dorsal skinfold window chamber on day 0 with location of aHep^{-N}-SDF and internal control gels. (C) Rendering of Z-stacked tile scans acquired via confocal laser scanning microscopy show that more EGFP^{+} bone marrow-derived cells (green) are recruited to the tissue beneath aHep^{-N}-SDF hydrogels compared to Hep^{-N} internal control and recruitment is highly localized. Vessels are counterstained with αSMA (red). (D) Percent area under the gel positive for GFP. Lines connect paired analysis of internal control and experimental gels in each animal (p=0.1 by paired t-test, n=3; scale bar = 1mm).

3.3.8. aHep^{-N}-SDF hydrogels enhance local recruitment of non-classical monocytes

To further evaluate the identity and localization of recruited cells, wildtype C57/BL6 mice were implanted with one experimental (aHep^{-N} or aHep^{-N}-SDF) gel and one internal control unloaded gel (Hep^{-N}) as described above (**Figure 12a**). To examine the phenotypes of recruited cells in the tissue surrounding each implant, dorsal tissue was harvested and bisected along the midline separating the two hydrogels (**Figure 12a**). The proportion of CD11b^{+} cells out of total cells in the digested dorsal tissue was not different between groups (**Figure 12b**); however, hydrogels releasing SDF-1α significantly increased the tissue recruitment of non-classical monocytes (CD11b^{+}SSC^{lo}Ly-6C^{lo}) compared to aHep^{-N} animals (**Figure 12c**). Local infiltration of classical monocytes (CD11b^{+}SSC^{low}Ly-6C^{high}) was not significantly different between unloaded and SDF-1α-loaded aHep^{-N} gels (**Figure 12d**). The ratio of non-classical to classical monocytes was significantly higher in the tissue surrounding the SDF-1α releasing hydrogels compared to both the Hep^{-N} internal control and the aHep^{-N} experimental control hydrogels (**Figure 12e**). To gain mechanistic insight into the preferential recruitment of non-classical monocytes by SDF-1α, we analyzed the cell surface expression of the SDF-1α cognate receptor, CXCR4. Bone marrow-derived non-classical monocytes have higher surface expression of CXCR4 compared to classical monocytes (**Figure 12f**) These data suggest that the SDF-1α releasing hydrogel preferentially attracts the pro-regenerative non-classical subset of monocytes to the tissue surrounding the gel, which is in accordance with our previous work showing that

non-classical monocytes migrate toward SDF-1α significantly more than classical monocytes[6].

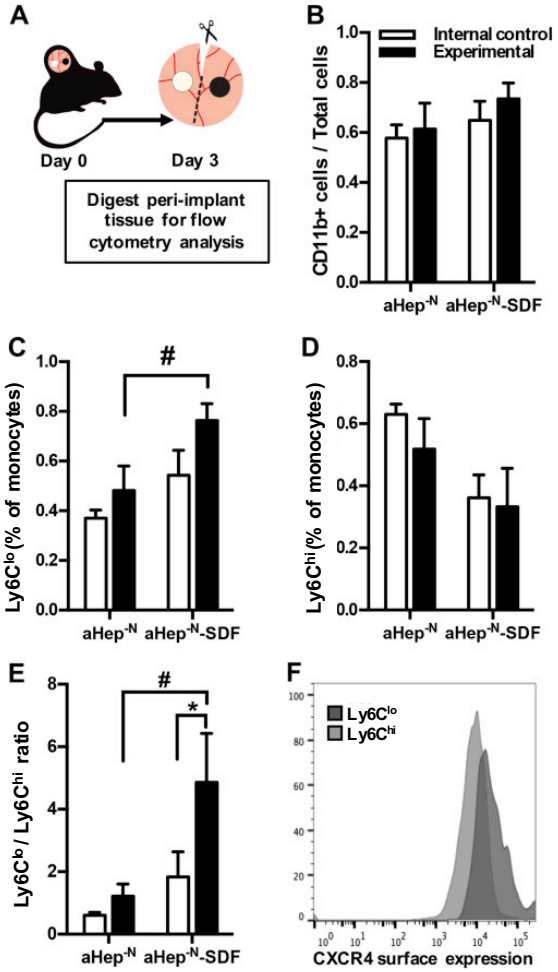

Figure 12. Localized recruitment of anti-inflammatory monocytes to the tissue surrounding the aHep^{-N}-SDF hydrogel. (A) Tissue was bisected between the internal control (Hep^{-N}, white) and the experimental (aHep^{-N} or aHep^{-N}–SDF, black) gels, digested with collagenase, and analyzed by flow cytometry. (B) The proportion of CD11b^{+} cells in the implant niche is not significantly different between groups. (C) aHep^{-N}-SDF hydrogels induce a significant increase in the recruitment of non-classical monocytes, but not classical monocytes (D) to the peri-hydrogel tissue. (E) The ratio of non-classical to classical monocytes in the tissue surrounding aHep^{-N}SDF hydrogels is higher than aHep^{-N} experimental control and Hep^{-N} internal control. (F) Surface expression of the SDF-1α cognate receptor CXCR4 is higher on the surface of non-classical compared to classical monocytes. (#, *p<0.05: two-way ANOVA with repeated measures and Bonferonni test for multiple comparisons; n=5 mice from 2 independent experiments, mean ± SEM).

3.3.9. Early arteriolar vascular expansion correlates with non-classical monocyte recruitment

Previous reports suggest that perivascular positioning of monocytes and macrophages promotes vascular remodeling[6, 48, 55]; therefore, we utilized intravital confocal laser microscopy analysis of post-capillary venules to examine the infiltration and positioning of CX3CR1-EGFP^{+} monocytes (**Figure 13a,b**, green) with respect to vessels (**Figure 13a,b**, red) in the peri-implant region. Images were further processed with Imaris software to generate 3D surface renderings and visualize cell proximity to vessels; a 3D distance heat map was overlayed on the cells (**Figure 13c,d**). Significantly more CX3CR1^{+} cells were observed in regions of interest around the aHep^{-N}-SDF hydrogels on day 1 after dorsal window chamber placement (**Figure 13e**; 68 ± 17 cells (Hep^{-N}) vs. 127 ± 88 (aHep^{-N}-SDF) in 0.49mm^2 area; n=3 mice). Early recruitment of CX3CR1^{high} non-classical monocytes was also observed (10 ± 4 cells (Hep^{-N}) vs. 22 ± 10 (aHep^{-N}-SDF); n=3 mice) in agreement with our finding that SDF-1α delivery increases recruitment of non-classical monocytes.

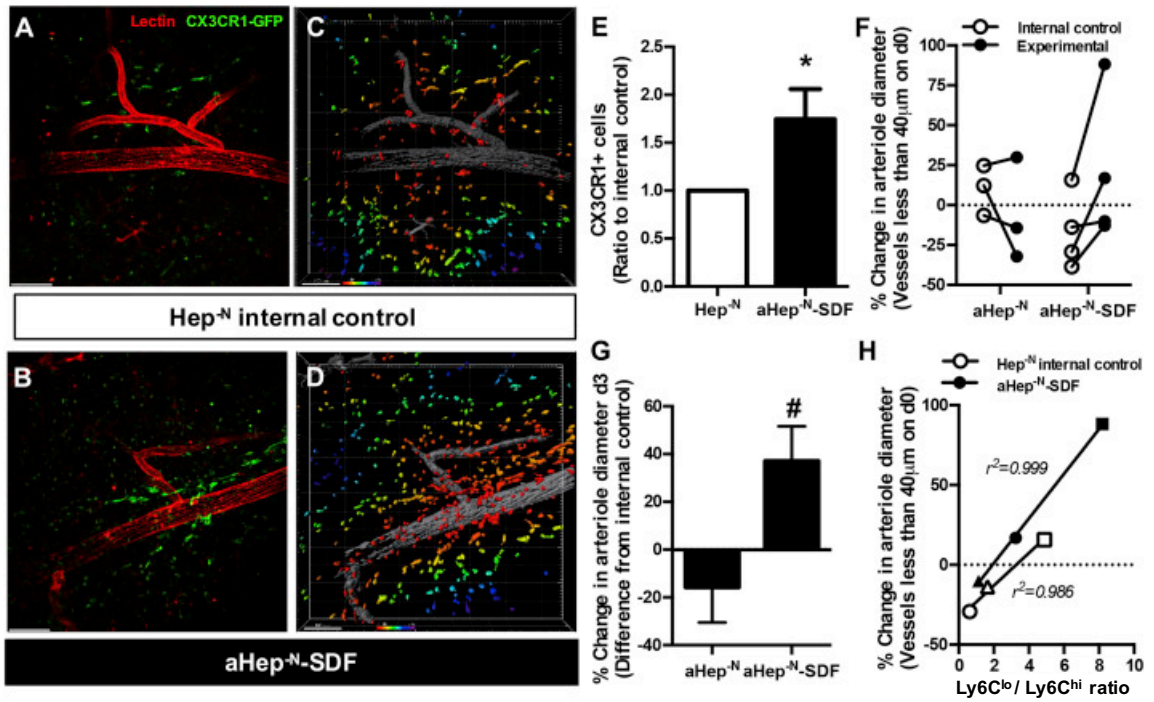

Figure 13. Monocyte recruitment correlates with early arteriolar remodeling. (A, B) Representative intravital imaging adjacent to each gel 1 day after surgery in CX3CR1-eGFP mice. (C, D) Color-coded map of 3D distance of CX3CR1+ cells from the surface of vessels rendered in Imaris software shows increased distribution of monocytes near vessels (perfused lectin, grey) near the aHep^{-N}-SDF gel (scale bar = 100μm, color scale: 0.00 to 0.275mm distance to vessel). (E) SDF-1α release increases perivascular CX3CR1+ cells (*p<0.05, paired ratio t-test, n=3, mean ± SEM). (F) The percent change in arteriolar diameter from day 0 is not significantly changed on day 3 (Lines connect paired analysis of internal control and experimental gels in each animal); however, (G) the change from internal control significantly increased (#p<0.05, one-tailed t-test, n=3-4, mean ± SEM). (H) The change in vessel diameter is highly correlated to the balance of non-classiacal and classical monocytes recruited to the tissue (linear regression of paired data, n=3, m=14.0 ± 0.4, r^2=0.986 for aHep^{-N}-SDF; m= 10.2 ± 1.2, r^2=0.999 for Hep^{-N}).

Longitudinal intravital brightfield microscopy analysis of hydrogel-treated dorsal tissue at days 0 and 3 does not show significant changes between groups in the diameter of peri-implant arterioles with an initial diameter less than 40μm (**Figure 13f**); however the change in arteriolar diameter in aHep^{-N}-SDF animals relative to the internal control was

significantly higher than aHep^{-N} relative to its internal control (**Figure 13g**, *n*=3-4 mice per group, #*p*<0.05, paired t-test). Linear regression analysis of paired immunophenotyping (by flow cytometry) and vessel measurements (by intravital imaging) indicates that arteriolar diameter enlargement positively correlates with non-classical:classical monocyte ratio in peri-implant tissue for both the SDF-1α- loaded and unloaded controls (**Figure 13h**). SDF-1α increased the slope of the regression line compared to unloaded gels suggesting that SDF-1α may amplify the positive effects of non-classical monocyte recruitment with respect to arteriolar diameter increase (**Figure 13h**).

3.3.10. aHep^{-N}-SDF hydrogels sustain local arteriolar expansion and microvascular network growth

SDF-1α release maintained peri-implant arteriolar structural enlargement at day 7 (**Figure 14a**). All animals exhibited a positive arteriolar enlargement response to SDF-1α release from aHep^{-N}-SDF gels compared to internal control while aHep^{-N} gels did not differ from internal controls (**Figure 14b**). Accordingly, the change in arteriolar diameter in aHep^{-N}-SDF relative to the internal control was significantly higher than aHep^{-N} relative to its internal control (**Figure 14c**; -2.45% ± 10.55% (aHep^{-N}) vs. 24.10% ± 6.43% (aHep^{-N}-SDF); n=3-5). We hypothesized that the sustained pro-arteriogenic response may be supported by the persistence of recruited non-classical monocytes through their differentiation into macrophages, particularly of the M2 phenotype associated with regeneration[6, 71]. CD206^{+} M2-like macrophages were identified in a peri-arteriolar niche location (**Figure 14d**), a phenomenon previously associated with

arteriogenesis[129]. SDF-1 delivery increased the frequency of $CD206^{+}$ macrophages within the macrophage pool compared to $aHep^{-N}$ (**Figure 14e**).

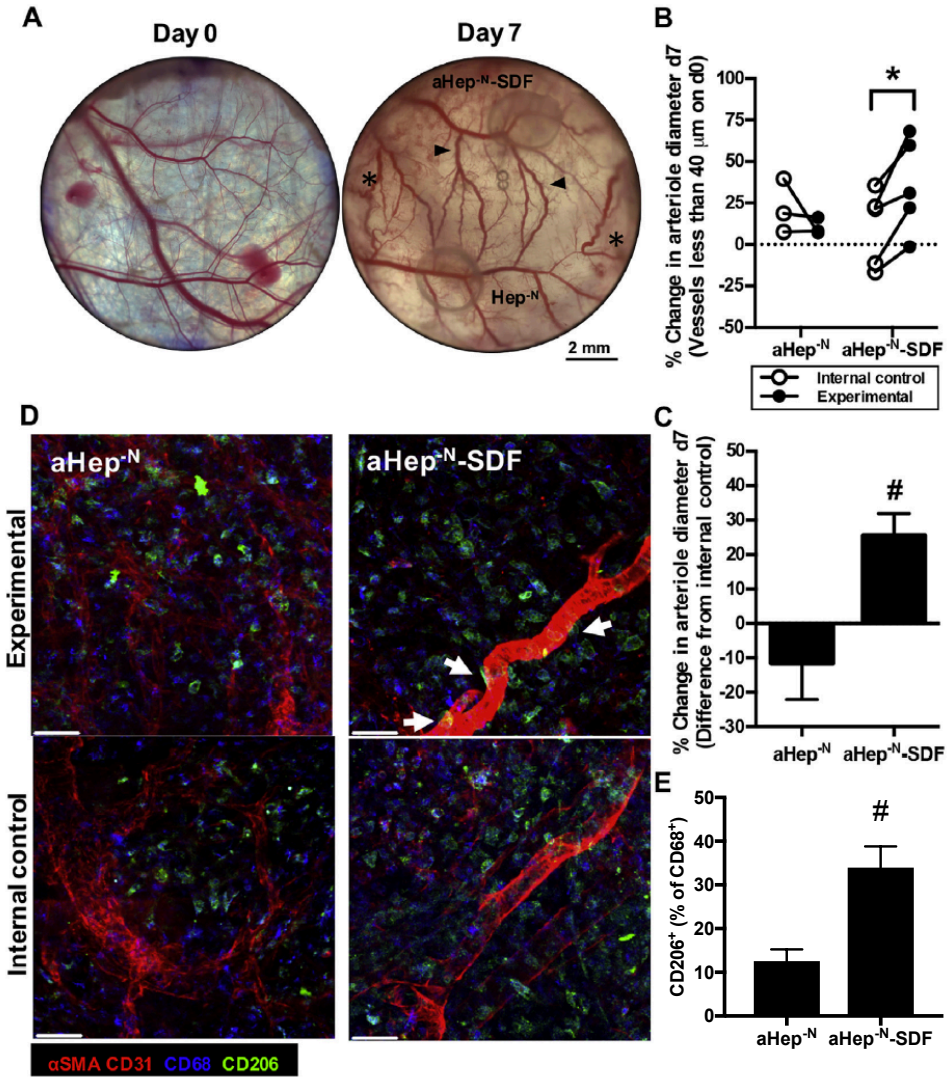

Figure 14. $aHep^{-N}$-SDF hydrogels sustain inflammatory arteriolar remodeling. (A) Dorsal skinfold tissue treated with $aHep^{-N}$-SDF hydrogels increases vessel caliber (arrowheads) and tortuosity (asterisks) by day 7 (Scale bar 2mm). (B) All animals display significantly increased arteriolar diameter near $aHep^{-N}$-SDF hydrogels compared to internal controls. (*p<0.05 by two-way ANOVA with repeated measures and Bonferonni test for multiple comparisons, n=3-5 from 2 independent experiments, lines connect paired analysis of internal control and experimental gels in each animal). (C) The relative increase in arteriolar diameter above internal control is significantly higher in the $aHep^{-N}$-SDF group compared to $aHep^{-N}$ control (#p<0.05, t-test, n=3-5 mice, mean ± SEM). (D) CD206+ M2-

like macrophages were identified in the tissue beneath aHep^{-N}-SDF hydrogels and associated internal controls (red, CD31 and αSMA; blue, CD68; green, CD206; scale bar = 50μm). M2-like macrophages were localized in a peri-arteriolar niche (arrowheads). Lower panels: internal control Hep^{-N} gels. (E) Frequency of CD206+ macrophages within the macrophage pool (*p<0.05, t-test, n=5-11 regions across 2-3 mice per group, mean ± SEM).

In addition to rapid changes in perfusion that can be accommodated by arteriogenic changes in local vasculature, angiogenic microvascular network growth is another hallmark of regenerative vascular remodeling. Analysis of network length in brightfield intravital microscopy was unable to detect differences in vessel length density between groups (**Figure 15a,b**) perhaps due to the resolution limit of this technique (approximately 20-25μm). However, whole mount CD31 immunostaining of perfusion-fixed, explanted dorsal skin enabled visualization of capillary-level microcirculation undetectable by brightfield imaging (**Figure 15c,d,e,f**). Tissue surrounding internal control hydrogels appeared to be more optically opaque in brightfield imaging, possibly indicating the formation of granulation tissue that may obscure visualization of microvessels. SDF-1α delivery from aHep^{-N}-SDF hydrogels significantly increased the density of CD31^{+} vessels near the implant compared to internal control less than 8mm away in the window chamber at day 7 (**Figure 15g**). These data support the idea of highly localized regenerative capacity of bioactive SDF-1α released from a heparin-based hydrogel *in vivo*.

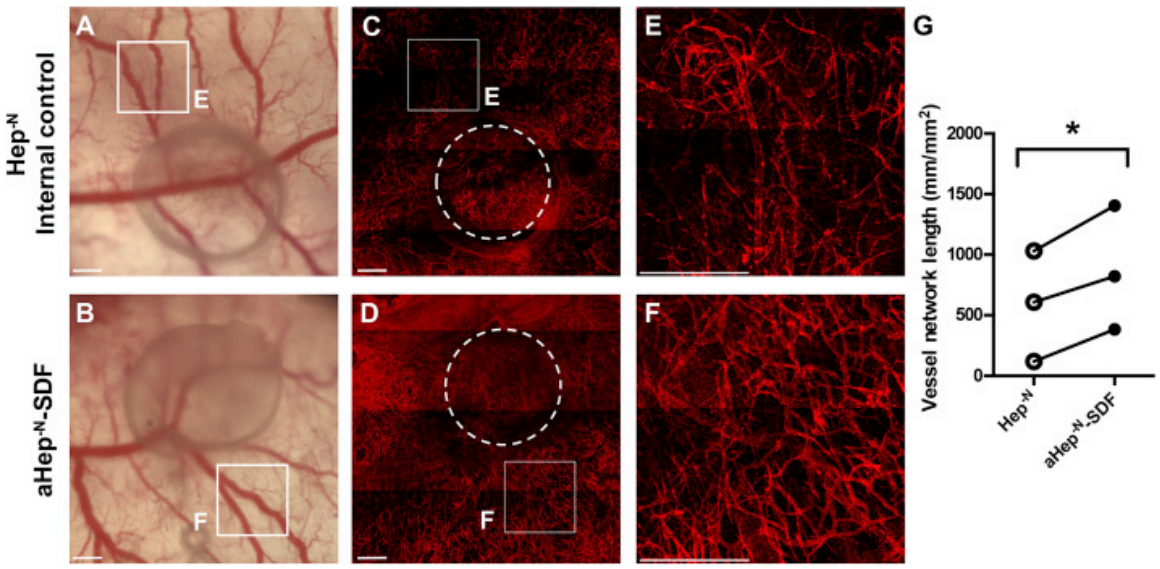

Figure 15. aHep^{-N}-SDF hydrogels enhance inflammatory microvascular network growth. (A, B) Intravital brightfield microscopy and (C, D) CD31^{+} whole mount immunofluorescence imaging of microvasculature surrounding gels. (E-F) Enlarged view of microvascular network in the region of a secondary-to-tertiary venular branch point near the hydrogel (scale bar = 500μm) (G) Analysis of 4mm-diameter circular ROI circumscribing each gel region (shown in Figure S4) indicates increased density of microvessels near aHep^{-N}-SDF hydrogels compared to internal control in all animals (*p<0.05 by paired t-test, n=3, lines connect paired analysis of internal control and experimental gels in each animal).

3.4. Discussion

3.4.1. Fractalkine aptagels

Aptagel-mediated enrichment of endogenous FKN avoids several major disadvantages of exogenous protein delivery, including their short half-lives *in vivo*, their suboptimal efficacy, the risk of immunogenic responses, batch variabilities and high costs in synthesis or purification[79, 80, 97-99]. Exogenous proteins exhibit short half-lives[100-103] and reduced potency[104] due to a lack of post-translational modifications (PTMs),

molecular instability and non-native glycosylation patterns. This is exacerbated by destabilizing insults during manufacturing, purification, storage, and delivery of exogenous proteins. PTMs significantly affect chemokine activity *in vitro* and *in vivo*. Engineering patterns of glycosylation that mimic endogenous proteins may ameliorate protein instability, but glycosylation biology is intrinsically complex and the glycoengineering process is technically challenging[104]. Circulation and clearance[102, 103] also reduce half-lives of small proteins, and achieving therapeutic pharmacodynamics may require multiple doses or sustained-release of otherwise fragile exogenous proteins. Immunogenic reactions are initiated by antibodies that react to small structural differences between exogenous and endogenous proteins[105, 106]. These anomalies in exogenous proteins arise primarily from variations in peptide sequence and glycosylation patterns, as well as detrimental effects of the manufacturing and storage process. The antibodies hamper efficacy, pharmacokinetics and pharmacodynamics, and risk the development of autoimmunity and systemic immune effects such as anaphylaxis and cytokine release syndrome[107]. Clinical translation of therapeutic proteins is further delayed because pre-clinical models poorly predict clinically relevant immunogenicity[107]. Lastly, synthesizing or purifying exogenous proteins is expensive, and managing batch-to-batch variability requires solutions in the manufacturing and quality control process that increase cost of production. As discussed earlier, enriching endogenous proteins can ameliorate these problems by 1) concentrating target proteins in the injury site; 2) exploiting the efficacy of PTMs and endogenous signaling pathways; 3) avoiding the introduction of anomalous structures or glycosylation patterns; 4) mitigating cost, manufacturing, and regulatory hurdles to clinical translation.

Accumulation of non-classical monocytes and M2-like macrophages within injured tissue is associated with augmented repair and enhanced implant integration[6-8, 27, 57, 70, 130-136]. A novel strategy to stimulate pro-regenerative inflammation is to enhance the recruitment of circulating non-classical monocytes, which are biased progenitors of M2-like macrophages[33]. Elevation of FKN and CX3CR1 is associated with better healing in dermal wound injuries[7, 131, 137]. Toward this end, the present study leverages non-classical monocytes' relatively high surface expression of CX3CR1, the cognate receptor of the chemokine FKN. To target the FKN-CX3CR1 axis, we synthesized implantable aptamer-functionalized hydrogels that catch and release FKN protein. Results *in vitro* show that mFKN binds to FKN-aptamers but rapidly dissociates, and that aptagels catch and passively release FKN for at least one week. Aptagel implantation in a murine excisional skin wound enriches endogenous FKN within the gel matrix and increases accumulation of non-classical monocytes and M2-like macrophages in the injured tissue surrounding the implant.

Aptagel-mediated recruitment of $CX3CR1^{+}$ cells requires that FKN be enriched locally but not sequestered permanently. Achieving this dynamic theoretically requires fast association (k_{on}) and fast dissociation (k_{off}) kinetics for aptamer-protein interactions. A fast k_{on} with slow k_{off} would likely sequester FKN, while the converse would fail to attract FKN. Waybrant *et al.,* discovered FKN-aptamers against hFKN through SELEX; a process that selects strong-binding aptamers (fast k_{on}, slow k_{off}, small K_D). As mFKN shares 78% homology with hFKN, we found FKN-aptamer k_{on} kinetics with mFKN were akin to hFKN while k_{off} kinetics were approximately four-fold faster. Thus, mFKN and hFKN associated equally well with FKN-aptamer, but mFKN dissociated faster; a desirable kinetic regime

for endogenous enrichment of mFKN. Additionally, both FKN variants had significantly lower affinity to FKN-aptamer (mFKN K_d = 1.2 μM, hFKN K_d = 340 nM) than FKN does with its cellular receptor CX3CR1 (30-740 pM)[125], allowing attracted FKN to signal to $CX3CR1^+$ cells. We report a weaker hFKN interaction with FKN-aptamer than Waybrant *et al.* (K_d = 3.7 nM) likely due to methodological differences.

Aptamers immobilized within the hydrogel matrix (i.e. aptagels) maintained catch-and-release activity for at least one week *in vitro*. This activity was also demonstrated in a bead-based formulation (i.e. aptabeads), indicating generalizability of endogenous enrichment across matrix-based biomaterial platforms. DNAse dampened functionality, suggesting that incorporation of DNAse resistant bases may further amplify FKN enrichment and consequent recruitment of $CX3CR1^+$ cells. Alternatively, maintaining DNAse susceptibility might be desirable to release any sequestered protein. Controlled inactivation of the material or bulk release of any sequestered protein could also be achieved via introduction of CS.

The present study conducts the first evaluation of an aptamer-based catch-and-release system *in vivo[93, 138]*. Increased numbers of non-classical monocytes and $CD206^+$ macrophages near FKN-aptagels may be explained by multiple mechanisms of action. FKN-aptagels bind endogenous fractalkine *in vivo* and exhibit rapid dissociation rate *in vitro*, suggesting that FKN-aptagels may generate local FKN gradients that affect $CX3CR1^+$ accumulation. Numerous studies indicate that the fractalkine-CX3CR1 axis promotes migration[139, 140] and survival[37, 141-143] of monocytes and macrophages. Non-classical monocytes, which express high levels of CX3CR1 compared to classical monocytes[34], may be more responsive to FKN-induced survival and migration, thereby

enriching this subpopulation. Given that non-classical monocytes are biased progenitors of M2-like macrophages[33], the observed increase in $CD206^+$ macrophages may be caused by differentiation of the increased non-classical monocyte population. Additionally, FKN-induced survival may limit monocytic cell death preventing feed forward pro-inflammatory responses. Recruitment of tissue-resident $CD206^+$ macrophages to peri-implant tissue is also a plausible mechanism[70, 139, 140]. The FKN-CX3CR1 signaling axis is also known to promote adhesion[78, 144, 145] of $CX3CR1^+$ cells. Interestingly, intra-vital microscopy showed decreased motility around FKN-aptagels by day 7 suggesting that recruited $CX3CR1^+$ cells may increase FKN-mediated adhesion by that timepoint. Future studies could investigate potential progression from chemotactic to adhesive signaling. No significant changes in neutrophil counts were observed, corroborating an earlier study[131].

Toward the goal of clinical translation, future studies could employ computational modelling or experimentation with mutated or modified aptamers[86, 126] to identify if better enrichment kinetics exist and to enable enrichment of hFKN. The ability to alter formulations may enable application to diverse clinical contexts. For example, aptabeads or aptamer-functionalized nanoparticles[146] may be advantageous when injury occurs deep within tissue and bulk hydrogel implantation is not feasible, such as after brain injury (e.g. trauma or stroke). Elevated FKN is associated with improved healing after brain injury[80-82] but while FKN levels initially rise, driving $CX3CR1^+$ cell recruitment, they soon rapidly fall[127]. FKN-aptabeads could prolong $CX3CR1^+$ cell recruitment by storing FKN during the early surplus and releasing it during later days as FKN levels decline. Other critical molecules can be targeted by identifying binding aptamers via SELEX and tuning

aptamer kinetics via selection pressures, mutations, truncations, and additions[86]. Through this, combinations of aptamers could be immobilized on biomaterials to treat complex pathological conditions in which regulation or enrichment of multiple proteins is required.

3.4.2. SDF-1α-releasing aHep^{-N} hydrogels

Stimulating the expansion of stable vascular networks promises to improve therapeutic outcomes after ischemia, trauma, and tissue transplantation; however, engineering a therapy that potently and safely promotes vascularization remains an unmet clinical need. Spatial concentration of pro-angiogenic/arteriogenic therapies would minimize off-target risks such as stimulating rogue tumor vasculature[147, 148], while focusing treatment only to the injured or regenerating tissue region. Here we exploited the ability of PEG-DA hydrogels functionalized with N-desulfated heparin, a modified GAG, to localize the presentation of bioactive growth factor cargo SDF-1α[114] and spatially concentrate its pro-angiogenic/arteriogenic effects. Selectively desulfated heparin exhibits low anticoagulant activity compared to native heparin while still protecting bioactivity of growth factor cargo[114, 115, 117, 121].

SDF-1α is of interest in angiogenic/arteriogenic therapies because pathophysiologically, SDF-1α can be secreted perivascularly by vessel-associated cells downstream of VEGF signaling, contributing to positioning of monocytes within a localized gradient of SDF-1α at the outer vessel wall[55]. While recruitment of monocytes has been associated with pro-angiogenic and arteriogenic metrics[6, 30, 45, 48, 51, 55,

149], the phenotype of SDF-1α-recruited cells has not been well characterized. Literature strongly associates both arteriogenesis and angiogenesis with recruitment of Ly-6C^{lo} non-classical monocytes and M2-like macrophages[6, 26, 52, 53]. We found that non-classical monocytes have higher surface expression of CXCR4, therefore yielding them more sensitive to SDF-1α chemotactic signals compared to classical monocytes. These data are in agreement with our recent finding that SDF-1α-directed chemotaxis is higher for non-classical than classical monocytes[6]. Indeed, in the present study we showed that heparin-functionalized hydrogels exhibiting *in vitro* release of SDF-1α over 3 days achieved increased monocyte recruitment to the peri-hydrogel space *in vivo* as early as 1 day compared to internal control. Three days after surgery, more non-classical monocytes were recruited to the aHep^{-N}-SDF gel than the aHep^{-N} gel without SDF-1. Similarly, the ratio of non-classical to classical monocyte was significantly higher under the aHep^{-N}-SDF gel compared to the Hep^{-N} gel less than 8mm away indicating a shift in the local tissue environment from inflammatory to regenerative. These data suggest that the aHep^{-N}-SDF hydrogel achieves a high degree of spatial control in pro-regenerative endogenous cell recruitment that enables continued cellular therapeutic action outlasting SDF-1α release.

Monocytes and monocyte-derived macrophages are key players in promoting angiogenesis and arteriogenesis, making them a desirable endogenous cell source to target for pro-regenerative immunologically smart biomaterials. During inflammatory vascular remodeling, select populations of perivascular monocytes and macrophages contribute paracrine signals to the remodeling vasculature, including secretion of growth factors such as platelet-derived growth factor (PDGF) and VEGF, as well as matrix-remodeling enzymes such as MMPs[30, 45, 48, 51, 55]. Consistent with this supportive role of

monocytes and macrophages in vascular remodeling, we showed in the present study that SDF-1α-releasing aHep-N hydrogels promoted the influx and retention of pro-regenerative monocytes that correlated with enhanced early and sustained arteriogenesis of small arterioles (< 40μm) and enhanced microvascular network density in the tissue surrounding SDF-1α releasing aHep^{-N}-SDF hydrogels. Thus, localized SDF-1α delivery may increase blood flow critical for tissue repair processes, in part through early and selective recruitment of pro-regenerative monocytes. Intravital imaging allowed us to use paired data of change in vessel diameter and immunophenotype of monocytes around the gels. Early arteriolar structural changes correlated with the non-classical:classical monocyte ratio in tissue and the slope of the aHep^{-N}-SDF regression line was higher than internal control. The difference in slope between the internal control and aHep^{-N}-SDF gels could suggest that local SDF-1α further enhances the pro-arteriogenic activity of recruited non-classical monocytes locally through additional functional cues. Indeed, previous reports have suggested that VEGF induces "on-site education" of monocytes upon recruitment, functioning both as a recruitment signal and a knob to tune pro-regenerative function of the arriving cells[30]. Taken together, our data suggest that the aHep^{-N}-SDF hydrogel system is a promising "immune-regenerative engineering" approach to promote vascularization in injured tissue through recruitment of pro-regenerative non-classical monocytes to the injury niche to enable or enhance their therapeutic potential.

3.5. Materials and Methods

3.5.1. Fractalkine aptagel experiments

Aptagel materials

Sequences of the FKN-binding oligonucleotide (FKN-aptamer, 5'-GGGGTGGGTGGGGGGCACGTGTGGGGGCGGCCAGGGTGCT-3') and scrambled oligonucleotide (SCR-aptamer, 5'-CTATCGGCGACATGAACTTTGGCAAGGGCATCTGGTCCAT-3') were obtained from Waybrant *et al*[125]. The oligonucleotides (5'-Acrydite-, amino-modified, or unmodified) and their complementary sequences (CS) were synthesized and purchased from Integrated DNA Technologies. Recombinant human (h), mouse (m) or rat (r) fractalkine protein (with or without BSA carrier), and DuoSet ELISA preparation kits were purchased from R&D Systems. Ammonium persulfate (APS) and N,N,N',N'-trimethylene diamine (TEMED) were purchased from BioRad. Poly(ethylene glycol) diacrylate (PEGDA, M_n = 700) for aptagel synthesis was purchased from Sigma-Aldrich. NHS-activated agarose resin for aptabead synthesis was purchased from ThermoFisher.

Surface Plasmon Resonance

The binding kinetics of the protein-aptamer interactions were assessed by surface plasmon resonance (SPR) on a Biacore T200 instrument at 25 °C in PBS running buffer (Gibco; 2.966 mM $Na_2HPO_4 \cdot 7H_2O$, 1.059 mM KH_2PO_4, 155.172 mM NaCl, pH 7.4). Immobilization of FKN protein to a CM5 sensor surface was performed via amine coupling chemistry at a flow-rate of 5 μL/min, following standard procedures recommended by the manufacturer. Briefly, CM5 sensor surfaces were activated with a 7-min injection of N-Hydroxysuccinimide/1-Ethyl-3-(3-dimethylaminopropyl) carbodiimide hydrochloride

(NHS/EDC), followed by injection of FKN, and deactivation of the surfaces with a 12-min injection of ethanolamine-HCl. For initial screening studies, fractalkine variants (50 μg/mL, 10 mM $NaCH_3COO$ pH 5.0) were injected on separate flow cells for 3-4 minutes to give final immobilization levels of ~2000 RU. For kinetic experiments, FKN variants (10 μg/mL in 10 mM $NaCH_3COO$, pH 5.0) were injected on separate flow cells for 60-90 seconds to give final immobilization levels of ~400 RU for hFKN and ~800 RU for mFKN. Mouse serum albumin (MSA) was employed as a negative surface control. Kinetic evaluation was performed by sequential 3-min injections of varying concentrations (10-1000 nM) of FKN- and SCR-aptamers, followed by a 10-min dissociation phase at a flow rate of 30 μL/min. Surfaces were regenerated between analyte injections with a 30-second injection of 20 mM NaOH, 1 M NaCl. Data analysis and curve fitting of MSA subtracted curves was performed with the Biacore T200 Evaluation Software (v2.0) using the heterogeneous ligand model. Due to the ligand surface density required to achieve sufficient signal detection, rebinding of analytes manifested as a biphasic dissociation curve. However, the fast-kinetic components of each fit accounted for greater than 80% of the observed binding and were reported for each interaction.

Chemistry and Synthesis of Aptagels and Aptabeads

Synthesis of aptamer-functionalized hydrogels was modified from Battig *et al*[150] and Krieger *et al*[27]. Aptagel molds were created by separating two glass slides with 0.5 mm of scotch-tape layered and sealed on the periphery. Acrydite-modified or unmodified aptamers (1 mM stock, 318.5 μM final) were mixed with PEGDA-700 (5% w/v final) and

APS (0.3 M stock, 18 μM final) and the solution was vortexed. TEMED (0.3 M stock, 18 μM final) was added and the solution was quickly injected into the mold. After five minutes, the mold was taken apart, extra liquid was blotted dry, and 2-mm disks were punched out and transferred to PBS in a low-binding 96-well plate for washing. The disks were washed with fresh PBS at least 4 times over 4 hours. Each disk contained ~500 pmol of aptamer. Thus, for 12 to 15 disks (100 μL), the recipe consisted of: 51.70 μL PBS, 4.45 μL PEGDA, 31.85 μL aptamers (1 mM), 6 μL APS (0.3 M) and 6 μL TEMED (0.3 M). For *in vivo* experiments, the glass aptagel molds and PEGDA solution were first sterilized in a UV oven for 30 minutes; APS and TEMED solutions were passed through a 0.22 μm cellulose filter; aptamers were reconstituted in sterile, nuclease-free H2O. Aptagel synthesis took place under a laminar-flow cell culture hood.

Aptabeads were prepared based on instructions provided by the NHS-activated agarose bead manufacturer. Briefly, 5'-amino-modified aptamers were mixed at concentrations of either 0.25 nmol/mg or 1 nmol/mg to batches of 50 mg of dry agarose beads and allowed to conjugate on a rotisserie shaker. Unreacted NHS groups were neutralized with Tris buffer.

Fluorescence Staining and Imaging of Aptagels

Hydrogels either functionalized with acrydite-modified FKN-aptamers, mixed with unmodified aptamers or without aptamers, were stained with fluorescein-tagged (6-FAM) complementary sequence (fCS) to the aptamer. fCS was diluted in 1% BSA 500-fold and the aptagels were incubated on a shaker overnight at room temperature. The aptagels

required washing at length to remove background fluorescence; studies to replicate our findings should begin with a more diluted fCS stain. The aptagels were imaged on a Leica SP5 Confocal Microscope with a 10X objective lens and a 488-nm argon laser. Slices were taken at 6 μm for a total depth of 100 μm. The imaging dimensions were 1920X1920 μm.

In vitro experiments

Experiment paradigm: mFKN was diluted in 1% or 5% BSA to the desired concentration and reverse pipetted into a low-binding 96-well-plate either with or without FKN- or SCR-aptagels. The plate was sealed and placed on a shaker at 300 rpm for 24 hrs. at room temperature. The total solution was then pipetted out and stored as Day 0 (unbound mFKN) samples. The gels were washed in their wells thrice (Fig. S2C) with wash media (1% BSA in phosphate buffered solution) to remove non-specifically bound mFKN. To initiate passive release experiments, fresh solutions of 1% BSA were added and left for 24 hrs. The total solution was removed, stored and replaced with fresh solution each day. Samples were either kept at 4°C if being assayed with ELISA the following day or at -20°C until the assay. One group of aptagels was pre-treated with 25 units of DNAse (ThermoFisher) at 37°C for 1 hour, before beginning the paradigm. All aptagels were studied in at least triplicate or quadruplicate per experiment and the experiments were repeated multiple times.

Protein quantification: Samples were analyzed with ELISA, following the manufacturer's instructions, after diluting them to the detectable range. We reliably observed high sensitivity towards recombinant mFKN and thus primarily report relative

differences between aptagels and controls instead of raw amounts. ELISA plates were read on a SpectraMax i3X Multi-mode plate reader at 450 nm with background subtraction at 570 nm. Duplicate technical replicates were averaged and the blank optical density was subtracted.

Dorsal Skin Window Chamber Surgery and Aptagel Implantation

All animal procedures were conducted per protocols approved by the Georgia Tech Institutional Animal Care and Use Committee. Male C57Bl/6 mice aged 11-15 weeks were anesthetized with vaporized isoflurane at 5% concentration and maintained under anesthesia at 1-3%. Sustained release buprenorphine (1.2 mg/kg, i.p.) was delivered pre-operatively as an analgesic. Dorsal skin was shaved, depilated, and sterilized using ethanol and chlorhexidine. A double-layered skinfold was elevated off the back of the mouse, and the back side of the titanium window chamber frame was surgically fixed to the underside of the skinfold. A circular area (diameter 12 mm) of epidermis and dermis on the top-side of the skinfold was removed using surgical micro-scissors to reveal the vasculature underlying the reticular dermis. Exposed tissue was kept hydrated with sterile saline. The front side of the titanium frame was then mounted on the top of the dissected tissue and attached to its underlying counterpart, and then the dorsal skin was sutured to the two titanium frames. An aptagel was placed near the edge of the window closest to the body, and the chamber was sealed with a sterile glass coverslip. Mice recovered in clean heated cages and received a laboratory diet and water ad libitum throughout the course of the experiment.

Flow Cytometry

Mice were euthanized by CO_2 asphyxiation and the hydrogel was explanted to measure sequestered mFKN via ELISA as described above. 4-mm diameter biopsy punches were used to harvest the dorsal tissue under the gel ("near" region) and tissue on the opposite side of the window ("far" region). Single cell suspensions were generated by mincing the tissue, digesting in collagenase IA (Sigma; C9891) for 45 min at 37˚C, and straining through 40 μm pore filters. Cell suspensions were immunostained using standard flow cytometry techniques. The following antibody panel was used: PerCP/Cy5.5-CD45 (BioLegend; clone 30-F11), APC/Cy7-Ly6G (BioLegend; clone 1A8), PE-MerTK (R&D Systems; clone 108928), BV711-CD64 (BioLegend; clone X54-517.1), BV510-CD11b (BioLegend; clone M1/70), APC-Ly6C (BioLegend; clone HK1.4), BV421-CD11c (BioLegend; clone N418), and BV605-CD206 (BioLegend; clone C068C2). Samples were analyzed using a BD FACS Aria IIIu Cell Sorter. Positive versus negative expression of each marker was determined using fluorescence-minus-one controls derived from excess dorsal tissue. Immunophenotypes were identified as follows: macrophage, $CD45^+$ $CD11b^+$ $CD64^+$ $MerTK^+$; M2-like macrophage, $CD45^+$ $CD11b^+$ $CD64^+$ $MerTK^+$ $CD206^+$; monocyte, $CD45^+$ $CD11b^+$ NOT($CD64^+$ $MerTK^+$) $CD11c^-$ SSC^{lo}; non-classical monocyte, $CD45^+$ $CD11b^+$ NOT($CD64^+$ $MerTK^+$) $CD11c^-$ SSC^{lo} $Ly6C^{lo}$; neutrophil, $CD45^+$ $CD11b^+$ NOT($CD64^+$ $MerTK^+$) $CD11c^-$ $Ly6G^+$ (Fig. S4).

High-dimensional analysis of flow cytometry data

t-Distributed Stochastic Neighbor Embedding (t-SNE) high-dimensional analysis on 9-parameter flow cytometry data was performed. Prior to tSNE dimensional reduction, each sample was pre-gated on $CD45^+CD11b^+$ single cells, and then downsampled to 1000 events in FlowJo Version 10.2. For samples with fewer than 1000 events, no downsampling was performed (the smallest number of $CD45^+CD11b^+$ single cells in a sample was 978). After downsampling, each sample was assigned an electronic barcode and all samples were concatenated to enable generation of a single composite tSNE map that utilized data points from all samples (16 total samples: 4 SCR near, 4 SCR far, 4 FKN near, 4 FKN far). tSNE analysis was performed in FlowJo software using all surface markers and the following parameters: 1000 iterations, 30 perplexity, 200 eta (learning rate), and 0.5 theta.

4D analysis of cell migration dynamics

Male heterozygous B6.129P-Cx3cr1tm1Litt/J (CX3CR1-EGFP) mice were utilized to visualize monocytes and macrophages *in vivo* based on their selective surface expression of CX3CR1. Aptagels were labelled fluorescently via incorporation of Alexa Fluor 647 conjugated, acrydite-modified SCR-aptamer (1% of total aptamer). Time lapse videos of $CX3CR1^+$ cell migration were generated by confocal intra-vital microscopy 7 days after dorsal skin window surgery and aptagel implantation. Briefly, mice were anesthetized using vaporized isoflurane and secured in a heated custom stage, the glass window was removed, and dorsal tissue was irrigated with sterile saline. Aptagels and $CX3CR1^+$ cells were visualized via 633nm and 488nm excitation, respectively, using a 20X water-immersion lens (NA = 1.0) and a Zeiss LSM 710 NLO confocal microscope. Time lapse

z-stacked videos (period = 30s) were acquired near the edges of FKN and SCR aptagels. For 4D analysis in Imaris (Bitplane), cells expressing CX3CR1-EGFP were identified using the surface tool. $CX3CR1^{+}$ surfaces were identified by smoothing with a 2 μm grain size and an automatic threshold on absolute intensity. Touching objects were split using a seed points diameter of 10 μm. $CX3CR1^{hi}$ cells were discriminated from all other $CX3CR1^{+}$ cells by applying a filter to select surfaces with a high fluorescence intensity in the CX3CR1-EGFP channel. To quantify migration dynamics, the automatic cell tracking feature was selected, and track displacement, track length, track straightness, and speed were analyzed.

Statistical Analysis

Statistical analysis was performed in GraphPad Prism. Outliers were identified and removed using Grubbs' test (alpha = 0.05). Sample sizes and statistical tests are stated in each figure legend.

3.5.2. SDF-1α-releasing $aHep^{-N}$ hydrogel experiments

Heparin chemical modification

Heparin sodium salt (Sigma) was reconstituted with distilled, deionized water (ddH_2O) at 10mg/mL and desalted using Dowex 50WX4 resin (mesh size 100-200, Sigma), adding pyridine until the pH reached a value of ~6, as previously described[114]. The

solution was reduced and excess pyridine was eliminated using a rotary evaporator (Buchi) before being flash frozen and lyophilized to yield heparin pyridinium salts. The heparin pyridinium salts were then dissolved in solution of 90% DMSO/10% ddH_2O (v/v) at a concentration of 1mg/mL. The solution was mixed for 2h at 50°C in a rotary evaporator and then cooled on ice and precipitated by an equal volume of 95% ethanol (VWR) saturated with sodium acetate (VWR). The precipitate was centrifuged and washed with ethanol prior to dissolving in distilled water (dH_2O). The solution was dialyzed for 3 days with daily exchanges of dH_2O and then lyophilized (Labconco). Finally, the product was functionalized using a 8.0 molar excess of of N-(3-aminopropyl) methacrylamide hydrochloride (APMAm, Polysciences), N-hydroxysuccinimide (NHS, Acros Organics) and N-3-dimethylaminopropyl)-N'-ethylcarbodiimide hydrochloride (EDC, Sigma) at an acidic pH. After functionalization, the solution was dialyzed and lyophilized again as described previously. The finished product was stored at -20°C until use.

PEG-DA synthesis

Distilled methylene chloride (DCM) was used to dissolve 3.4 kDa PEG in a three neck round-bottom flask and stirred under nitrogen flow. First, triethylamine in DCM at a 1:1 molar ratio with the PEG was added. Subsequently, a 100% molar excess of acryloyl chloride (AcCl) in 15-20mL of DCM was added dropwise. Following the AcCl addition, the system was closed and kept under nitrogen overnight. Potassium carbonate (K_2CO_3) was then added to the solution to remove trimethylamine hydrochloride by-product created in the previous step. After separation of the organic phase, the PEG-DA was precipitated using cold diethyl ether and dried overnight at RT. The finished product was stored at -20°C until use.

Hydrogel fabrication

PEG-DA and N-desulfated heparin (Hep^{-N}) were used as a mixture of 90:10 by weight in all hydrogels. These polymers were UV sterilized and combined at a 10 wt% total solution ratio with sterile phosphate buffered saline (PBS), thermal initiators ammonium persulfate (APS, 0.018M, Sigma) and N,N,N',N'-tetramethylethane-1,2-diamine (TEMED, 0.018M, Sigma), and an amount of GMP-quality bovine serum albumin (BSA, Sigma #A8412) equivalent to 50 wt% of the solution. The solution was then pipetted between two sterile glass slides with an inner clearance of 500μm. The solution was allowed to gel at 37°C for 10 min before the gels were punched out using a 2mm (diameter) biopsy punch (Miltex). The resulting hydrogels were discs of 0.5mm thickness and 2mm diameter.

NMR Analysis of heparin and PEG-DA polymers

Proton nuclear magnetic resonance (^{1}H NMR) was used to characterize the polymers used for hydrogel fabrication (**Figure 16**). Samples of N-desulfated heparin methacrylamide (Hep^{-N} Mam) and poly(ethylene glycol) diacrylate (PEG-DA) were diluted to a concentration of 10 mg/mL with deuterated water (D_2O) and ^{1}H NMR was measured on a Bruker Avance III 400 spectrometer at 400 MHz. To determine the degree of functionalization of the Hep^{-N} MAm derivative, first the contributions of N-acetyl protons in un-functionalized specimens were determined (**Figure 16a**). Subsequently, the ratio of protons donated by methacrylate groups was multiplied by the native N-acetyl groups from unfunctionalized samples (**Figure 16b**). The contribution of native methyl groups in non-methacrylated material was approximately 8-9%. The degree of

functionalization in Hep^{-N} MAm was ~20% for the *in vitro* assays in **Figure 10**. For the characterization of PEG-DA, the presence of acrylate peaks around 5.8-6.4 ppm were observed (**Figure 16c**).

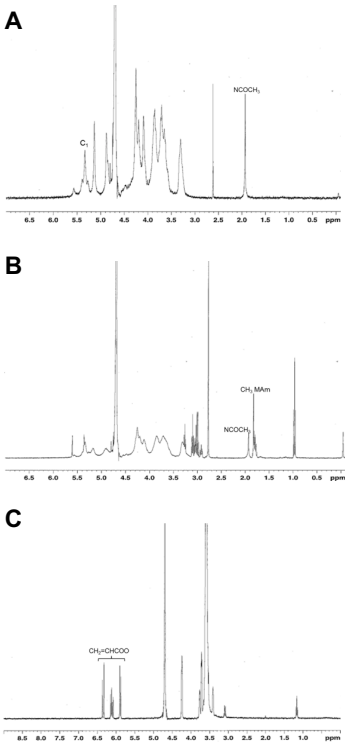

Figure 16. NMR analysis of polymers. (A) NMR spectrum of Hep^{-N} is used to find native N-acetyl contributions from un-functionalized samples. The contribution of native methyl groups in non-methacrylated material is 8-9%. (B) NMR spectrum of Hep^{-N} Mam shows ~20% functionalization of Hep^{-N} polymer with MAm. (C) NMR spectrum of PEG-DA. Acrylate peaks (5.8-6.4ppm) are labeled.

SDF-1α loading and in vitro release

Gels were placed in ultra-low binding 24-well plates and rinsed with PBS for 3h rinse prior to loading with recombinant murine SDF-1α (Peprotech) overnight at 4°C. During this time, each gel was incubated with a 10μL droplet of PBS containing 0.1μg growth factor or no protein (control gels). After loading, the wells were filled with 500μL

of PBS and incubated at 37°C for the release study. PBS was exchanged at appropriate timepoints and stored at -20ºC for subsequent analysis.

In vitro migration

SDF-1α loaded gels (aHep^{-N}-SDF) or albumin loaded control gels (aHep^{-N}) were incubated with 650μL of Iscove's Modified Dulbecco's Medium (Fisher) containing 0.5% fatty acid-free bovine serum albumin (Fisher) for 24h at 37°C. A transwell assay was assembled by transferring hydrogel-conditioned media to the chamber below a 5μm pore size membrane, and seeding $4x10^5$ cells from C57BL/6 mouse bone marrow aspirate on top. After 4h of migration at 37°C and 5% CO_2, migrated cells were stained with DRAQ5 dye according to manufacturer's protocol (Cell Signaling Technologies). Relative migration was quantified by fluorescence intensity using an Odyssey CLx Infrared Imaging System (LI-COR Biosciences).

Chimeric mice

All animal procedures were conducted according to protocols approved by the Georgia Tech Institutional Animal Care and Use Committee. For generation of mice with chimeric EGFP-labeled bone marrow, male C57BL/6 recipient mice, 8-10 weeks of age, were lethally irradiated with a total dosage of 10.5 Gy (5.5-Gy and 5-Gy doses, 3h apart) using an x-ray source (Radsource 2000). Animals were given water supplemented with Baytril for 1 week before and 2 weeks after irradiation and bone marrow cell transplantation. Transplants were performed by injecting $1x10^7$ bone marrow cells harvested from transgenic EGFP (donor) mice into the jugular vein of recipient mice under

inhaled isoflurane anesthesia. Mice were allowed to recover for at least 4 weeks prior to surgery.

Dorsal skinfold window chamber

Male C57BL/6 mice aged 8-12 weeks of age were anesthetized by i.p. injection of a mixture of ketamine (100mg/kg) and xylazine (10mg/kg) in sterile 0.9% saline and surgically fitted with sterile dorsal skinfold window chambers (APJ Trading Co.) as previously described[6, 53, 151, 152]. Briefly, dorsal skin was shaved, depilated, and sterilized via triplet washes of 70% ethanol and chlorhexidine. A double-layered skin fold was elevated off the back of the mouse and the back side of the titanium window chamber frame was surgically fixed to the underside of the skinfold. Surgical microscissors were used to remove the epidermis and dermis from the top-side of the skinfold in a circular area (diameter = 12mm) to reveal the vasculature underlying the reticular dermis. Exposed tissue was kept hydrated with sterile saline. The front side of the titanium frame was then mounted on the top of the dissected tissue and attached to its underlying counterpart. The dorsal skin was sutured to the two titanium frames, and the exposed tissue was sealed with a protective sterile glass coverslip. Mice were allowed to recover in heated cages and administered sustained release buprenorphine via i.p. injection as a postoperative analgesic. All mice received a laboratory diet and water *ad libitum* throughout the course of the experiment.

Hydrogel placement and intra-vital brightfield microscopy

Hydrogels were implanted into the window chamber on the day of surgery (day 0). Mice were anesthetized via inhaled isoflurane, the glass window was removed and dorsal

tissue was flooded with 1mM adenosine in Ringer's solution to maximally dilate all vessels and maintain tissue hydration. The mouse was then mounted to a custom microscope stage mount and imaged noninvasively at 5X magnification on a Zeiss Imager.D2 microscope with AxioCam MRc 5 color digital camera (Carl Zeiss). Images were acquired on day 0 immediately preceding hydrogel implantation and again on day 3 or 7 according to experimental design. Mice were implanted with one Hep^{-N} internal control hydrogel and one $aHep^{-N}$ experimental hydrogel (unloaded or loaded with SDF-1α) placed on opposite sides of the window.

Changes in microvascular length density

Microvascular length density measurements were made by intravital brightfield microscopy and whole mount immunofluorescence. A 4mm (diameter) region of interest circumscribing the hydrogel and tangential to the gel edge was selected as indicated in **Figure 17**. Vessels visible within these cropped images were traced and total vessel length per unit area was quantified using ImageJ.

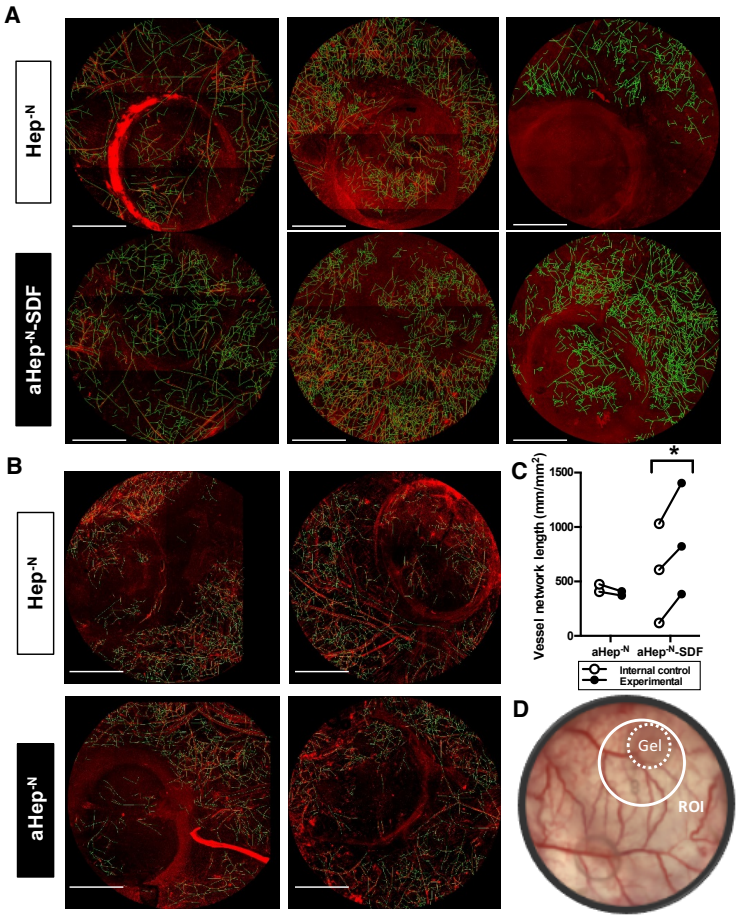

Figure 17. Analysis of CD31+ microvessels. (A-B) CD31+ vessels were visualized by whole mount immunofluorescence microscopy at day 7 and traced to quantify length of the microvascular network. (C) aHep^{-N}-SDF hydrogels significantly increase microvascular network length compared to internal control while aHep^{-N} controls show no change. (Scale bar = 1 mm). (D) Region of interest is 4mm diameter circle circumscribing the gel.

Measurement of change in arteriolar diameter

To measure changes in arteriolar diameter, arteriole–venule pairs were identified within a 3mm radius of the center of each gel. Arterioles and venules were identified on the basis of size and morphology at day 0; venular diameters were larger than arteriolar diameters on day 0. Internal diameters based on blood column width in brightfield images

were measured using Zen Blue (Zeiss) and recorded longitudinally for each vessel segments on day 0 and 3 or day 0 and 7 (**Figure 18**). Day 0 diameter measurements were used to bin vessels less than 40µm in diameter[129]. This metric is limited to vessels visible at both time points (1-4 vessels/gel).

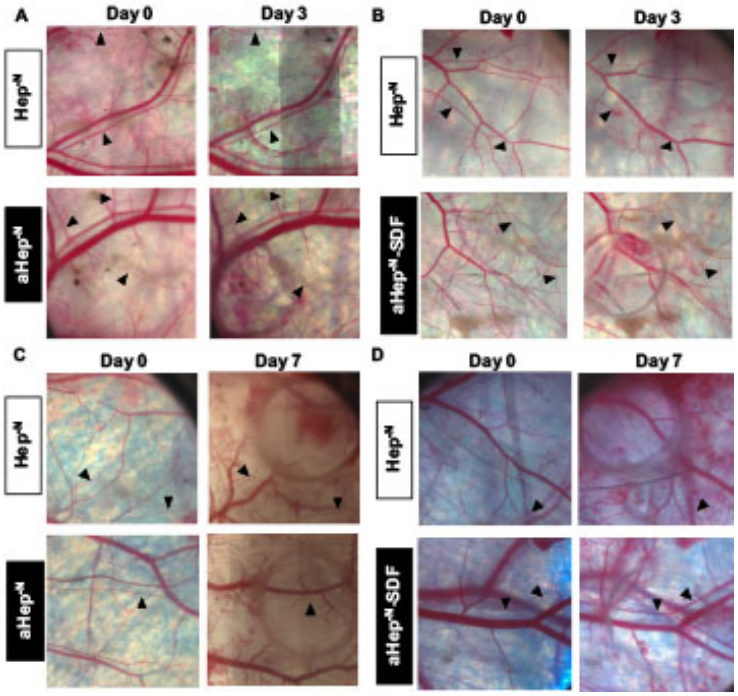

Figure 18. Representative intravital microscopy of arteriolar remodeling. Change in lumenal diameter of arterioles (arrowheads) is negative for internal controls and aHep^{-N} control and positive for aHep^{-N}-SDF hydrogels at (A, B) day 3 and (C, D) day 7. (Scale bar = 1 mm).

Hydrogel removal, tissue harvest, and preparation for single-cell suspensions

To visualize the recruitment of cells to the hydrogel interface, hydrogels were explanted onto glass slides and imaged at 5X magnification. For subsequent flow cytometry analysis, cells were then removed from the hydrogel surface by incubation with

trypsin for 10min at 37°C and combined with a fixed volume of flow cytometry counting beads for quantification of relative cell number, CountBright^{TM} Absolute Counting Beads (Life Technologies). To measure the recruitment of cells to tissue by day 3, the dorsal tissue was bisected along the midline separating the hydrogels, digested with 1mg/mL collagenase at 37°C, and further disaggregated with a cell strainer to create a single cell suspension.

Flow cytometry

Immuno-staining and flow cytometry analyses were performed according to standard procedures and analyzed on a FACS-AriaIIIu flow cytometer (BD Biosciences). The following antibodies were used for cell phenotyping: APC/Cy7-conjugated anti-CD11b (BioLegend, M1/70), APC-conjugated anti-Ly-6C (BioLegend, HK1.4), and PE- or PerCP/Cy5.5-conjugated anti-CXCR4 (eBiosciences, 2B11). $CD11b^{+}SSC^{low}Ly\text{-}6C^{high/low}$ monocyte populations were confirmed to be $Ly\text{-}6G^{neg}$.

Whole mount immunohistochemistry and intravital confocal microscopy

Mouse vasculature was perfused with warm 0.9% saline and then 4% PFA until tissues were fixed. Dorsal tissue was explanted and drop-fixed in 4% PFA for 10min, permeabilized with 0.2% saponin in PBS for 16-24h at 4°C, blocked with 10% mouse serum in PBS for 16-24h, and stained with combinations of the following monoclonal antibodies diluted into a solution of 0.5% BSA, 5% mouse serum, and 0.1% saponin in PBS: Cy3-conjugated anti-α-smooth muscle actin (αSMA, 1:300, Sigma), AF594-conjugated anti-CD31 (1:100, BioLegend), AF647-conjugated anti-CD68 (1:200, AbD Serotec), and AF488-conjugated anti-CD206 (1:200, AbD Serotec). Images of dorsal tissue

vessel networks were acquired as 3-dimensional z-stacked tile scans in confocal and multiphoton modes using a Zeiss LSM710 NLO microscope, Ti:Sapphire pulsed IR laser, and 5X, 10X, or 20X magnification. Male heterozygous B6.129P-*Cx3cr1*^{tm1Litt}/J (CX3CR1-EGFP) mice were utilized to visualize monocytes in live mice based on their selective surface expression of CX3CR1[6, 34]. Intravital confocal visualization of CX_3CR1^{high} and CX_3CR1^{+} cells in/near peri-implant venules was performed in (CX3CR1-GFP) knock-in transgenic mice after jugular vein injection of rhodamine-conjugated isolectin B_4 (0.1mg/50μL; Vector Laboratories) to visualize perfused vasculature on day 1 after surgery. One 20X region of interest adjacent to each gel implant was imaged on day 1 after surgery and immediately after infusion of fluorescently tagged lectin to visualize vessels. Intravital confocal imaging was conducted with a 20X water immersion objective (NA=1.0). CX_3CR1^{+} cell numbers were quantified using Fiji and 3D surface rendering was performed in Imaris (Bitplane).

Statistical analysis

Data are presented as mean ± standard error of the mean (SEM) unless otherwise indicated. Paired data for internally controlled studies were analyzed in paired *t*-tests or by ANOVA with repeated measures. Multiple comparisons were made by one- or two-way ANOVA followed by Bonferroni or Sidak post-tests to compare means. Linear regression analysis was performed separately on the internal control group and experimental group and r^2 values are reported. All statistical analysis was done in GraphPad Prism software. Unless otherwise noted, $p<0.05$ was considered statistically significant.

4. SYNERGY BETWEEN CHEMOKINE AND SPHINGOLIPID SIGNALS IN MONOCYTE RECRUITMENT AND VASCULARIZATION OF INJURED SKIN[2]

4.1. Abstract

The immune response to biomaterial implants critically regulates functional outcomes such as vascularization, transplant integration/survival, and fibrosis. To create "immunologically smart" materials, the host-material response may be engineered to optimize the recruitment of pro-regenerative leukocyte subsets which mature into corresponding wound healing macrophages. We have recently identified that a unique feature of pro-regenerative Ly6C^{low} monocytes is a higher expression of both the bioactive lipid receptor sphingosine-1-phosphate receptor 3 (S1PR3), and the stromal derived factor-1α (SDF-1α) receptor, CXCR4. Therefore, we designed a bi-functional hydrogel to harnesses a mechanistic synergy between these signaling axes to enhance the recruitment of endogenous pro-regenerative monocytes. To overcome the challenge of co-delivering two physiochemically distinct molecules—a large hydrophilic protein and hydrophobic small molecule—we engineered a dual affinity hydrogel that exploits the growth factor affinity of a modified heparin (Hep^{-N}) and lipid chaperone activity of albumin. The sphingosine analog FTY720 and SDF-1α are successfully loaded and co-released from the

[2] Adapted from: M.E. Ogle, J.R. Krieger, L.E. Tellier, J. McFaline-Figueroa, J.S. Temenoff, E.A. Botchwey, Dual Affinity Heparin-Based Hydrogels Achieve Pro-Regenerative Immunomodulation and Microvascular Remodeling, ACS Biomaterials Science & Engineering (2017). Reprinted by permission of ACS Publications.

Hep^{-N}-functionalized PEG-DA hydrogels while maintaining bioactivity. Placement of these hydrogels into a murine partial thickness skin wound demonstrates that co-release of FTY720 and SDF-1α yields superior recruitment of myeloid cells to the implant interface compared to either factor alone. While *in vivo* delivery of FTY720 or SDF-1α individually promotes the enhanced recruitment of Ly-$6C^{low}$ non-classical monocytes, co-delivery enhances the early accumulation and persistence of the differentiated wound healing $CD206^{+}$ macrophages in the tissue surrounding the gel. Co-delivery similarly promoted the synergistic expansion of vasculature adjacent to the implant, a key step in tissue healing. Taken together these findings suggest that the combination of chemotactic molecules may provide additional maturation signals to the infiltrating leukocytes to facilitate macrophage transition and vascular network expansion, thus, ultimately, potentiating tissue repair. The coupling of multiple pro-regenerative biological cues provides a foundation for more fine-tuned immunoregenerative modulation to facilitate tissue repair.

4.2. Introduction

Endogenous inflammatory response in sterile injury and tissue trauma is characterized by the infiltration of circulating mononuclear phagocytes to clear debris, remodel extracellular matrix and vasculature, and signal to circulating and parenchymal cells that help restore the native cellular and matrix composition[10]. Loss of function studies show that early myeloid cell input is critical for effective repair of tissue injury in the complex tissue regeneration models of the salamander limb and zebrafish tail fin[12, 153]. Monocytes and their macrophage progeny participate in processes of

angiogenesis[48] and arteriogenesis[52] while orchestrating healing across myriad injury contexts including liver[31], kidney[154], cardiac and skeletal muscle[1, 61, 134, 155], and peripheral nervous tissue[2, 5, 70]. Circulating blood monocytes are comprised of at least two functionally distinct subsets[34] and the inflammatory index, or balance of regenerative to inflammatory myeloid cells, in the tissue is correlated with the healing outcome[2, 6, 27, 156]. Classical monocytes are characterized by high Ly6C and low CX3CR1 surface expression in mice and $CD14^{+}CD16^{-}$ in humans. Non-classical monocytes express low levels of Ly6C and high CX3CR1 in mice and $CD14^{low}CD16^{+}$ in humans[34]. Monocyte-derived macrophages similarly exhibit functional and phenotypic heterogeneity with a spectrum of M1 "inflammatory" to M2 "regenerative" macrophages and the dominant presence of M2 versus M1 macrophages is related to positive healing outcomes[10]. Biomaterial-mediated strategies to change the inflammatory index of the tissue improves metrics of regeneration[2, 6, 27, 28]; therefore, development of materials that can effectively control the recruitment, polarization, and activity of myeloid cells presents an opportunity for supporting a powerful endogenous repair system[6, 27].

Controlled drug delivery can facilitate spatial and temporal control over presentation of biological or pharmacological factors within a wounded tissue. Using biomaterials to produce *in vivo* gradients of immunomodularory cues can facilitate recruitment of endogenous pro-regenerative cells to the injury microenvironment[10, 27, 53]. To control the frequency and selectivity of endogenous inflammatory cell recruitment, we have investigated receptor signaling axes that govern selective recruitment of monocyte subsets. Two such control points for manipulating the balance of functional phenotypes of monocytes/macrophages within inflamed tissues are the bioactive lipid receptor

sphingosine 1-phosphate receptor 3 (S1PR3) and CXC-type chemokine receptor 4 (CXCR4)[6, 27, 53]. Non-classical monocytes display a higher expression of S1PR3[6] and CXCR4[27] at the cell surface compared to classical monocytes. Following inflammatory injury, upregulation of stromal derived factor-1α (SDF-1α), the natural ligand of CXCR4, promotes tissue repair in part by attracting and retaining myeloid cells near vessels to coordinate leukocyte-assisted angiogenesis and arteriogenesis[55, 157]. Antagonism of CXCR4 during the injury response leads to a significant reduction in recruited myeloid cells and a failure of neovascularization[55]. Localized biomaterial-mediated delivery of exogenous SDF-1α enhances the recruitment of non-classical monocytes to inflamed tissue vasculature and concomitant expansion of microvascular networks within the injury niche[27]. Similarly, delivery of FTY720, a small molecule agonist of S1PR3, from degradable polymers stimulates selective recruitment of non-classical monocytes from blood and their pro-regenerative on-site education, as indicated by their strategic perivascular positioning, attenuated secretion of inflammatory cytokines, and differentiation to $CD206^+$ M2 macrophages[6]. Molecular cross-talk between S1PR3 and CXCR4 evidenced by transactivation of CXCR4 upon S1PR3 stimulation in endothelial progenitor cells suggests potential synergy between these axes for chemotaxis[158]. Stimulation of S1PR3 also enhances CXCR4-mediated chemotaxis of non-classical monocytes toward SDF-1α, whereas classical monocytes fail to migrate robustly toward SDF-1α[6]. S1PR3 agonism enhances CXCR4 activation in endothelial progenitor cells, thereby enhancing their homing efficacy in the treatment of hind limb ischemia[158]. These results suggest that dual stimulation of S1PR3 and CXCR4 signaling axes *in vivo* through localized gradient release within an inflammatory injury niche would

promote synergistic recruitment of pro-regenerative monocytes/macrophages and enhance microvascular growth and remodeling[10, 27, 157].

To investigate the functional synergy of the CXCR4 and S1PR3 signaling axes, we engineered a dual-affinity heparin-based biomaterial carrier to co-release SDF-1α and S1P receptor targeted small molecule FTY720. Heparin is a glycosaminoglycan that binds cationic proteins such as SDF-1α and protects them from denaturing conditions[114, 115, 117]. We have previously demonstrated that matrices functionalized with a heparin derivative protect proteins against denaturation to maximize bioactivity and lower the payload requirement for *in vivo* efficacy[113, 114]. To reduce the anti-coagulant activity of heparin for safe use *in vivo*, we incorporated a cross-linkable heparin derivative that was selectively desulfated at the -N position (Hep^{-N})[114] within a poly(ethylene glycol) diacrylate (PEG-DA) network. To overcome the physiochemical disparities between SDF-1α, a 10 kDa hydrophilic protein, and FTY720, a 307 Da hydrophobic small molecule lipid, the scaffolds were further engineered for dual affinity by encapsulation of albumin within the matrix during crosslinking ($aHep^{-N}$) as an affinity-based carrier for the small molecule FTY720 due to its endogenous chaperone binding capacity for bioactive lipids[159].

In this study, we investigated inflammatory and arteriogenic responses to $aHep^{-N}$-PEG-DA hydrogel implants releasing either SDF-1α or FTY720 or both factors combined. We show that SDF-1α and FTY720 are co-released from $aHep^{-N}$-PEG-DA gels over several days *in vitro*. The dorsal skinfold window chamber model, a mouse model of excisional skin injury, was used to longitudinally assess the recruitment of innate immune cells and associated microvascular network expansion. Synergy between SDF-1α and

FTY720 was observed with regard to leukocyte attachment to the implant surface and structural enlargement of arterioles in the peri-implant tissue. Accumulation of macrophages in the early phase of repair and wound-resolving macrophages in the later phase was enhanced by co-delivery of SDF-1α and FTY720 compared to either factor alone. These results suggest an exciting potential of the aHep^{-N}-PEG-DA hydrogel technology to release multiple distinct biomolecular cues and locally tune the innate immune response in favor of regeneration.

4.3. Results

4.3.1. aHep^{-N}-PEGDA hydrogels co-release bioactive SDF-1α and FTY720 in vitro

The sphingosine analog FTY720 enhances the migration of non-classical monocytes toward an SDF-1α gradient *in vitro[6]*. To harness this biological synergy, we sought to develop a biomaterial that could release both the small molecule FTY720 and the protein SDF-1α to locally deliver these agents *in vivo*. Hydrogels containing a heparin derivative and embedded with albumin were engineered to sequester and release these physiochemically distinct biomolecules. The albumin provides an affinity carrier for small bioactive lipids or small molecule analogs such as FTY720[159], while the heparin derivative provides a platform for loading and stabilizing heparin-binding growth factors[27, 114, 115]. The fabrication and composition of aHep^{-N} hydrogels encapsulating the chemokine protein SDF-1α and hydrophobic small molecule FTY720 are shown in **Figure 19a**. The dual loaded gels release 24.9 +/- 7.2 % of total SDF-1α payload by day 1

and 26.0 +/- 0.2 % by day 7 *in vitro* (**Figure 19b**); while 43.0 +/- 4.0 % of FTY720 is released by day 1 and 87.2 +/- 2.1% by day 7 (**Figure 19b**). Both FTY720 and SDF-1α released from the gels maintain bioactivity as illustrated by their ability to induce chemotaxis of primary murine bone marrow cells toward 24h hydrogel-conditioned media in an *in vitro* transwell migration assay. Media conditioned by gels releasing SDF-1α induced a 1.5-fold increase in chemotaxis compared to control gels containing only embedded albumin, while gels releasing both FTY720 and SDF-1α induced a 2.0-fold increase compared to control (**Figure 19c**).

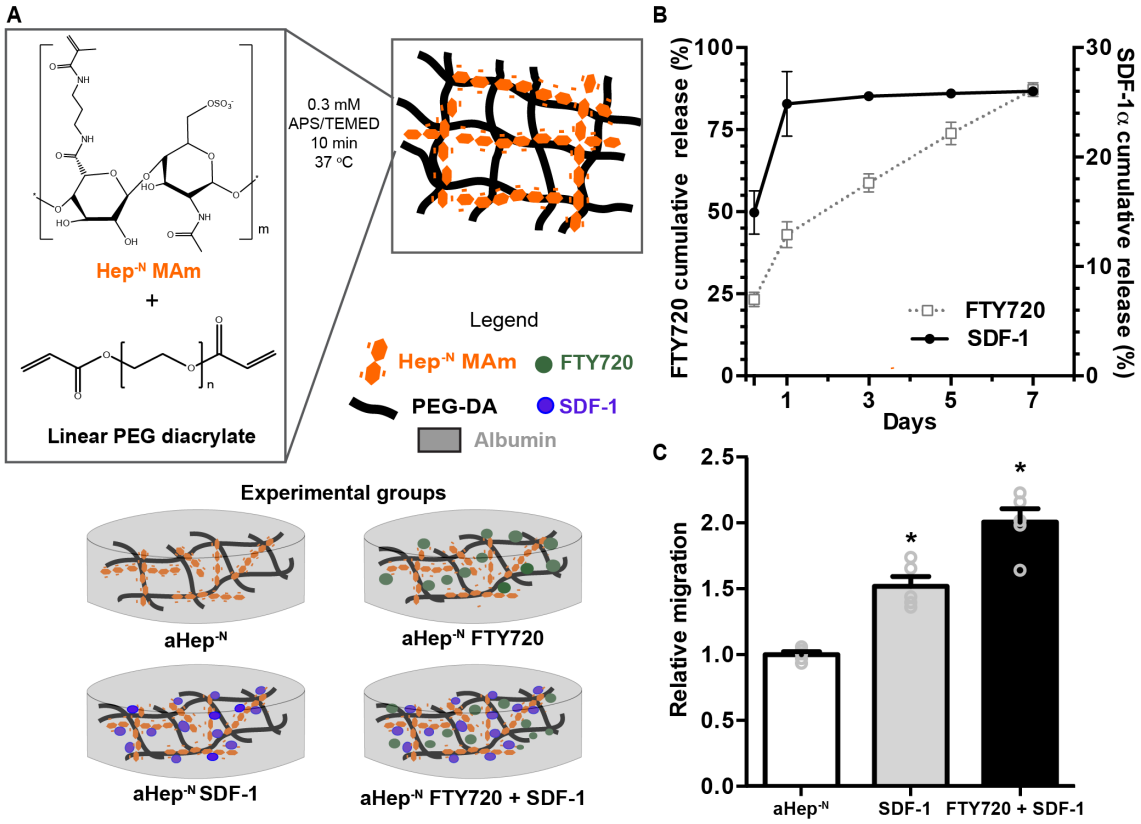

Figure 19. Hep^{-N}-PEG-DA hydrogels co-release bioactive SDF-1α and FTY720 in vitro. (A) Fabrication and post-gelation loading of SDF-1α and/or FTY720 into albumin-embedded Hep^{-N}-PEG-DA gels (aHep^{-N}). (B) SDF-1α and FTY720 are released over 7

days in vitro (n= 6 gels, 2 independent studies). (C) *In vitro* migration of primary murine bone marrow cells toward media conditioned by 24h of hydrogel release. *Indicates significance compared to all other groups (n=5, ANOVA, $p<0.05$).

4.3.2. Dual release of SDF-1α and FTY720 from aHep^{-N}-PEG-DA hydrogels promotes synergistic recruitment of leukocytes to the gel surface

To measure the ability of aHep^{-N}-PEG-DA gels to recruit endogenous cells *in vivo*, we utilized the dorsal skinfold window chamber model, a mouse model of excisional skin injury that enables intra-vital microscopic (IVM) assessment of host responses to biomaterial implants, including microvascular remodeling and associated recruitment of immune cells. aHep^{-N} gels were implanted in wild-type C57Bl/6 mice for 3 days and explanted for analysis of cell recruitment to the implant-tissue interface. Brightfield microscopy of explanted gels reveals increased cell attachment to the surface of gels co-releasing SDF-1α and FTY720 compared to either factor alone or unloaded control (data not shown). Cells were digested from the gel surface and characterized by flow cytometry. Recruitment of myeloid leukocytes (CD11b^{+}) is greatest in response to co-delivery of FTY720 and SDF-1α in a pattern that indicates synergy between these two molecules (**Figure 20a**). Myeloid leukocytes (CD11b^{+}) expressing the SDF-1α receptor (CXCR4) exhibit a similar, but non-significant, pattern of synergy in recruitment to the gel indicating that the responding cells may be equipped to respond to SDF-1α released from the gel (**Figure 20b**).

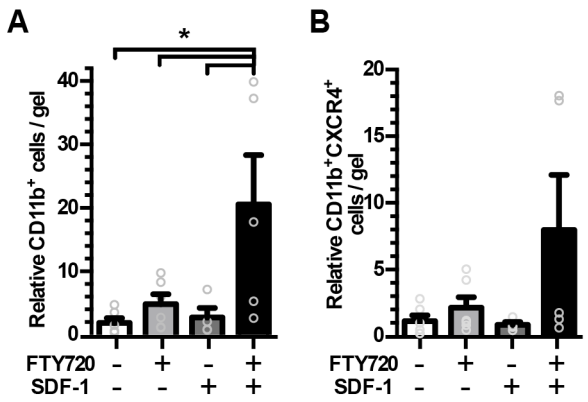

Figure 20. Dual release of SDF-1α and FTY720 from aHep^{-N}-PEG-DA hydrogels promotes synergistic recruitment of leukocytes to the gel surface. Gels were implanted in the dorsal skin window chamber for 3 days and explanted to evaluate cell association with the gel by flow cytometric analysis of (A) CD11b^{+} and (B) CD11b^{+}CXCR4^{+} populations. (n= 5-6, ANOVA, *p<0.05)

One day after implantation of either an unloaded Hep^{-N} gel or an aHep^{-N} gel co-releasing FTY720 and SDF-1α into CX3CR1$^{GFP/+}$ mice that allow the tracking of myeloid cells by GFP fluorescence, myeloid cells can be seen extravasating and migrating in the tissue adjacent to each gel (**Figure 21a**). Cells in the peri-implant region of the dual releasing gel had a greater displacement (**Figure 21c**) and directional migratory patterns compared to cells in the peri-implant region of the unloaded Hep^{-N} gel (**Figure 21e**) suggesting that the dual affinity gel alters the migratory behavior of infiltrating myeloid cells.

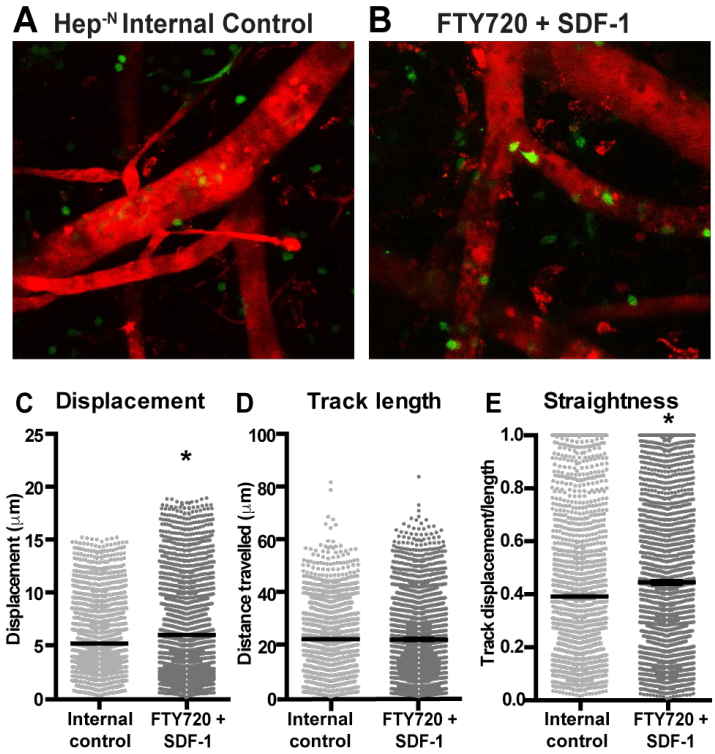

Figure 21. Myeloid cells have greater directional motility around dual releasing gel. Myeloid cell movements were captured by intra vital microscopy of the dorsal window chamber in the CX3CR1$^{GFP/+}$ transgenic mouse model one day after surgery and gel implantation. Myeloid cells (green) and vessels (red) were visible adjacent to the unloaded Hep^{-N}-PEG-DA internal control gel (A) and the dual releasing aHep^{-N}-PEG-DA SDF + FTY720 gel (B) in the same window chamber. Fifteen minute videos were acquired and cell tracking analysis was done in IMARIS software. Cell displacement (C) was enhanced in the region surrounding the experimental gel but not track length (D), suggesting that the cells are traveling in a straighter and more directed path (E). (n=2 mice, 2 regions of interest each, Mann-Whitney rank test, *$p<0.05$)

4.3.3. Recruitment of mononuclear phagocyte subsets to tissue surrounding aHep^{-N}-PEG-DA gels

To assess the immunophenotypes of recruited cells in the tissue surrounding each gel at day 3, a 4mm biopsy of dorsal tissue under the hydrogel was harvested and digested

for flow cytometric analysis. We have previously shown that non-classical monocytes ($Ly6C^{low}$) can be functionally distinguished from classical monocytes ($Ly6C^{high}$) by higher surface expression of CXCR4 and S1PR3[6, 27]. In the present study, recruitment of non-classical monocytes to the peri-implant tissue increased approximately 1.5-fold in response to delivery of either FTY720 or SDF-1α alone compared to animals implanted with the albumin containing control gel; however, co-delivery of FTY720 and SDF-1α did not significantly increase non-classical monocyte recruitment (**Figure 22a**).

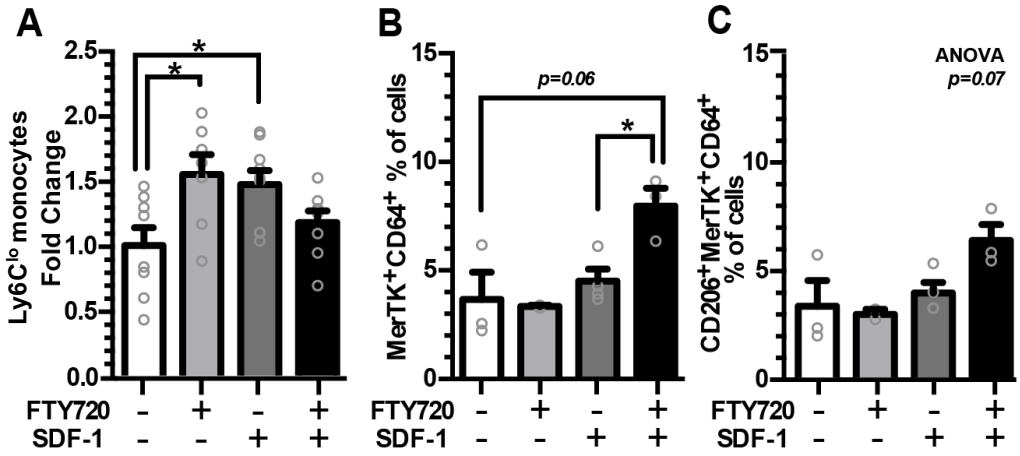

Figure 22. Recruitment of mononuclear phagocyte subsets to tissue surrounding aHep^{-N}-PEG-DA gels. Tissue surrounding the hydrogel was analyzed 3 days after surgery and implantation for the immunophenotype of the recruited myeloid populations. (A) Either FTY720 or SDF-1α lead to an increase in non-classical monocyte ($SSC^{low}CD11b^{+}Ly6C^{low}$) recruitment to the gel as a percent of monocytes ($SSC^{low}CD11b^{+}$) (n=7-9, ANOVA, *p<0.05). (B) Dual release of FTY720 and SDF-1α significantly increased the presence of $MerTK^{+}CD64^{+}$ macrophages within the tissue as a percent of total cells (n=2-4, ANOVA of control, SDF-1, and FTY720/SDF-1 groups (FTY720 excluded due to low sample size)). (C) Dual release similarly produced a trend of increased $CD206^{+}MerTK^{+}CD64^{+}$ cells as a percent of total cells (n=2-4, ANOVA of control, SDF-1, and FTY720/SDF-1 groups (FTY720 excluded due to low sample size), p=0.07).

4.3.4. Dual release of SDF-1α and FTY720 increases abundance of M2-like macrophages

Although both FTY720 and SDF-1α both individually increased recruitment of non-classical monocytes to the tissue adjacent to the hydrogel, the dual delivery gel did not exhibit the expected synergy of localized non-classical monocyte recruitment in these two chemotactic signaling axes. Previous studies suggest that non-classical monocytes recruited by FTY720 can differentiate into $CD206^{+}$ wound healing macrophages within the injury niche[6]. We hypothesized that co-delivery of FTY720 and SDF-1α may support an accelerated monocyte-to-macrophage differentiation prior to the day 3 time point. In agreement with this hypothesis, co-release of FTY720 and SDF-1α increased the abundance of macrophages ($MerTK^{+}CD64^{+}$)[160, 161] in tissue surrounding the implanted biomaterial at day 3 (**Figure 22b**). The abundance of $CD206^{+}MerTK^{+}CD64^{+}$ macrophages out of total cells at day 3 followed an increasing trend that paralleled the increase in total macrophages (**Figure 22c**).

To further investigate this finding, we assessed *in situ* macrophage accumulation at later stages of repair by complementary microscopy techniques. The $CX3CR1^{GFP/+}$ transgenic mouse model was selected to enable intra vital microscopic visualization of monocyte and macrophage populations based on GFP expression and cell morphology (**Figure 23a**)[41, 162]. Implantation of SDF-1α or dual-loaded gels in the $CX3CR1^{gfp/+}$ mouse followed by confocal intra vital microscopy at day 6 revealed phenotypic differences in CX3CR1-GFP+ cell accumulation and morphology. The SDF-1α group had a higher proportion of rounded monocytes identified as CX3CR1-GFP+ (**Figure 23b,d**), whereas the dual release FTY720 + SDF-1α group was enriched in CX3CR1-GFP^{dim} and

more elongated cells, features that are consistent with macrophage morphology[41] (**Figure 23c,e**).

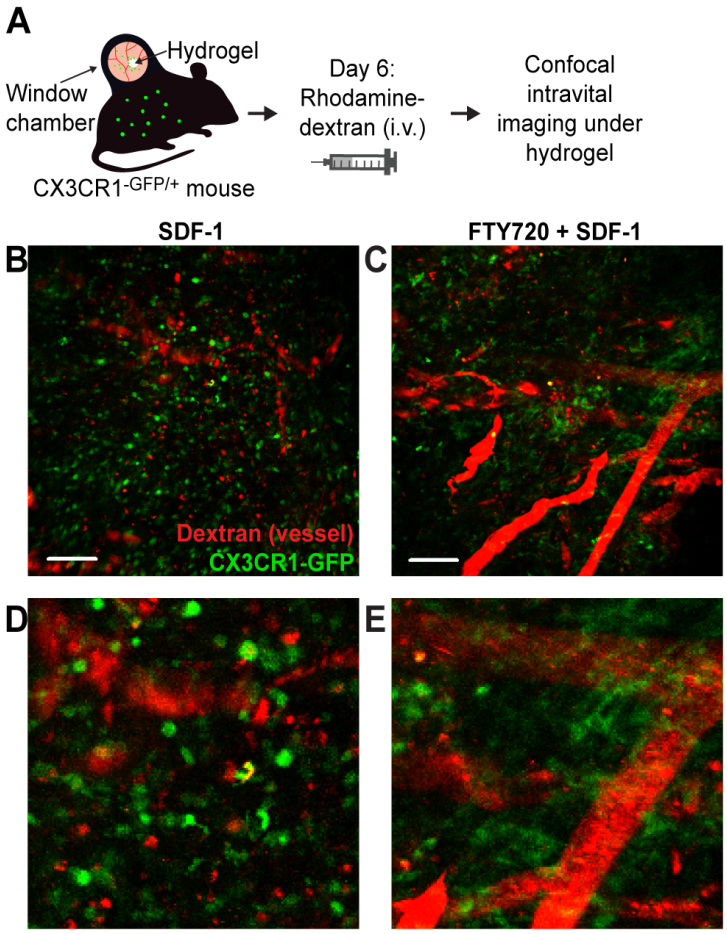

Figure 23. Dual release of SDF and FTY720 alters CX3CR1+ cell morphology. (A) CX3CR1$^{-GFP/+}$ mice were fitted with a dorsal window chamber and after six days were injected (i.v.) with rhodamine-dextran to visualize perfused vessels. Confocal intravital imaging was then conducted in the region directly surrounding the hydrogel implant. (B, D) Tissue surrounding the SDF hydrogel had rounded CX3CR1-GFP+ cells surrounding the vasculature, while tissue surrounding the SDF + FTY720 hydrogel (C, E) had CX3CR1^{dim} myeloid cells with elongated morphology consistent with macrophage phenotype. Scale bar 100μm. (representative images from n=3 ROI per gel)

Whole-mount immunohistochemistry in wild-type C57Bl/6 mice at day 7 (**Figure 24a**) revealed increased accumulation of CD68^{+}CD206^{+} wound-healing macrophages in

the tissue surrounding gels co-releasing FTY720 + SDF-1α compared to either factor alone or control (**Figure 24b**). A higher proportion of $CD68^+$ cells were also $CD206^+$ in the dual treatment group (**Figure 24c**). Taken together, these results suggest that co-release of FTY720 and SDF-1α increases the early accumulation of $CD68^+CD206^+$ wound-healing macrophages compared to release of either factor alone.

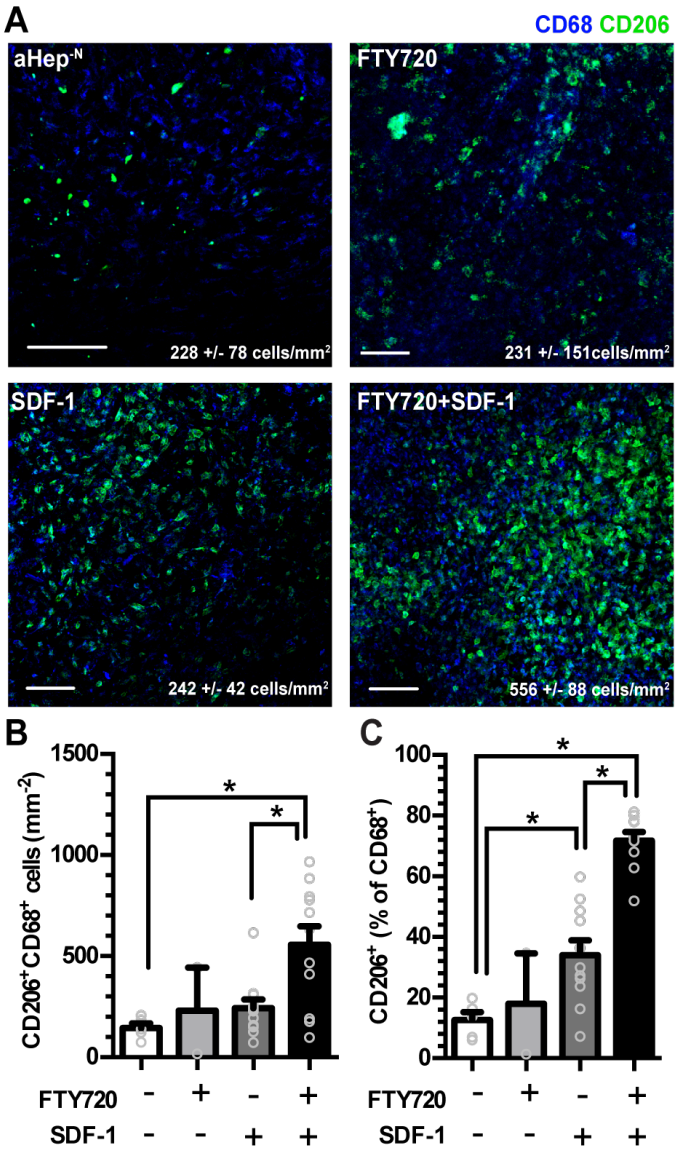

Figure 24. Dual release of SDF-1 and FTY720 increases abundance of $CD206^+$ macrophages. (A) Whole-mount IHC and confocal microscopy shows accumulation of

$CD68^+$ macrophages and $CD206^+CD68^+$ macrophages in tissue proximal to the gels at day 7 (CD206, green; CD68, blue scale bar 100μm). (B-C) Quantification of $CD206^+CD68^+$ macrophages (n= 2-3 mice, 2-11 ROI each, ANOVA, *$p<0.05$).

4.3.5. Dual release of SDF-1α and FTY720 synergistically increases the caliber of arterioles in tissue surrounding aHep^{-N}-PEG-DA gels

Mononuclear phagocytes serve a prominent regulatory role in arteriogenesis, which is critical to restoring perfusion to ischemic tissues[52, 129, 163]. To determine whether recruitment of pro-regenerative monocyte and macrophage populations by dual-loaded $aHep^{-N}$ gels is associated with enhanced arteriogenesis, we assessed the change in diameter of arterioles in the tissue surrounding $aHep^{-N}$ gels (**Figure 25a**). At day 3 during the acute phase of healing, FTY720-releasing gels cause a mean decrease in arteriolar diameter of -21.7% while SDF-1α-releasing and co-releasing gels stimulate an increase of 20.1% and 25.4%, respectively (**Figure 25b**). At day 7 during the later phase of healing, gels co-releasing FTY720 + SDF-1α stimulated greater arteriolar diameter enlargement (**Figure 25c**). In addition, the dual releasing gel produced a more densely packed network of microvasculature compared to an internal control Hep^{-N} gel implanted in the same window chamber (**Figure 25d,e,f**). Taken together, these data demonstrate that co-release of FTY720 and SDF-1α from bi-functional $aHep^{-N}$-PEG-DA gels provides a regenerative environment that supports the recruitment of $CD206^+$ macrophages and a coordinate increase in vascular remodeling.

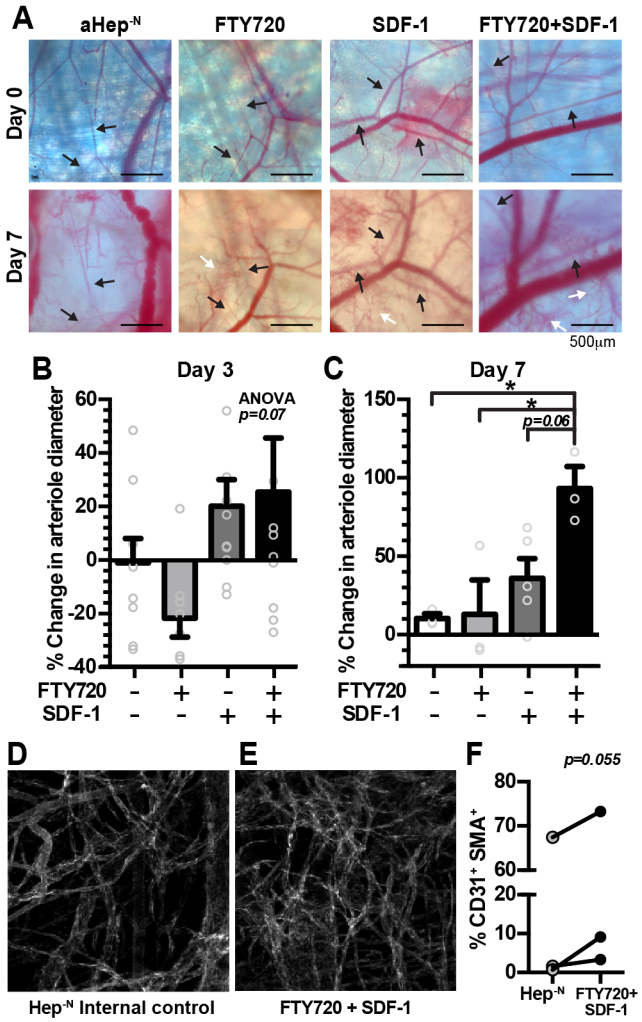

Figure 25. Dual release of SDF-1α and FTY720 synergistically increases the caliber of arterioles in tissue surrounding Hep^{-N}-PEG-DA gels. (A) Brightfield intravital microscopy was used to measure enlargement of arterioles in the microcirculation surrounding implanted gels at day 3 (B) and day 7 (C) (ANOVA, *$p<0.05$, n=8-10 at day 3, n=3-5 at day 7). (D-F) Whole mount immunofluorescent imaging of vessels (CD31+SMA+) surrounding unloaded control gels or aHep^{-N}-FTY720 + SDF-1 gels within the same window chamber (n=3).

4.4. Discussion

The immune response to biomaterial implants critically regulates functional healing outcomes such as vascularization, tissue regeneration, transplant integration, and extent of

fibrosis. By mimicking the presentation of natural inflammatory and regenerative signals, we have an opportunity to engineer the host-material interaction in the design of "immunologically smart" materials. Due to the complexity of the immune response, materials that can release multiple complementary factors are likely necessary to fine tune an engineered inflammatory response. We have previously shown that either SDF-1α or FTY720 released in a localized gradient from a biomaterial can support the enhanced recruitment of $Ly6C^{low}$ non-classical monocytes and improved vascular remodeling. The inflammatory process is inherently complex and dynamic; tissues and infiltrating inflammatory cells integrate and respond to a multiplicity of signals which may be enhanced by localized release of multiple complementary therapeutic agents[23]. To move toward higher level of control of the local inflammatory environment, we have developed a bi-functional hydrogel that targets a mechanistic synergy between chemokine protein SDF-1α and the S1P signaling axis to enhance the recruitment and behavior of endogenous pro-regenerative leukocytes. Dual affinity $aHep^{-N}$-PEG-DA hydrogels were engineered to achieve simultaneous *in vivo* release of SDF-1α and FTY720 with the goal of modulating local innate immunity to promote vascular remodeling that will support wound healing. We found that both SDF and FTY720 recruit $Ly6C^{low}$ non-classical monocytes to the peri-implant region; however, the combination of these two factors increases the number of $CD206^{+}$ macrophages within the tissue suggesting a complex cellular response that can be achieved by combination of two signaling factors compared to either factor alone.

To overcome the challenge of co-delivering two physiochemically distinct molecules—a hydrophilic protein and hydrophobic small molecule—we engineered a dual affinity hydrogel that exploits the growth factor affinity of heparin and lipid chaperone

activity of albumin. In the present study, albumin-embedded Hep^{-N}-PEG-DA hydrogels released bioactive SDF-1α and FTY720 *in vitro* with approximately ~25% of the total SDF-1α payload and ~85% of the FTY720 payload released by day 7. SDF-1α, loaded by charge-based interaction with a heparin derivative[116] covalently linked in the hydrogel, was delivered primarily in a burst release within the first 24-36 hours. Heparin-based growth factor loading provides an advantage of protecting the stability of the growth factor cargo under various conditions that may otherwise lead to denaturation or degradation[114, 117]. To enable safe *in vivo* use of heparin and maintain its protective effect on growth factor cargo, we utilized a selectively -N desulfated heparin derivative (Hep^{-N}) with reduced anticoagulant activity[115, 117]. In previous studies, we have demonstrated that this amount of SDF-1α released from $aHep^{-N}$ hydrogels *in vivo* stimulates a localized recruitment of $Ly6C^{low}$ non-classical monocytes to the tissue surrounding the gel within 3 days[27].

To make the hydrogel bi-functional, albumin was encapsulated within the Hep^{-N} hydrogels as a lipid carrier for co-delivery with protein cargo and a novel means to display bioactive lipids in a biomaterial context[159]. Chaperone proteins facilitate stability and transport of lipids within blood and tissue compartments. Albumin is one of the main chaperone proteins that reversibly binds S1P in the blood and has also been found to bind FTY720[159]. Nearly 35% of S1P is found in albumin-rich fractions of blood and approximately 65% is found in complex with ApoM high-density lipoprotein[164]. FTY720, which is loaded by affinity for albumin entrapped in the bulk gel, released with a burst and continued sustained release over 7 days for total release of approximately 85% of the loaded drug *in vitro*. The differences in cumulative release between SDF-1α and

FTY720 are likely due to the distinct means of loading within the aHep^{-N} matrix. As we have observed previously with FTY720 released from PLGA polymer films, release of FTY720 alone from aHep^{-N} gels increased recruitment of non-classical monocytes to the peri-implant niche suggesting *in vivo* bioactivity. This highly localized recruitment is a desirable feature in managing local versus off-target effects. While these gels were designed as 2mm disk gels to create a localized response within the 12mm dorsal skinfold window chamber injury, the size, shape, and loading could be altered to achieve a broader tissue coverage area to scale the response. Further, future iterations of the material could include degradable elements to extend the opportunity for cell infiltration into the material.

Selective recruitment of Ly6C^{low} non-classical monocytes and CD206^{+} MerTK^{+}CD64^{+} "wound-resolving" macrophages are associated with enhanced tissue repair[2, 6, 27, 57, 156]. The extent to which macrophage heterogeneity arises from inherent plasticity versus microenvironmental polarization ("on-site education")[30], selective or sequential recruitment of monocyte subsets, or preferential survival of specific subtypes remains controversial due to the complex nature of the wound healing cascade in different injury contexts. Cells on the M2 end of the macrophage continuum are responsible for both stimulating the deposition of extracellular matrix and degrading/remodeling the matrix during wound healing; if left unchecked, these macrophages can contribute to pathologic fibrotic tissue[165]. A careful balance of the appropriate local cues must be struck to steer the inflammatory process towards healing and not chronic inflammatory fibrosis. Hydrogels were implanted in excisional skin wounds to evaluate synergy between S1PR3 and CXCR4 signaling axes with regard to pro-regenerative cell recruitment and microvascular remodeling. Dual release of SDF-1α and FTY720 synergistically increased

the recruitment of $CD11b^+$ myeloid leukocytes and $CXCR4^+$ cells to the implant-tissue interface relative to control or either factor alone supporting our hypothesis of functional synergy between these two pathways. Dual-loaded gels altered the early migratory behavior of monocytes that extravasated near the loaded implant, but not an unloaded control implant within the same window-chamber, indicating that release of these molecules affects the local behavior of monocytes in the tissue. Interestingly, within the peri-implant tissue, while both SDF-1α and FTY720 individually increased the proportion of $Ly6C^{low}$ non-classical monocytes in the tissue, with dual release, we observed a synergistic increase in macrophages ($MerTK^+CD64^+$), but not monocytes. Dendritic cells were excluded from our analysis based on the findings that skin dendritic cells do not express high levels of CD64[161]. The finding of increased macrophage accumulation was further supported by the presence of myeloid cells with an elongated morphology consistent with macrophage phenotype in the $CX3CR1^{GFP/+}$ mouse and also the presence of more $CD206^+$ cells in whole mount immunohistochemistry of the peri-implant tissue. CD206 is most highly expressed on M2a macrophages, but may also be expressed at lower levels on M2c cells[23]. Detection of synergy in the macrophage pool but not their recruited monocyte precursors may be explained by enhanced differentiation. These findings suggest that the combination of these two factors *in vivo* produces a more complex synergy than we have previously observed *in vitro* or that has been described in the literature. While priming monocytes with FTY720 increases their migration toward SDF-1α *in vitro* in an S1PR3 dependent manner[6], treating inflamed tissue with both SDF-1α and FTY720 causes an increase in cell recruitment and fate transition within the injury niche. We have previously shown that FTY720 released from PLGA thin films enhances

non-classical monocyte entrance into tissue from circulation as well as their differentiation into macrophages[6]. While the mechanism of this enhanced differentiation is incompletely understood, S1PR3 activation by FTY720 regulates reduced secretion of inflammatory cytokines from monocytes and increases in anti-inflammatory/pro-regenerative protein secretion from endothelial cells[6]. Thus, FTY720 may serve as a tissue conditioning cue that provides on-site education to encourage pro-regenerative differentiation of recruited monocytes into macrophages and their polarization toward wound-resolving phenotypes. The precise mechanistic details of this phenomenon will require further investigation.

Recruited leukocytes facilitate blood vessel remodeling during angiogenesis and arteriogenesis via strategic perivascular positioning, secretion of growth factors, and matrix-remodeling enzymes[43, 52, 55, 129, 166-168]. Expansion of the vascular network through formation of new vessels and increased caliber of existing vessels is crucial for supplying sufficient nutrients to promote tissue repair. Wound-resolving macrophages on the M2 end of the spectrum in particular are associated with enhanced vascular remodeling[26, 47, 52]. In the present study, dual release of SDF-1α and FTY720 synergistically enhanced arteriolar structural enlargement in conjunction with greater accumulation of wound-resolving macrophages. While we cannot definitively say there is a causal relationship between the macrophages and vascular remodeling in this study, based on prior literature, we believe there is a strong link between the macrophage recruitment and increased vascular diameter and network density. Thus, the dual affinity aHep^{-N}-PEG-DA platform has potential to increase tissue perfusion and improve therapeutic outcomes after ischemia, trauma, and tissue transplantation. It remains unclear whether this

phenomenon is the result of increased total myeloid recruitment, increased differentiation of M2-like macrophages, or alterations to the behavior of the recruited cells[6]. Taken together, these results indicate that cooperativity between the SDF-1α/CXCR4 and FTY720/S1PR3 signaling axes can be exploited to localize pro-regenerative macrophages to sites of injury and enhance microvascular network remodeling.

4.5. Materials and Methods

4.5.1. Heparin modification

N-desulfated heparin methacrylamide (Hep^{-N}-MAm) was fabricated as described previously[27]. Briefly, heparin sodium salt (Sigma) was dissolved in dH_2O at a concentration of 10 mg/mL and desalted using Dowex 50WX4 resin (mesh size 100-200, Sigma). Pyridine was added drop-wise to result in a pH of ~6, after which time excess pyridine was removed using a rotatory evaporator[114]. The solution was flash frozen and lyophilized to yield heparin pyridinium salt. Next, heparin pyridinium salt was dissolved in 90% DMSO/10% ddH_2O (v/v) at a concentration of 1 mg/mL, mixed for 2h at 50°C using a rotary evaporator, cooled and precipitated with 95% ethanol (VWR) saturated with sodium acetate (VWR). The precipitate was centrifuged, collected, and dissolved in dH_2O and this solution was dialyzed for 3 days followed by lyophilization to yield N-desulfated heparin. Finally, the product was functionalized with methacrylamide groups with an 8.0 molar excess of of N-(3-aminopropyl) methacrylamide hydrochloride (APMAm, Polysciences), N-hydroxysuccinimide (NHS, Acros Organics) and N-3-dimethylaminopropyl)-N'-ethylcarbodiimide hydrochloride (EDC, Sigma) at an acidic

pH. After functionalization, Hep^{-N}-MAm was dialyzed, lyophilized, and stored at -20°C until use. Proton nuclear magnetic resonance (^{1}H NMR) was performed to determine the degree of methacrylamide functionalization whereby Hep^{-N}-MAm was dissolved in deuterated water (10 mg/mL) and ^{1}H NMR spectra were recorded on a Bruker Avanace III 400 spectrometer at 400 MHz.

4.5.2. Hydrogel fabrication

As described previously, PEGDA and Hep^{-N}-MAm were UV sterilized, combined in a 9:1 PEGDA:Hep^{-N}-MAm ratio, and then added to a sterile phosphate buffered saline (PBS) solution comprised of GMP-quality bovine serum albumin (BSA, Sigma), ammonium persulfate (APS, 0.018M, Sigma), and N,N,N`,N`-tetramethylethylenediamine (TEMED, 0.018M, Sigma). Final concentrations of components in the hydrogel precursor solution were as follows: PEGDA, 10.0% w/v; Hep^{-N}-MAm, 1.1% w/v; BSA, 5.6% w/v; APS, 0.41% w/v; and TEMED, 0.21% w/v." The hydrogel precursor solution was pipetted between two sterile glass slides with an inner clearance of 0.5 mm, allowed to gel for 10 minutes at room temperature, and then punched with 2mm diameter biopsy punches (Miltex) to form gels of 0.5 mm thickness and 2 mm diameter.

4.5.3. SDF-1 α/FTY720 loading and release in vitro

Following fabrication, gels were placed in ultra-low binding 24-well plates and rinsed with PBS for 3h. For FTY720 only gels, a 10 μL droplet containing 2.38 x 10^{-8}

moles of either FTY720 (Cayman Chemical) or fluorescent 7-Nitrobenz-2-oxa-1,3-diazol-4-yl-FTY720 (Cayman Chemical) was added to the top of each gel and the gels were incubated overnight at 4˚C. After loading, gels were rinsed for 3h at room temperature with 500 μL PBS. For SDF-1α only gels, PBS was removed and a 10 μL droplet of SDF-1α (0.1 μg; PeproTech) was added to each gel followed by incubation overnight at 4˚C. For dual-loaded gels, FTY720 was loaded overnight first, followed by SDF-1α. (For parity in sample treatment, in gels with either FTY720 or SDF-1α only, the samples would undergo both overnight incubations, but with a 10 μL droplet of PBS in place of the drug that was not being loaded.)

After loading, the wells were filled with 500μL of PBS and incubated at 37°C for the release study. At each timepoint, PBS was exchanged and stored at -80ºC for subsequent analysis. The concentration of SDF-1α in supernatant was quantified using a Mouse CXCL12/SDF-1α Quantikine ELISA Kit (R&D Systems) and the concentration of 7-Nitrobenz-2-oxa-1,3-diazol-4-yl-FTY720 was quantified using a fluorescence plate reader with λex = 485nm and λem = 515nm. Two batches of Hep^{-N}-MAm were required to complete all studies, and therefore FTY720 and SDF-1α release from hydrogels made with both Hep^{-N}-MAm batches were averaged to obtain final release curves (n = 6 hydrogels per group across 2 batches of Hep^{-N}-MAm).

4.5.4. In vitro migration

Bioactivity of released SDF-1α/FTY720 was assayed *in vitro* as described previously. Briefly, albumin-embedded gels loaded with FTY720 and SDF-1α (aHep^{-N}-FTY+SDF), SDF-1α alone (aHep^{-N}-SDF), or neither factor (aHep^{-N}) were incubated with

650µL of Iscove's Modified Dulbecco's Medium (Fisher) containing 0.5% fatty acid-free bovine serum albumin (Fisher) for 24h at 37°C. A transwell assay was assembled by transferring hydrogel-conditioned media to the chamber below a 5µm pore size membrane, and seeding $4x10^5$ cells from C57BL/6 mouse bone marrow aspirate on top. After 4h of migration at 37°C and 5% CO2, migrated cells were stained with DRAQ5 dye according to manufacturer's protocol (Cell Signaling Technologies). Relative migration was quantified by fluorescence intensity using an Odyssey CLx Infrared Imaging System (LI-COR Biosciences). Statistical analysis was performed using one-way ANOVA, Geisser-Greenhouse correction for non-sphericity, and Tukey post-hoc multiple comparisons test (n=5).

4.5.5. Dorsal skinfold window chamber and hydrogel implantation

Male C57BL/6 mice aged 8-12 weeks of age were anesthetized by i.p. injection of a mixture of ketamine (100mg/kg) and xylazine (10mg/kg) in sterile 0.9% saline or by inhaled isoflurane and surgically fitted with sterile dorsal skinfold window chambers (APJ Trading Co.) as previously described[6, 53, 151, 152]. Prior to surgery, dorsal skin was shaved, depilated, and sterilized via triplet washes of 70% ethanol and chlorhexidine. A double-layered skin fold was elevated off the back of the mouse and the back side of the titanium window chamber frame was surgically fixed to the underside of the skinfold. Surgical microscissors were used to remove the epidermis and dermis from the top-side of the skinfold in a circular area (diameter = 12mm) to reveal the vasculature underlying the reticular dermis. Exposed tissue was kept hydrated with sterile saline. The front side of the titanium frame was then mounted on the top of the skin and attached to its underlying

counterpart. The dorsal skin was sutured to the titanium frame, and mice were implanted with one Hep^{-N} internal control hydrogel and one $aHep^{-N}$ experimental hydrogel (unloaded or loaded albumin-containing gel with SDF-1α, FTY720, or both factors) placed on opposite sides of the window. The exposed tissue was then overlaid with a protective sterile glass coverslip. Mice were allowed to recover in heated cages and administered sustained release buprenorphine via i.p. injection as a postoperative analgesic. All mice received a standard laboratory diet and water *ad libitum* throughout the course of the experiment.

4.5.6. Flow cytometry and identification of immunophenotypes

To measure the recruitment of cells to tissue surrounding the hydrogels, the dorsal tissue circumscribing the gel position was collected and digested with 1mg/mL collagenase IA (Sigma) in Krebs-Ringers solution at 37°C, and further disaggregated with a cell strainer and pestle to create a single cell suspension. To examine cells at the hydrogel interface, cells were removed from the hydrogel surface by incubation with trypsin for 10min at 37°C and combined with a fixed volume of flow cytometry counting beads for quantification (CountBright Absolute Counting Beads, Life Technologies). Immuno-staining and flow cytometry analyses were performed according to standard procedures and analyzed on a FACS-AriaIIIu flow cytometer (BD Biosciences). The following antibodies were used for cell phenotyping: APC/Cy7- or BV510-conjugated anti-CD11b (BioLegend, M1/70), APC- or BV421-conjugated anti-Ly-6C (BioLegend, HK1.4), PE- or PerCP/Cy5.5-conjugated anti-CXCR4 (eBiosciences, 2B11), PE-conjugated anti-MerTK (R&D Systems, 108928), BV711-conjugated anti-CD64 (BioLegend, X54-5/7.1), and BV605-conjugated anti-CD206 (BioLegend, C068C2). Monocyte populations were defined as

$CD11b^{+}SSC^{low}Ly\text{-}6C^{high/low}$ and were confirmed to be $Ly\text{-}6G^{-}$ (BioLegend, 1A8). Macrophages were identified with high fidelity as $MerTK^{+}CD64^{+}$ cells[160] which excludes dendritic cells[161]. Further confirming macrophage identity of the $MerTK^{+}CD64^{+}$ cells, nearly all cells identified as macrophages expressed F4/80 (data not shown). Statistical analysis in **Figure 20** and **Figure 22** was conducted using one-way ANOVA, Geisser-Greenhouse correction for non-sphericity, and Tukey post-hoc multiple comparisons test. The number of replicates in are as follows: **Figure 20**, n=5-6; **Figure 22a**, n=7-9; **Figure 22b,c**, n=2-4.

4.5.7. Confocal intra-vital microscopy of $CX3CR1^{+}$ macrophages

Male heterozygous B6.129P-Cx3cr1tm1Litt/J (CX3CR1-EGFP) mice were utilized to visualize monocytes and macrophages in live mice based on their selective surface expression of CX3CR1[6, 27, 34]. Confocal intra-vital microscopy was performed on day 1 or day 6 after surgery and gel implantation. To label perfused vasculature, mice were anesthetized with isoflurane gas and given a retro-orbital injection of high molecular weight TRITC-conjugated dextran (2 MDa; Life Technologies). For subsequent microscopy, the mouse was secured to the microscope stage in a custom adapter, the glass window was removed, and dorsal tissue was irrigated with sterile saline. Z-stack images were acquired immediately proximal to the gel using a 20X water immersion objective (NA=1.0) on a Zeiss LSM710 NLO microscope. For 3D analysis in Imaris (Bitplane), time-lapse images (period=30s, duration=15min) were acquired to visualize immune cell migration in the close surrounding tissue. Cells expressing CX3CR1-GFP were identified in Imaris using the surface tool. CX3CR1+ surfaces were identified by smoothing with a

2μm grain size and an automatic threshold on absolute intensity. Touching objects were split using a seed points diameter of 10μm. Vessels were identified in Imaris by drawing a surface on the TRITC-dextran fluorescent channel with a 3μm grain size, manually-selected threshold value (determined based on each image), and manually-selected volume filter to remove small debris. The automatic cell tracking feature was selected, and the following metrics were exported for statistical analysis: track displacement, track length, and track straightness. For statistical analysis of cell migration metrics in figure 3, Mann-Whitney rank test was performed on the distribution comprised of all cells analyzed across 2 mice per group and 2 ROI per mouse (FTY720+SDF-1, n=3095; internal control, n=2119).

4.5.8. Whole-mount IHC and confocal microscopy of recruited macrophages

On day 7 after surgery and gel implantation, mouse vasculature was perfused with warm 0.9% saline and then 4% PFA until tissues were fixed. Dorsal tissue was explanted and drop-fixed in 4% PFA for 10min, permeabilized with 0.2% saponin in PBS for 16-24h at 4°C, blocked with 10% mouse serum in PBS for 16-24h, and stained with combinations of the following monoclonal antibodies diluted into a solution of 0.5% BSA, 5% mouse serum, and 0.1% saponin in PBS: Cy3-conjugated anti-α-smooth muscle actin (αSMA, 1:300, Sigma), AF594-conjugated anti-CD31 (1:100, BioLegend), AF647-conjugated anti-CD68 (1:200, AbD Serotec), and AF488-conjugated anti-CD206 (1:200, AbD Serotec). Images of macrophage accumulation in dorsal tissue were acquired as 3-dimensional z-stacks in confocal mode using a Zeiss LSM710 NLO microscope at 20X magnification. To quantify the number of CD68+CD206+ macrophages per unit area, Imaris (Bitplane)

software was used. Surfaces were created in the CD68 and CD206 channels independently, and the number of CD68+ surfaces overlapped by CD206+ surfaces were counted. In Figure 25, cell density is reported for n=2-11 regions of interest per group across 2-3 animals per group.

4.5.9. Brightfield intra-vital microscopy and analysis of arteriolar diameter

Immediately following surgery and on day 3, mice were maintained under isoflurane anesthesia, the glass window was removed, and dorsal tissue was flooded with 1mM adenosine in Ringer's solution to maximally dilate all vessels and maintain tissue hydration. The mouse was then mounted to a custom microscope stage mount and a tile scan of the entire window was acquired noninvasively at 5X magnification on a Zeiss Imager.D2 microscope with AxioCam MRc 5 color digital camera (Carl Zeiss). To measure changes in the diameter of arterioles, arteriole–venule pairs were identified within a 3mm radius of the center of each gel. Arterioles and venules were identified on the basis of size and morphology at day 0. Internal diameters based on blood column width in brightfield images were measured using Zen Blue (Zeiss) and recorded longitudinally for each vessel segment on day 0 and 3. Quantification of arteriolar diameter was restricted to the microvasculature by analyzing arterioles with diameters <40μm on day 0[27, 129]. Analysis was limited to arterioles visible at both time points (1-7 arterioles/gel).

4.5.10. Statistical analysis

Data are presented as mean ± standard error of the mean (SEM). All statistical analysis was executed in GraphPad Prism software. Statistical tests are reported in the methods and legends associated with each figure. Unless otherwise noted, $p<0.05$ was considered statistically significant.

5. RELATIONSHIP BETWEEN IMMUNE CELL INFILTRATION AND ROTATOR CUFF MUSCLE DEGENERATION[3]

5.1. Introduction

Full-thickness rotator cuff tears (RCTs) are present in more than 20% of the population[169]. RCTs increase in frequency and severity with age and cause significant pain and functional deficiency[170-174]. RCT causes degeneration of the associated muscles, a process which includes muscle retraction and atrophy, fatty infiltration, and fibrosis. Muscle degeneration is a strong predictor of patient morbidities such as pain, functional deficiency, and post-surgical tear recurrence, and is not reversed by tendon repair[175, 176]. Thus, prevention or reversal of muscle degeneration due to RCT is a major unmet clinical need. Identification of molecular and cellular targets for therapeutic intervention requires elucidating the underlying pathobiology of RC muscle degeneration.

Evidence from RCT and chronic muscle pathologies suggests that inflammation, particularly mononuclear phagocyte (MP) infiltration, contributes to muscle degeneration. Pro-inflammatory cytokines such as TNFα and IL-6 stimulate apoptosis of myocytes and catabolism of intramyocellular proteins[64, 65], thus causing muscle atrophy in cancer cachexia and autoimmune disorders. Classical "pro-inflammatory" subpopulations of mononuclear phagocytes secrete more pro-inflammatory cytokines compared to non-

[3] Adapted from: J.R. Krieger, L.E. Tellier, M.T. Ollukaren, J.S. Temenoff, E.A. Botchwey, Quantitative Analysis of Immune Cell Subset Infiltration of Supraspinatus Muscle After Severe Rotator Cuff Injury, Regenerative Engineering and Translational Medicine (2017) 1-12. Reprinted with permission from Springer Nature.

classical alternatively-activated subpopulations[8, 11, 22-24], suggesting that intramuscular infiltration of classical subtypes may promote chronic muscle degeneration. Indeed, in the *mdx* mouse model of Duchenne muscular dystrophy, chronic muscle degeneration is in part caused by the classical pro-inflammatory Ly6C^{hi} subset of circulating monocytes (MO)[66]. Human and rodent muscles undergoing fatty degeneration after RCT show dramatic co-localization of fat-rich regions with macrophages (MΦ) that contain intracellular lipid droplets[67, 68]. Rotator cuff muscle degeneration is exacerbated by administration of lysophosphatidic acid, whereby MΦ accumulation and TNFα expression are increased[69]. Taken together, these studies suggest that pro-inflammatory mononuclear phagocytes promote chronic muscle degeneration.

Because MP are comprised of highly heterogeneous subpopulations that exert divergent effects on injured tissue during pathogenesis and regeneration, understanding RC muscle inflammation at the subpopulation level is critical for identifying therapeutic targets. The spectrum of MΦ phenotypes is commonly simplified into two primary categories: classically-activated "M1" and non-classical or alternatively-activated "M2", of which multiple subtypes have been described[11]. Accumulation of MΦ within injured adult skeletal muscle is primarily driven by recruitment of circulating MO rather than expansion of tissue-resident MΦ[1]. MO circulate as functionally distinct subsets in both mouse and human blood. Classical MO are characterized by Ly6C^{hi}CX3CR1^{lo} expression in mice (CD14^{hi}CD16^{-} in human), whereas non-classical MO are Ly6C^{lo}CX3CR1^{hi} in mice (CD14^{+}CD16^{+} in human)[34]. Ly6C^{hi} classical MO predominate the acute phases of injury, secrete inflammatory cytokines such as IL-6, iNOS, and TNFα[29], and produce high

levels of matrix metalloproteinases and cathepsins[8], whereas Ly6C^{lo} MO predominate in later phase inflammation, promote angiogenesis and matrix deposition, and secrete higher levels of VEGF, TGFβ, and IL-10 and lower levels of TNFα and IL-1β[1, 8, 30]. MO recruitment is required for natural repair; multiple studies show that depletion of circulating MO causes incomplete and fibrotic healing of skeletal muscle after toxin-induced injury[1, 59, 60]. In early stages after acute muscle injury, infiltrating Ly6C^{hi} MO ingest debris and induce proliferation of myosatellite mononuclear progenitor (satellite) cells[1]. In later stages, Ly6C^{lo} MO and M2 MΦ subsets promote satellite cell myogenic differentiation and fusion to expand myotubes, and secrete insulin-like growth factor-1 (IGF-1) required for muscle regeneration[63].

Given that different subpopulations of MP exert distinct effects on skeletal muscle, the present study seeks to investigate the phenotypic distribution and causal role of inflammatory cells in supraspinatus (SS) degeneration after severe RCT in a mouse model. As in Aims 1 and 2, biomaterial-mediated local delivery of SDF-1 or FTY720 is evaluated for its ability to modulate inflammation and protect against degeneration.

5.2. Results

5.2.1. Mononuclear phagocyte recruitment to supraspinatus muscle after severe rotator cuff injury

To quantify subpopulations of inflammatory cells within the SS muscle after massive RC injury, SS muscles were harvested 7 days after injury and analyzed by flow

cytometry. MP were identified according to the following surface marker expression: MΦ = $MerTK^+$ $CD64^+$; dendritic cell (DC) = NOT($MerTK^+$ $CD64^+$) $CD11c^+$; MO = NOT($MerTK^+$ $CD64^+$) $CD11c^-$ $CD11b^+$ SSC^{lo} (**Figure 26a**)[177]. MP count is $3.9x10^4$ cells/g in the tenotomy (TT) group and $8.7x10^4$ cells/g in the tenotomy plus denervation (TT+DN) group, which represent 3.2-fold and 3.9-fold increases from respective uninjured contralateral muscles (**Figure 26b**). MP count is 2.2-fold greater in TT+DN than TT (**Figure 26b**). MΦ count is $3.0x10^4$ cells/g in the TT+DN group, increasing 6.3-fold compared to contralateral (**Figure 26c**). MO count is $1.0x10^4$ in TT and $2.3x10^4$ in TT+DN, representing 2.4-fold and 2.6-fold increases compared to contralateral controls (**Figure 26d**). MO count is 2.3-fold greater in TT+DN than TT (**Figure 26d**). DC count in the TT+DN group is 3.9-fold higher than contralateral and 2.1-fold higher than TT (**Figure 26e**). The frequency of DC, MΦ, and MO populations is 1.7%, 1.2%, and 1.1% in TT, respectively, compared to 2.5%, 2.1%, and 1.6% in TT+DN (**Figure 26f**). Overall, results indicate that injury causes dramatic accumulation of MO, MΦ, and DC.

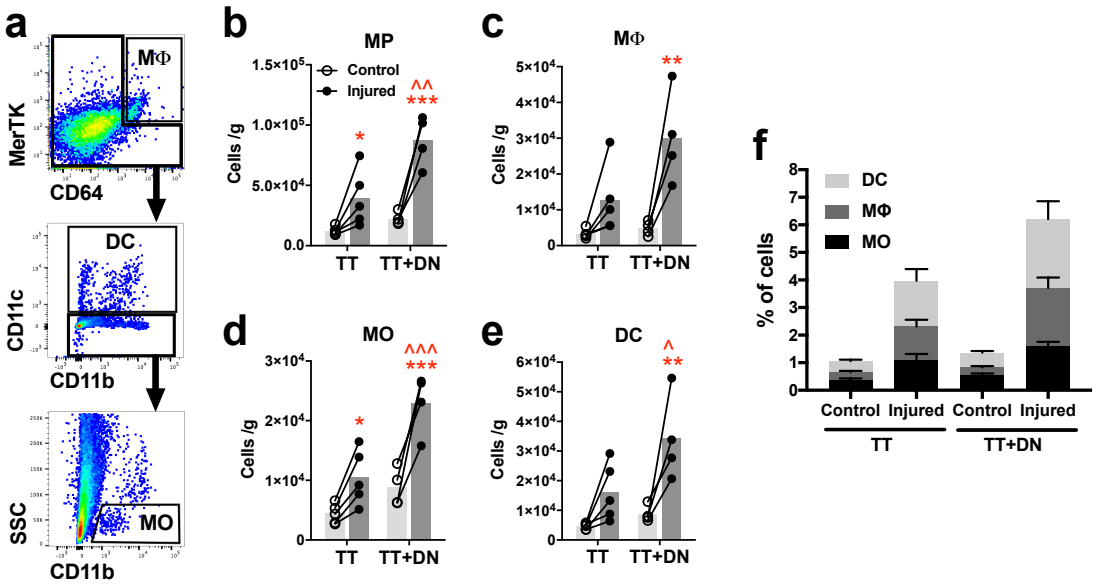

Figure 26. Mononuclear phagocyte accumulation in supraspinatus muscle 7 days after rotator cuff injury. (A) Flow cytometry gating scheme to identify populations of mononuclear phagocytes after pre-gating for single cells. Mononuclear phagocyte count (B) is calculated as the sum of macrophages (C), monocytes (D), and dendritic cells (E) normalized to muscle mass. (F) Frequency of each mononuclear phagocyte population out of total cells. Closed circles represent the injured side; open circles, uninjured contralateral side. Statistical comparisons are conducted by repeated measures two-way ANOVA followed by Sidak multiple comparisons test (TT, n=5; TT+DN, n=4). *P<0.05, **P<0.01, ***P<0.001 comparing injury side to contralateral side. ^P<0.05, ^^P<0.01, ^^^P<0.001 comparing TT+DN to TT.

5.2.2. Non-classical subpopulations predominate mononuclear phagocyte infiltration

M1-like and M2-like subpopulations of MΦ were identified by surface expression of CCR7 and CD206, respectively (**Figure 27a**), as per Spiller *et al.[23]*. TT increases the frequency of $CD206^+$ cells within the MΦ pool from 29.3% to 59.9%; TT+DN, from 39.8% to 74.7% (**Figure 27b**). $CD206^+$ frequency is higher in TT+DN compared to TT (**Figure 27b**). Conversely, TT decreases the frequency of $CCR7^+$ cells within the MΦ pool from

77.7% to 59.6%; TT+DN, from 82.7% to 64.2% (**Figure 27c**). Thus, SS muscle is biased toward M1-like MΦ without injury, and toward M2-like MΦ after TT and TT+DN. The TT+DN group has the highest counts of both $CD206^+$ MΦ and $CCR7^+$ MΦ compared to TT and contralateral (**Figure 27d**). Increased $CCR7^+$ MΦ count despite decreased $CCR7^+$ MΦ frequency in the MΦ pool is explained by the larger overall pool of MΦ in the TT+DN group.

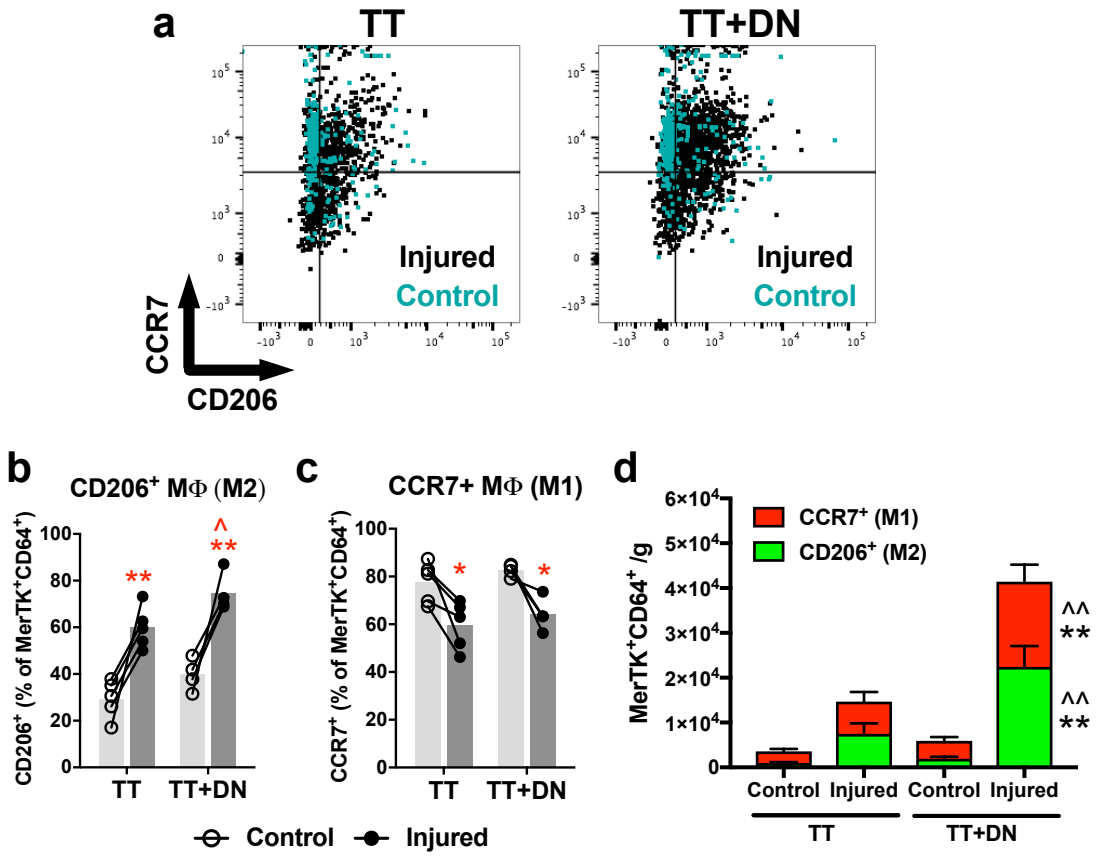

Figure 27. Macrophage subpopulations. (A) Flow cytometry gating scheme to identify CD206+ and CCR7+ macrophages. The fractions of CD206+ (B) and CCR7+ (C) cells within the macrophage pool are affected by rotator cuff injury. TT+DN injury increases the number of CD206+ and CCR7+ macrophages per gram of muscle (D). Closed circles represent the injured side; open circles, uninjured contralateral side. Statistical comparisons are conducted by repeated measures two-way ANOVA followed by Sidak multiple comparisons test (TT, n=5; TT+DN, n=4). *P<0.05, **P<0.01 comparing injured side to contralateral side. ^P<0.05, ^^P<0.01 comparing TT+DN to TT.

MO subpopulations are discriminated by surface expression of Ly6C (**Figure 28a**)[8, 34]. TT+DN significantly increases the frequency of non-classical Ly6C^{lo} (**Figure 28b**) and decreases the frequency of classical Ly6C^{hi} (**Figure 28c**) cells within the MO pool compared to contralateral, whereas TT has no significant effect on Ly6C^{lo}/Ly6C^{hi} frequency. Consequently, TT+DN increases the absolute count of both Ly6C^{lo} and Ly6C^{hi} compared to TT and contralateral (**Figure 28d**). TT increases Ly6C^{lo} count compared to contralateral, owing increased overall MO count (**Figure 28d**).

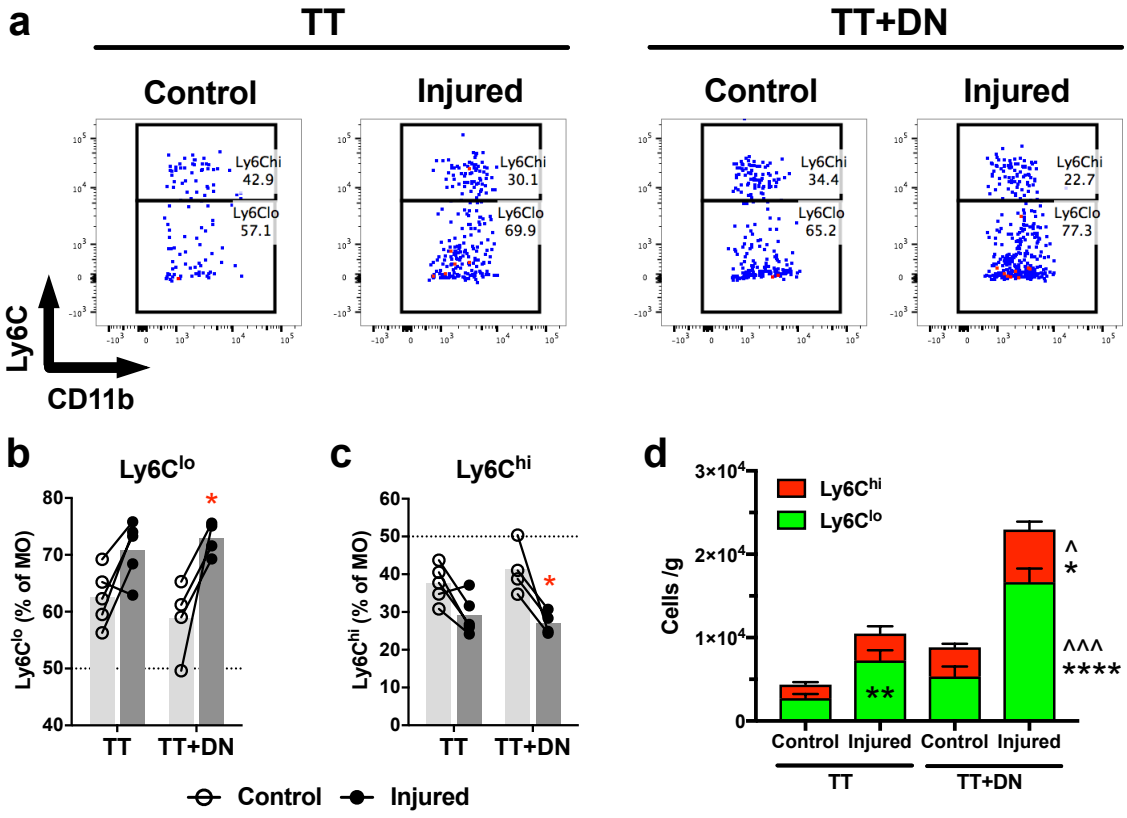

Figure 28. Monocyte subpopulations. (A) Flow cytometry gating scheme to identify Ly6C^{lo} and Ly6C^{hi} subpopulations of monocytes. The fraction of Ly6C^{lo} (B) and Ly6C^{hi} (C) cells within the monocyte pool are increased and decreased, respectively, by TT+DN injury. The numbers of Ly6C^{lo} and Ly6C^{hi} monocytes per gram of muscle are increased by injury (D). Closed circles represent the injured side; open circles, uninjured contralateral side. Statistical comparisons are conducted by repeated measures two-way ANOVA followed by Sidak multiple comparisons test (TT, n=5; TT+DN, n=4). *P<0.05, **P<0.01,

***P<0.001, ****P<0.0001 comparing injury side to contralateral side. ^P<0.05, ^^P<0.01, ^^^P<0.001 comparing TT+DN to TT.

5.2.3. Neutrophil and T lymphocyte recruitment

Neutrophil and T lymphocyte infiltration is also quantified (**Figure 29**). Neutrophils ($Ly6G^+$) are present in low abundance (6000 cells/g) relative to other inflammatory cell types measured. Neither injury affects neutrophil count (**Figure 29b**) but TT increases the frequency of neutrophils out of total cells compared to TT+DN (**Figure 29c**). T lymphocyte count is unaffected by either injury (**Figure 29d**), but the frequency of T lymphocytes decreases due to TT (**Figure 29e**). Helper T lymphocyte (T_H; $CD4^+CD3^+$) and regulatory T lymphocyte (T_{reg}; $CD25^+CD4^+CD3^+$) counts and frequency out of total cells do not change due to injury (**Figure 29f,g,i,j**). Injury enriches the T lymphocyte pool in T_H cells, as evidenced by TT increasing the T_H frequency within the T lymphocyte pool from 2.8% to 7.5% and TT+DN increasing the frequency from 3.2% to 4.9% relative to controls (**Figure 29h**). The T_H frequency within the T lymphocyte pool is higher in TT compared to TT+DN (**Figure 29h**). Neither injury enriches the T_H pool in T_{reg} cells (**Figure 29i**). The T_{reg} frequency within the T lymphocyte pool is higher in TT (3.1%) compared to TT+DN and contralateral (**Figure 29k***)*, due to the larger frequency of T_H.

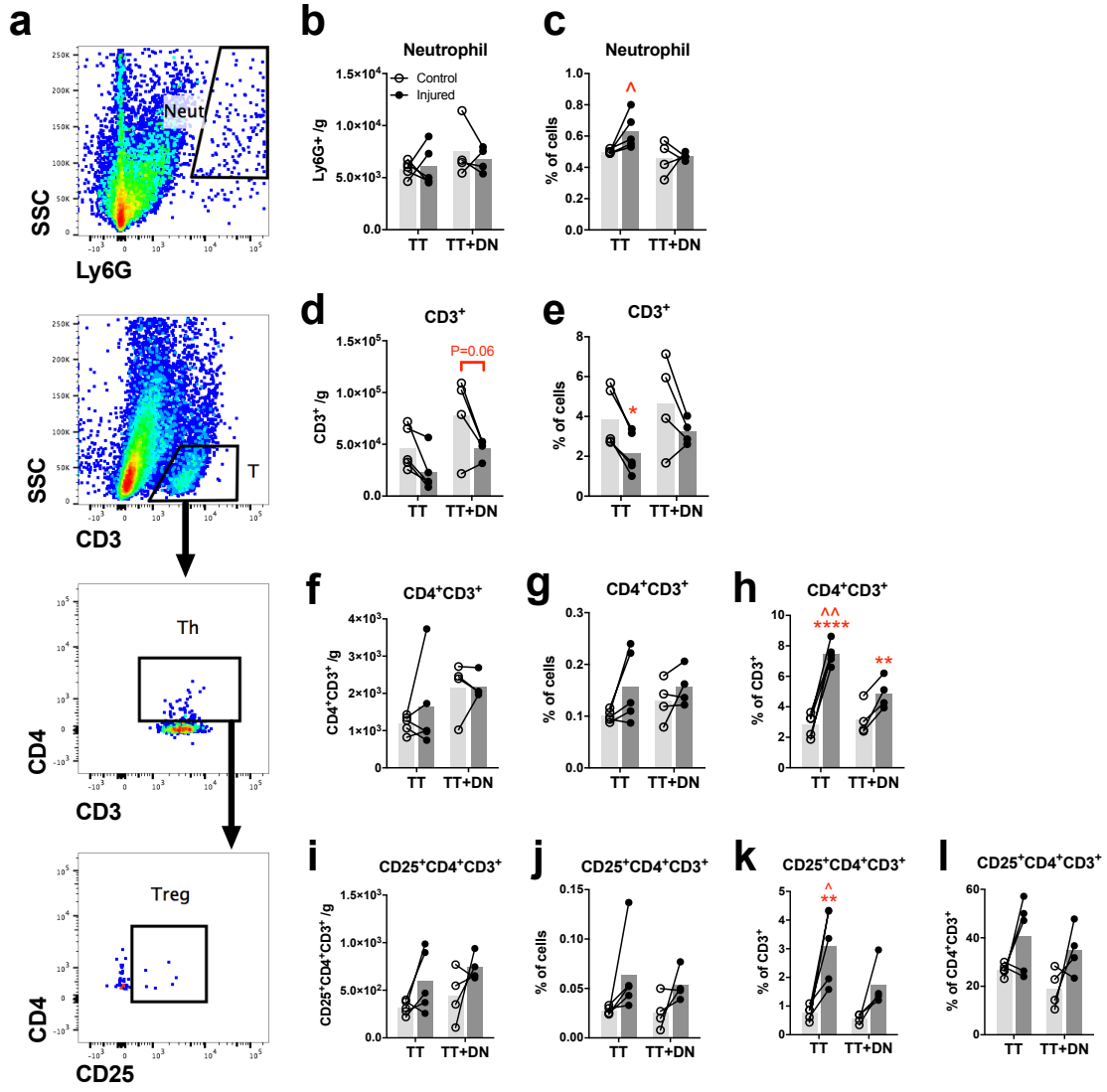

Figure 29. Quantification of neutrophil and T lymphocyte populations. (A) Flow cytometry gating scheme to identify neutrophils (Ly6G+), T lymphocytes (CD3+), T_H (CD4+CD3+), and T_{reg} (CD25+CD4+CD3+). Cell count per gram of muscle of neutrophils (B), T lymphocytes (D), T_H (F), and T_{reg} (I) is not significantly affected by injury. TT increases neutrophil frequency out of total cells compared to TT+DN (C). TT decreases T lymphocyte frequency out of total cells compared to uninjured contralateral (E). Neither injury affects T_H (G) or T_{reg} (J) frequency out of total cells. The fractions of T_H (H) and T_{reg} (K) within the T lymphocyte pool are increased by injury. The fraction of T_{reg} within the T_H pool is unaffected by injury (L). Statistical comparisons are conducted by repeated measures two-way ANOVA followed by Sidak multiple comparisons test (TT, n=5; TT+DN, n=4). *P<0.05, **P<0.01, ***P<0.001, ****P<0.0001 comparing injured side to contralateral side. ^P<0.05, ^^P<0.01, ^^^P<0.001 comparing TT+DN to TT.

5.2.4. Multivariate analysis of immune cell infiltration

To describe the inflammatory profile in a reduced-dimensionality model, unsupervised principal component (PC) analysis was performed on a set of 11 flow cytometric measurements. Injured versus contralateral muscles are discriminated along PC1, and TT versus TT+DN muscles are discriminated along PC2 (**Figure 30b**). The x-axes of the loadings (**Figure 30a**) and scores (**Figure 30b**) plots show that injury is described by increased MO, MΦ, DC, Ly6C^{lo} MO, CD206^{+} MΦ, T_H, and T_{reg}, and decreased CCR7^{+} MΦ, T lymphocytes, and wet muscle mass. The y-axes of the loadings and scores plots show that TT+DN is discriminated from TT by increased MO, MΦ, DC, CD206^{+} MΦ, and T lymphocytes, and decreased T_H, T_{reg}, and neutrophils.

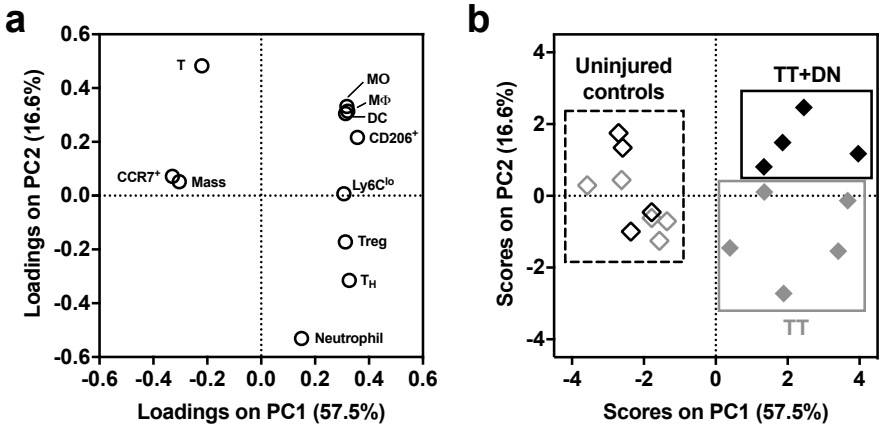

Figure 30. Unsupervised principal component analysis of flow cytometry quantification. (A) Loadings (weight coefficients) plot of the 11 input variables in the reduced principal component space. Input variables are: muscle mass, MΦ (% of cells), MO (% of cells), DC (% of cells), T lymphocyte (% of cells), neutrophil (% of cells), CD206^{+} (% of MΦ), CCR7^{+} (% of MΦ), Ly6C^{lo} (% of MO), T_H (CD4^{+}CD3^{+} % of CD3^{+}), and T_{reg} (CD25^{+}CD4^{+}CD3^{+} % of CD4^{+}CD3^{+}). (B) Injury conditions are separated by the model in the scores plot (TT, n=5; TT+DN, n=4). Quality-of-fit metrics are provided in Methods.

Pro-regenerative cytokines are secreted after injury

To assess whether predominance of non-classical subpopulations is associated with a pro-regenerative cytokine and growth factor milieu, 22-plex quantitative immunoassay was performed on SS muscle lysate at day 7. TT+DN injury significantly affected the production of 6 of the 22 proteins analyzed, increasing the production of IL-10, IL-33, SDF-1α, IGF-1, FGF-basic, and Dkk-1 compared to uninjured contralateral controls (**Figure 31**).

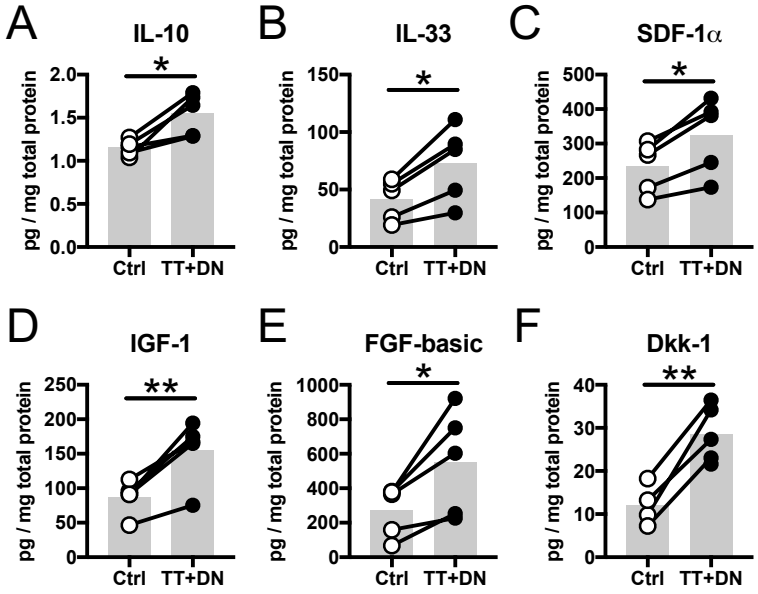

Figure 31. Cytokine and growth factor production in supraspinatus after RCT. Cytokines and growth factors involved in immune cell polarization and muscle degeneration and regeneration were quantified via Luminex 22-plex immunoassay. TT+DN injury increases production of IL-10 (A), IL-33 (B), SDF-1α (C), IGF-1 (D), FGF-basic (E), and Dkk-1 (F) compared to uninjured contralateral control (n=5, *P<0.05, **P<0.01, paired t-test).

5.2.5. Depletion of circulating monocytes protects supraspinatus against atrophy

Intravenous administration of liposomal clodronate is an experimental tool used to deplete circulating MO[178, 179]. Liposomal clodronate causes complete depletion of blood MO within 6 h followed by recovery of the $Ly6C^{hi}$ and $Ly6C^{lo}$ populations at 2 and 7 days, respectively[178]. The present study investigates the contribution of circulating MO to SS atrophy by administering liposomal clodronate (clod-lip) or saline control every 2-3 days upon combined tenotomy and denervation injury (**Figure 32a**). Clod-lip decreases wet muscle mass compared to uninjured contralateral control at 21 days (mean: 29.0 vs. 41.8 mg), whereas saline control has no effect (mean: 38.5 vs. 41.5 mg) (**Figure 32b**). Clod-lip causes greater percent decrease in wet mass between injured and uninjured contralateral muscles compared to saline control (**Figure 32c**). Quantification of myofiber cross-sectional area (CSA) is a complementary approach to assess muscle atrophy and is accomplished using immunohistochemistry (IHC) to visualize collagen IV in the myofiber basement membrane (**Figure 32d**). Saline control shows no difference in myofiber CSA between injured and uninjured contralateral muscles (median: 607 vs. 655 μm^2) (**Figure 32e**). Lack of atrophy at 21 days in the saline control group is consistent with literature indicating that mouse SS degeneration is detected at 6-12 weeks[69, 180-182]. Notably, clod-lip causes decreased CSA compared to both uninjured contralateral (median: 507 vs. 641 μm^2) (**Figure 32f**) and saline controls (**Figure 32g**). Taken together, these results indicate that depletion of circulating MO via liposomal clodronate accelerates SS atrophy after severe RC injury.

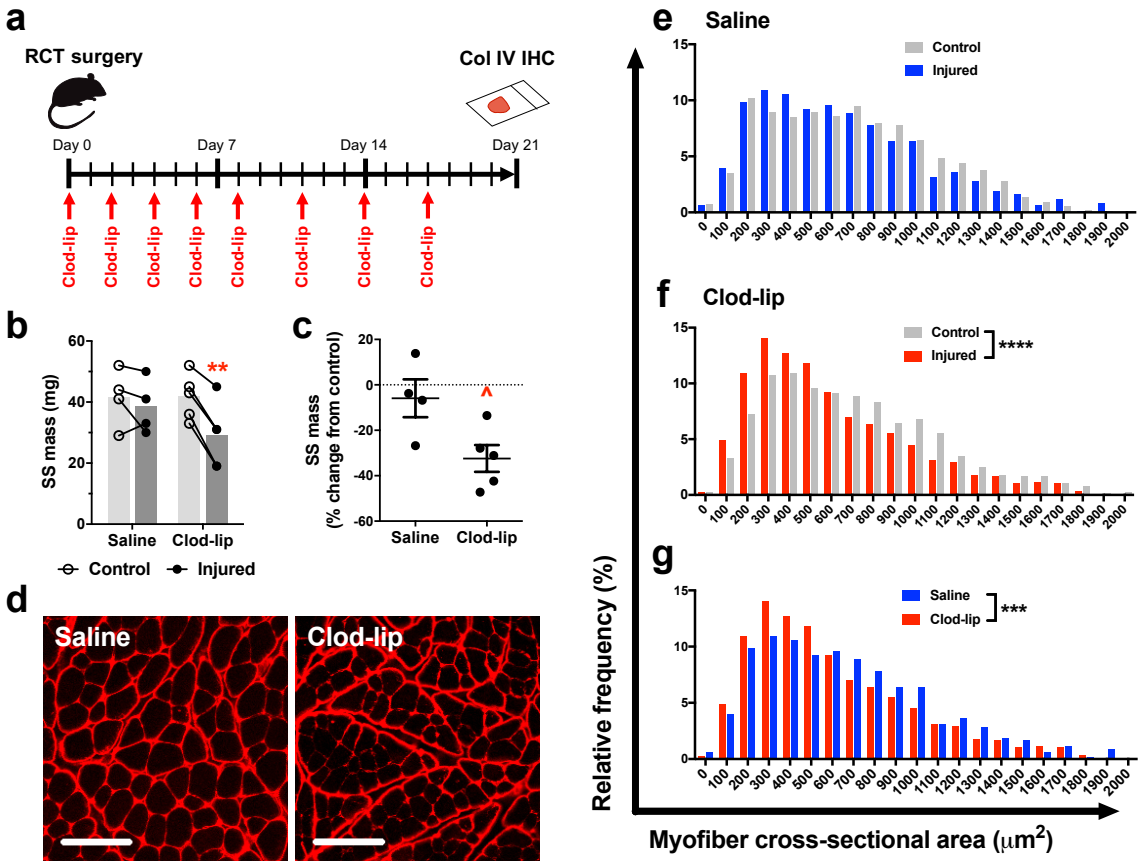

Figure 32. Liposomal clodronate accelerates muscle atrophy. Liposomal clodronate is delivered intravenously at 2-3 day intervals following TT+DN injury (A). To assess muscle atrophy, supraspinatus mass (B) and percent change in mass between injured and uninjured contralateral supraspinatus (C) are measured at day 21 (Saline, *n*=4; Clod-lip, *n*=5). Myofiber cross-sectional area is visualized by anti-collagen IV IHC (D) and quantified using ImageJ (E-G) (n=964 across 4 animals per group). Statistical comparisons are conducted by two-way ANOVA with Sidak post-hoc test (B), t-test (C), and Mann-Whitney rank test (E-G). ^*P*<0.05, **P*<0.05, ****P*<0.001, *****P*<0.0001. Scale bar: 100 μm.

5.2.6. Local delivery of SDF-1 via Hep^{-N} microparticles increases recruitment of dual polarized MΦ

To investigate MP infiltration in response to local delivery of SDF-1, we employed a DTT-crosslinked, hydrolytically degradable microparticle formulation of the aHep^{-N}

hydrogel platform, enabling injection into the SS. Microparticles released human SDF-1 by approximately 24 h *in vitro* (**Figure 33a,b**). Microparticles were injected into the supraspinatus during surgery and immune cell infiltration was assessed at day 7 by flow cytometry. Human SDF-1 decreased the proportion of $CD206^{+}CCR7^{+}$ "dual polarized" MΦ within the MΦ pool compared to FTY720, unloaded MP, and untreated control (**Figure 33a,b**).

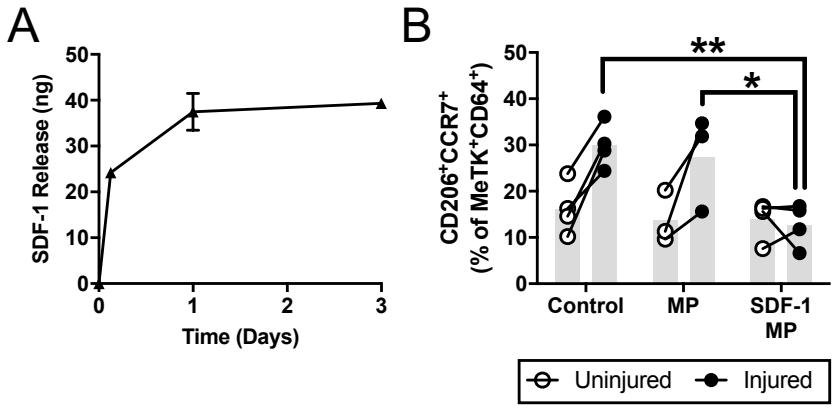

Figure 33. SDF-1-releasing aHep^{-N} microparticle delivery to the supraspinatus. (A) Release kinetics of human SDF-1 from microparticles. (B) SDF-1-loaded microparticle delivery at the time of surgery decreases the proportion of CD206+CCR7+ "dual polarized" macrophages at day 7 as measured by flow cytometry. **P*<0.05, ***P*<0.001 by two-way ANOVA and post-hoc multiple comparisons test (*n*=3-4).

5.2.7. Local, sustained delivery of FTY720 via PLGA microparticles

Although SDF-1-releasing Hep^{-N} microparticles exhibited immunomodulatory activity by decreasing the frequency of dual polarized MΦ, it is unclear whether this initial outcome is desirable toward the goal of inhibiting degeneration and/or enhancing regeneration of SS muscle. Because FTY720 affects both the recruitment and cytokine

elaboration of MO[6], and because sustained release of FTY720 over several weeks can be achieved using PLGA microparticle carriers[183], we next attempted therapeutic immunomodulation using local delivery of FTY720-loaded PLGA microparticles. To achieve sustained local delivery of FTY720 during the progression of immune cell infiltration, 50:50 PLGA microparticles encapsulating FTY720 (total dose = 10 μg, drug:polymer ratio = 1:150) were injected into SS muscle at the time of surgery. PLGA microparticles release FTY720 *in vitro* with an initial burst followed by relatively linear release (**Figure 34b**). Microparticle-mediated delivery of 10 μg FTY720 does not affect MP count, T lymphocyte count, or T_H/T_{reg} count at day 7; however, the frequency of T_{reg} cells in the T_H and T lymphocyte populations is decreased in the FTY720 microparticle group compared to unloaded PLGA microparticles and vehicle control (**Figure 34c,d**).

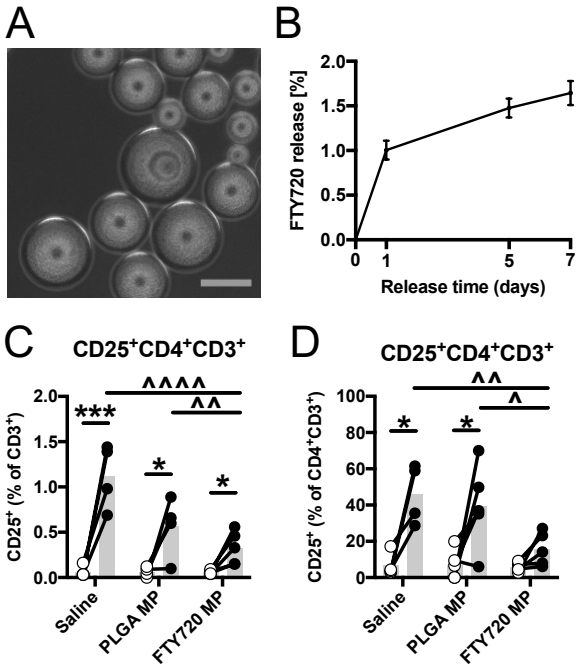

Figure 34. Effect of FTY720-releasing PLGA microparticles at acute day 7 time point. (A) Light microscopy image of PLGA microparticles (*scale bar* = 100 μm). (B) FTY720 release kinetics *in vitro* from PLGA (1:150) microparticles. Total dose delivered in vivo

was 10 μg. FTY720 release decreases the frequency of Treg cells within the T lymphocyte (C) and helper T lymphocyte (D) populations in SS muscle at day 7 (n=4-5, two-way ANOVA with repeated measures). *P<0.05, ***P<0.001, ^P<0.05, ^^P<0.01, ^^^^P<0.0001.

Contrary to the initial hypothesis, FTY720 microparticles do not affect levels of key cytokines and growth factors at day 7 compared to PLGA and untreated controls, as determined by a 22-plex protein immunoassay. Microparticle-mediated delivery of 1.1 μg FTY720 does not significantly affect SS wet mass at week 9 compared to untreated control and PLGA MPs; however, PLGA MPs significantly decrease mass compared to untreated control (**Figure 35b**). Similarly, PLGA MPs increase accumulation of $CD68^+$ MΦ and $CD206^+CD68^+$ M2-like MΦ at week 9 compared to untreated control, whereas FTY720 release returns $CD68^+$ and $CD206^+CD68^+$ counts to the same level as untreated control (**Figure 35c-f**). Decrease in muscle mass did not correlate strongly with $CD206^+CD68^+$ count (r^2 = 0.18, (**Figure 35g**), and the slope of the regression line did not significantly differ from zero.

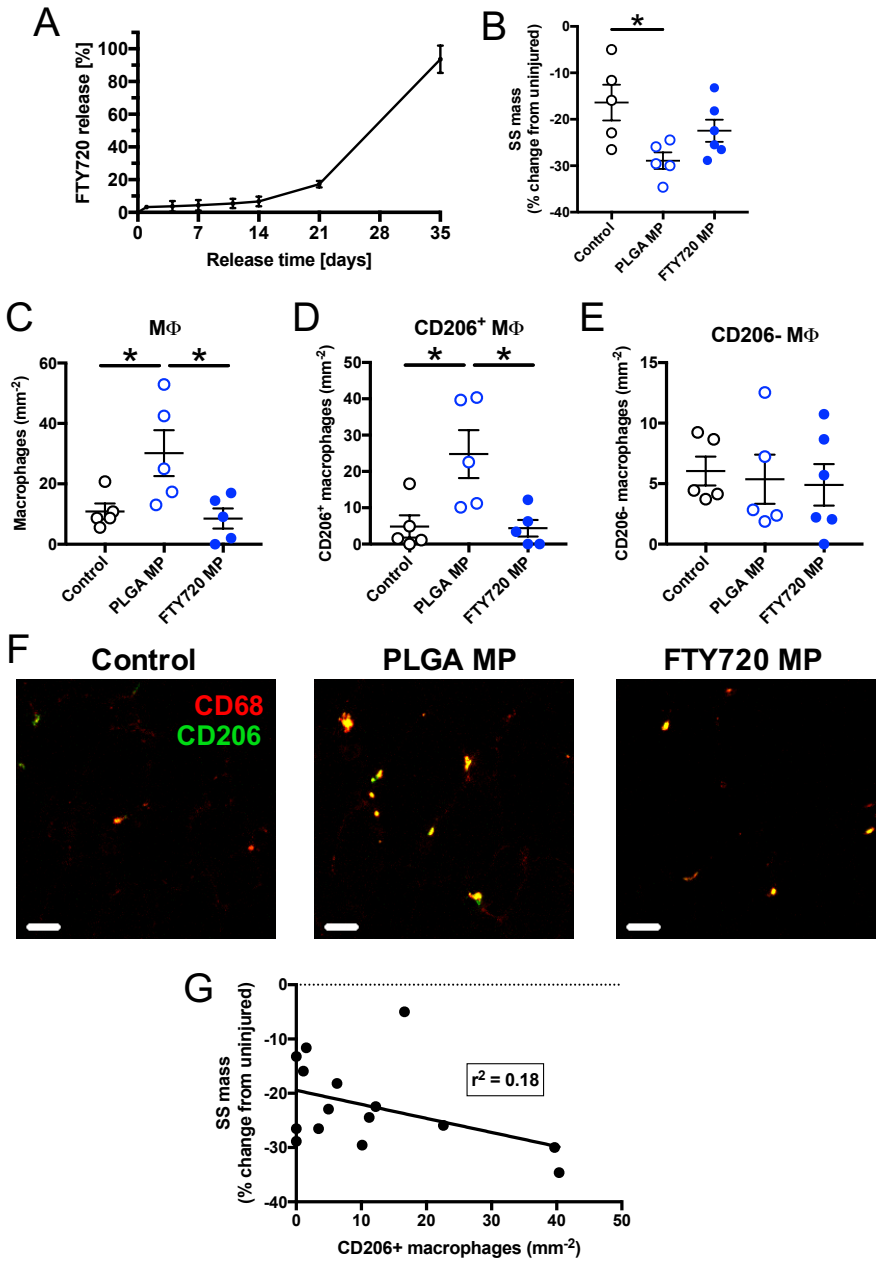

Figure 35. Effect of FTY720-releasing PLGA microparticles at chronic week 9 time point. (A) FTY720 release kinetics *in vitro* from PLGA (1:70) microparticles. (B) PLGA microparticles decrease the percent change in wet mass between injured SS and uninjured contralateral SS (B). Macrophage (C), CD206+ macrophage (D), and CD206- macrophage (E) counts as determined by cross-sectional IHC (F; *scale bar* = 20 μm). Change in SS mass does not negatively correlate with CD206+ macrophages (G; $r^2 = 0.18$). **P*<0.05 by ANOVA (n=5-6 animals).

5.2.8. Intramuscular injection of bolus FTY720 stimulates pro-inflammatory immune cell infiltration

Because of the atrophic effect of PLGA microparticles at week 9, we next investigated the effect of on-site delivery of FTY720 in the absence of biomaterial carriers. Bolus FTY720 (1 μg in 20 μL) was administered daily via intramuscular injection starting at the time of surgery, and immune cell infiltration was assessed at day 7 via flow cytometry. Daily FTY720 caused dramatically increased accumulation of MP (5.7-fold), MΦ (4.3-fold), MO (7.8-fold), and DC (3.8-fold) compared to vehicle control (**Figure 36**). FTY720 did not affect the proportion of M2-like or M1-like MΦ compared to vehicle (**Figure 37a-c**); however, both vehicle and FTY720 increased the proportion of $CCR7^{+}CD206^{-}$ M1-like MΦ compared to uninjured contralateral controls (**Figure 37d**). FTY720 decreased the proportion of "dual-activated" MΦ that positively express both CD206 and CCR7 (**Figure 37e**), decreased the proportion of $Ly6C^{lo}$ non-classical MO (**Figure 37f**), and increased the proportion of $Ly6C^{hi}$ classical MO (**Figure 37g**). FTY720 increased T_H count (**Figure 38a**) and enrichment of T lymphocytes in T_H subpopulation (**Figure 38b**) compared to both vehicle and uninjured contralateral controls. Daily FTY720 did not affect blood levels of circulating MO (**Figure 39a,b**), but did cause lymphopenia with regard to both the T_H and $CD8^{+}$ cytotoxic T lymphocyte subpopulations of circulating T lymphocytes (**Figure 37c,d**).

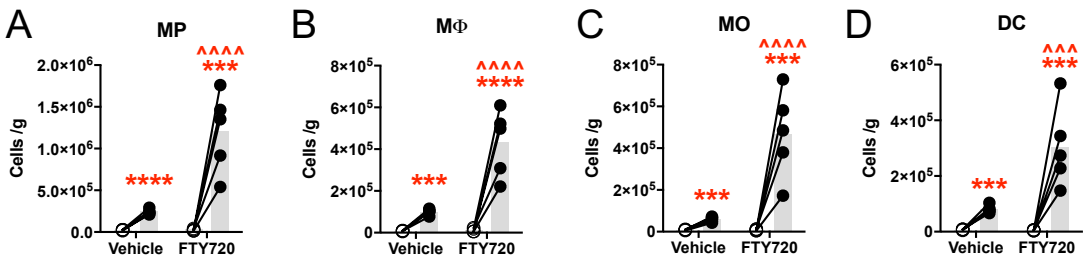

Figure 36. Daily on-site delivery of bolus FTY720 affects mononuclear phagocyte infiltration. FTY720 dramatically increases accumulation of mononuclear phagocytes (A), macrophages (B), monocytes (C), and dendritic cells (D) in SS muscle at day 7 compared to vehicle control and uninjured contralateral control. ***P<0.001, ****P<0.0001 compared to uninjured contralateral control, ^^^P<0.001, ^^^^P<0.0001 compared to vehicle control, as determined by two-way repeated measures ANOVA with post-hoc multiple comparisons test (n=5).

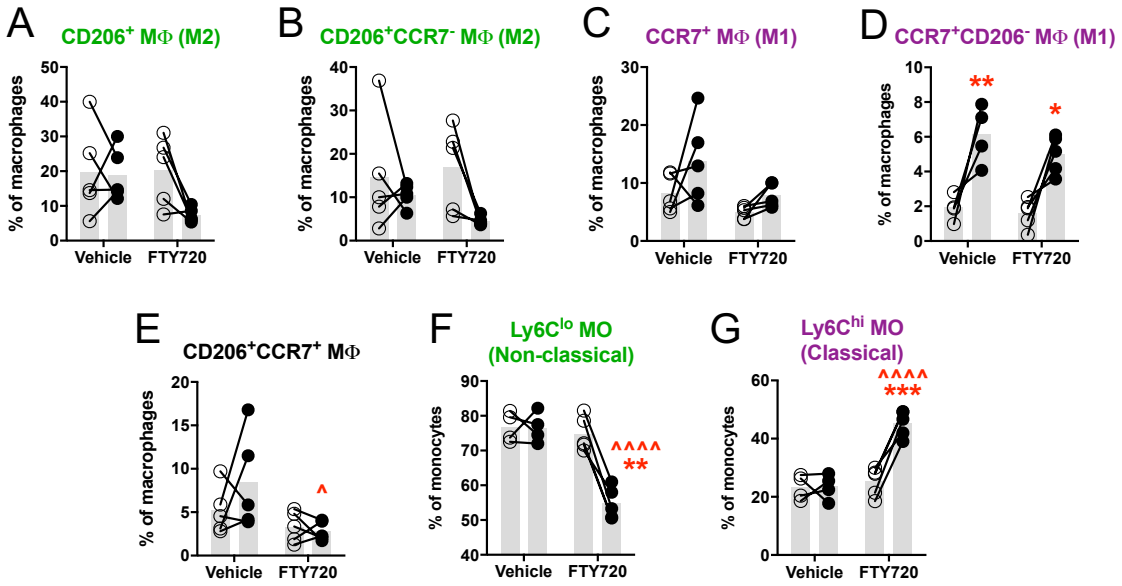

Figure 37. Mononuclear phagocyte subpopulations after daily on-site delivery of FTY720. (A,B) M2-like macrophages, (C,D) M1-like macrophages, (E) $CD206^{+}CCR7^{+}$ dual-activated macrophages, (F) $Ly6C^{lo}$ non-classical monocytes, and (G) $Ly6C^{hi}$ classical monocyte frequencies within their respective parent populations at day 7. *P<0.05, **P<0.01, ***P<0.001 compared to uninjured contralateral control, ^P<0.05, ^^^P<0.001, ^^^^P<0.0001 compared to vehicle control, as determined by two-way repeated measures ANOVA with post-hoc multiple comparisons test (n=5).

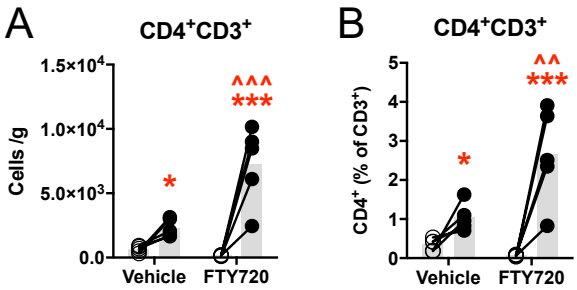

Figure 38. CD4$^+$ T_H lymphocytes after daily on-site delivery of FTY720. (A) T_H count and (B) T_H frequency within the T lymphocyte pool are increased by FTY720 compared to vehicle control and uninjured contralateral control. **P*<0.05, ****P*<0.001 compared to uninjured contralateral control, ^^*P*<0.01, ^^^*P*<0.001 compared to vehicle control, as determined by two-way repeated measures ANOVA with post-hoc multiple comparisons test (*n*=5).

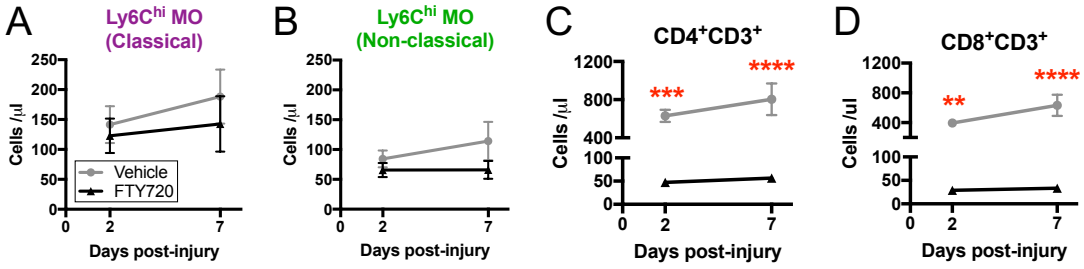

Figure 39. Immune cell count in blood circulation in response to RCT and daily on-site delivery of FTY720. (A) Ly6C^{hi} classical monocytes, (B) Ly6C^{lo} non-classical monocytes, (C) CD4$^+$ T_H lymphocytes, and (D) CD8$^+$ cytotoxic T lymphocytes. ***P*<0.01, ****P*<0.001, *****P*<0.0001 compared to vehicle control as determined by two-way repeated measures ANOVA with post-hoc multiple comparisons test (*n*=5).

5.3. Discussion

RCT treatment responses are poor, as non-operative management fails in approximately 50% of patients, leaving surgical tendon repair as the standard of care[172, 173]. The failure rate of surgery is as high as 26% for small to medium tears and up to 94% for large and massive tears[184-189]. Because muscle degeneration correlates highly with patient morbidities such as pain, functional deficiency, and post-surgical tear recurrence, prevention or reversal of muscle degeneration due to RCT could significantly improve treatment outcomes.

By selectively targeting subpopulations of MP that are present in the injury niche of the torn RC, new interventions may be found that harness endogenous inflammatory signaling to promote repair. Our group and others have previously investigated this therapeutic approach in diverse injury models, including volumetric muscle loss[130], peripheral nerve regeneration[2], bone regeneration[57, 153, 183], microvascular network growth[6, 53], and cardiovascular injury[190]. Application of immuno-regenerative biomaterial strategies to treat RCT requires a foundational understanding the subpopulations present and their functions in this injury context. The present study represents the first detailed quantification of inflammatory cell populations in SS muscle and their role in degeneration.

RCT injury causes dramatic infiltration of MP comprised of comparable frequencies of MΦ, MO, and DC. Injury skews the MΦ and MO pools toward non-classical $CD206^{+}$ and $Ly6C^{lo}$ subpopulations, respectively, and away from the classical $CCR7^{+}$ and $Ly6C^{hi}$ subpopulations. The impact of non-classical MΦ and MO on skeletal muscle has been partially elucidated in both acute and chronic injury contexts. After toxin-induced injury to skeletal muscle, $CD206^{+}$ MΦ and $Ly6C^{lo}$ MO accumulate during the secondary

phase of healing and are required for complete regeneration, likely because they stimulate myotube fusion[1]. COX-2^{lo} MΦ, which are phenotypically similar to $CD206^{+}$ MΦ, protect myotubes against atrophy *in vitro*[191]. In contrast, classical $Ly6C^{hi}$ MO promote chronic muscle degeneration in *mdx* mice[192]. Taken together, these findings suggest that non-classical MO and MΦ may support SS integrity compared to their classical counterparts that may feed forward degeneration. Here, depletion of circulating MO via liposomal clodronate accelerates SS atrophy. Because infiltration of circulating MO supplies the intramuscular MP pool[1], which is skewed toward non-classical MO and MΦ after RCT, these results suggest that non-classical MO and MΦ may protect against SS degeneration. Therefore, interventions that decrease MP accumulation may exacerbate outcomes after RCT. Toward the ultimate goal of therapeutic immunomodulation, follow-up studies should employ gain- and loss-of-function techniques to elucidate the functions of non-classical MO and MΦ in the context of SS degeneration and regeneration. Because these typically "pro-regenerative" MP subpopulations predominate the SS as early as day 7, increasing their recruitment may offer only modest therapeutic efficacy for muscle degeneration, which occurs over weeks.

MO and MΦ infiltration of SS muscle is less pronounced after RCT compared to other muscle injury contexts[193]. MO and MΦ counts are $2.3x10^4$ and $3.0x10^4$ cells/g at day 7 following TT+DN. In degenerative muscles of the *mdx* mouse model of muscular dystrophy, MΦ counts vary from $6x10^4$ to $3x10^6$ cells/g at 6-12 weeks of age[192, 194]. After toxin-induced skeletal muscle injury, MO/MΦ infiltration is dramatically higher, reaching a maximum of $1.4x10^7$ cells/g at day 7[155]. Myocardial infarction results in

massive infiltration of $4.5x10^7$ $Ly6C^{hi}$ and $3.0x10^7$ $Ly6C^{lo}$ MO/g at days 3 and 5-7, respectively[8]. Notably, the preceding examples involve direct injury to the muscle, whereas the RCT model herein primarily involves injury to tendon and nerve, with subsequent effects on rotator cuff muscles. That RCT results in less infiltration of MP compared to other muscle pathologies suggests that the underlying inflammatory stimuli may be less severe.

The present study represents a snap shot of the immune cell profile, which may change dynamically over time. The day 7 time point was selected because robust MP infiltration is detected at day 7 in numerous studies of soft tissue injury[6, 27, 130]. Evaluating multiple time points earlier and later than day 7 would elucidate whether the magnitude and phenotypic distribution of MP infiltration evolves temporally after RCT.

Infiltration of non-classical subpopulations after TT+DN injury was associated with increased production of pro-regenerative proteins, namely IL-10, IL-33, SDF-1α, IGF-1, Dkk-1, and basic FGF (bFGF). IL-10 is produced by non-classical monocytes and M2b and M2c macrophages, and polarizes MΦ toward M2c "regulatory macrophage" phenotype[10, 11]. IL-10 blunts inflammation by inhibiting the production and activity of various pro-inflammatory cytokines[11], and IL-10 switches muscle MΦ from a pro-inflammatory M1 to reparative M2 phenotype that promotes muscle regeneration after acute injury[195]. Local IL-33 rescues aged mouse impairment in Treg accumulation and acute muscle regeneration[20]. As described earlier, SDF-1α is involved in the recruitment of non-classical MO, and increased SDF-1α expression is associated with wound healing in various tissues[196]. IGF-1 down-regulates pro-inflammatory cytokines such as TNFα and IL-1β, accelerates muscle regeneration, and reduces muscle fibrosis[197]. MΦ-specific

expression of IGF-1 is required for acute muscle regeneration; after acute muscle injury, MΦ secrete IGF-1 which autopolarizes them toward reparative gene programs[63]. Wnt signlaing is in part responsible for the fibrotic bias of satellite cells during muscle healing in aged mice[198]. Intramuscular injection of dkk-1, an endogenous protein inhibitor of canonical Wnt signaling, reduces fibrosis in aged mice after acute muscle injury and in *mdx* mice[199]. Basic FGF (bFGF) promotes myoblast proliferation yet inhibits myoblast differentiation in vitro, and thus may promote the early phase of muscle regeneration[200]. Elevated bFGF is found in serum and muscles during chronic muscle degeneration in humans and mice with muscular dystrophy[201, 202]. Taken together, the results suggest that the cytokine and growth factor milieu in SS muscle after RCT is generally conducive to regeneration.

The ideal injury paradigm for pre-clinical investigation of RCT is controversial. Specifically, it is unclear whether denervation is an appropriate adjunct injury to tenotomy for modeling human pathogenesis. Clinically, the relationship between tendinopathy, suprascapular neuropathy, and muscle degeneration is unclear. Suprascapular neuropathy is present in only 8-12% of patients with full-thickness RCTs[203-207] and is likely caused by muscle retraction and increased tension on the suprascapular nerve[208]. Clinical studies contradict each other as to whether RCT-induced suprascapular neuropathy contributes to muscle degeneration[205, 209]. Nevertheless, in pre-clinical models, suprascapular denervation helps recapitulate the degree of muscle degeneration observed in human cases of RCT[69, 181, 182, 210]. In the present study, TT+DN increases MP, MO, and DC counts by at least 2-fold and slightly increases $CD206^{+}$ enrichment of the MΦ

pool compared to TT. These results show that inflammatory infiltrate in SS muscle is affected dramatically by denervation as an adjunct to tenotomy.

The biological cascade connecting RCT-induced muscle unloading to chronic muscle degeneration is unknown. Given that muscle anabolism and catabolism are coupled to physical activity[211], mechanical unloading after RCT likely causes myofiber atrophy by shifting muscle metabolism from anabolic to catabolic processes. The initial hypothesis of the present study is that MP infiltration exacerbates SS atrophy. According to this hypothesis, muscle unloading after RCT causes mitochondrial dysfunction[212], elaboration of damage associated molecular patterns (DAMPs), and recruitment of inflammatory cells that secrete pro-inflammatory cytokines (e.g. TNFα, IL-1β, IL-6)[8, 11, 23, 24], which then stimulate catabolism of intramyocellular proteins over weeks[65]. However, results here suggest that MP infiltration protects against SS atrophy in mice. Future studies are required to elucidate the etiology of RC muscle degeneration.

The impact of subpopulations of T lymphocytes on skeletal muscle is increasingly recognized. In agreement with the report that T lymphocytes are dispensable for the development of fatty degeneration in rats[67], RCT does not affect T lymphocyte count in mouse SS muscle. However, RCT enriches the T lymphocyte pool in T_H and T_{reg} subpopulations. Multivariate analysis reveals injury type-specific differences in T lymphocyte populations not detected by individual measurements; TT+DN is discriminated from TT by increased overall T lymphocyte frequency and decreased T_{reg} frequency within the T_H pool. T_H are required for biomaterial-induced non-classical MΦ polarization and muscle regeneration after volumetric muscle loss[28]. T_{reg} aid repair of acutely injured skeletal muscle, possibly because they encourage MP to switch from

classical to non-classical phenotypes[213]. Deficient T_{reg} accumulation in aged mice impairs acute muscle regeneration[20]. Thus, enrichment of the T_H and T_{reg} fractions may confer protective effects on SS muscle after RCT. Moving forward, one intriguing hypothesis is that aging may exacerbate RCT-induced muscle degeneration due to deficient accumulation of T_H or T_{reg} subpopulations.

SDF-1α-releasing, hydrolytically degradable Hep^{-N}-PEGDA microparticles were injected into SS muscle at the time of RCT injury to test the hypothesis that local delivery of SDF-1α would recruit non-classical MO at the acute week 1 time point. SDF-1α skewed the MΦ pool toward dual expression of the M1 (CCR7) and M2 (CD206) markers. There are no reported functions *in vitro* or *in vivo* of this dual polarized phenotype. Dual $CD206^{+}CCR7^{+}$ polarization possibly reflects the highly plastic nature of MΦ and their ability to integrate a multitude of microenvironmental signals, which may consist of pro-inflammatory and anti-inflammatory cues simultaneously. Future studies could employ single cell qPCR to compare the function of dual polarized MΦ to other MΦ subpopulations via broad gene expression.

Subsequent studies of therapeutic drug delivery pivoted to local delivery of FTY720-encapsulating PLGA microparticles for multiple reasons. First, data from SDF-1α delivery did not suggest unambiguous pro-regenerative effects on immune cell recruitment. Second, our lab previously showed that FTY720 stimulation of MO *in vitro* and injured skin *in vivo* causes cytokine secretion to shift the balance from pro-inflammatory to pro-regenerative factors. Lastly, Hep^{-N} microparticles exhibit rapid release of FTY720 by 24 h, whereas PLGA microparticles can sustain the release of FTY720 over multiple weeks.

At the early week 1 time point, FTY720 release from PLGA microparticles decreases the frequency of Treg within the T_H and T cell populations. Decreased Treg frequency may be caused by multiple processes, including decreased recruitment, proliferation, survival, retention, or differentiation of Treg, or an increase in these processes in other T lymphocyte populations. In light of literature reporting pro-regenerative effects of Treg on skeletal muscle, decreased Treg frequency caused by FTY720 may exacerbate muscle degeneration. At the late week 9 time point, FTY720 release had no significant effect on SS atrophy, whereas control PLGA microparticles exacerbated atrophy. PLGA microparticles increased accumulation of macrophages, particularly $CD206^+$ M2-like macrophages. SS atrophy did not correlate with $CD206^+$ macrophage count, suggesting that $CD206^+$ macrophages likely do not exert atrophic effects on SS muscle. The acidic products of PLGA degradation, lactic acid and glycolic acid, may negatively regulate muscle mass[214], but additional experiments would be necessary to test this hypothesis.

To investigate on-site FTY720 in the absence of atrophic PLGA microparticles, bolus FTY720 was injected into SS muscle daily. FTY720 exhibited broad pro-inflammatory effects, increasing the accumulation of all MP populations, increasing the frequency of classical MO, and decreasing the frequency of non-classical MO. Interestingly, bolus FTY720 decreased the frequency of $CD206^+CCR7^+$ dual polarized MΦ, similar to the effect of SDF-1α delivery from Hep^{-N} microparticles. FTY720-induced patterns of MP accumulation were unlikely to result from systemic effects on circulating MO, given that blood counts of classical and non-classical MO did not differ between FTY720 and control. FTY720 dramatically increased T_H accumulation despite causing

lymphopenia in blood. Divergent immunomodulatory effects due to daily injection versus sustained polymeric release of FTY720 may be explained by additional injury stimuli introduced by injections. Repeated injections likely injure myofibers, thereby creating a profile of DAMPs, cytokines, and endothelial adhesion signatures that differ from SS muscle experiencing indirect injury via tendon and nerve transection.

Inability of local delivery of SDF-1 and FTY720 to induce pro-regenerative cell recruitment and protein production after murine RCT contrasts with prior studies indicating such effects in the murine dorsal skin window model[6, 27, 215]. The disparity may suggest that the effects of SDF-1 and FTY720 on inflammation are highly context-dependent. Moreover, given that the murine SS is biased naturally toward non-classical monocyte/macrophage subpopulations and regenerative proteins after RCT, the therapeutic window for immune modulation may be limited. To identify additional therapeutic targets, deeper investigation of the mechanisms underlying SS degeneration and regeneration are necessary.

5.4. Materials and Methods

5.4.1. Mouse model of massive rotator cuff injury

All animal procedures were conducted according to protocols approved by the Georgia Tech Institutional Animal Care and Use Committee. Male C57bl/6 mice aged 8 weeks were anesthetized using vaporized isoflurane (5% for induction and 2% for maintenance). Sustained-release buprenorphine was administered i.p. for analgesia. The right shoulder served as the injured group and the contralateral shoulder served as the

uninjured control group. The right arm and chest were shaved, depilated, and sterilized using triplicate alternating washes of alcohol and chlorhexidine. Using a No. 11 scalpel blade, a lateral incision in the skin was made from the midline to the humeral head. Fascia was removed by blunt dissection. To expose the glenohumeral joint, the deltoid was split by making a ~5mm incision from the clavicle to the superior-lateral region of the humerus. The supraspinatus and infraspinatus tendons were sharply transected using the scalpel blade. The suprascapular nerve (SSN) was located by creating a small incision in the pectoralis major and bluntly dissecting the muscle. The SSN was severed using surgical microscissors. The deltoid and pectoralis were closed using absorbable 4-0 sutures and the skin was closed using wound clips. Mice were allowed unrestricted ambulation after awakening from anesthesia.

5.4.2. Flow cytometry

For blood analysis, blood samples were collected via retro-orbital sinus. For SS muscle analysis, mice were euthanized by CO_2 asphyxiation 7 days after injury to analyze cellular inflammation in the muscle. To generate single cell suspensions from blood, RBCs were lysed by suspension in ammonium chloride for 10 min. To generate single cell suspensions from muscles, tissue was minced, digested in 1mg/mL collagenase IA for 45 min at 37°C, filtered through membranes with 40µm pore size, and resuspended in 3% FBS for immunostaining. Cell suspensions were immunostained for 30 min on ice followed by fixation in 2% PFA for 10 min and addition of CountBright™ Absolute Counting Beads. The following antibody panel was used: MerTK-PE (clone 108928; R&D Systems),

CCR7-PE/Cy7 (clone 4B12; BioLegend), CD3-FITC (17A2; BioLegend), CD25-PerCP/Cy5.5 (clone PC61; BioLegend), Ly6C-APC (clone HK1.4, BioLegend), Ly6G-APC/Cy7 (clone 1A8; BioLegend), CD11c-BV421 (clone N418; BioLegend), CD11b-BV510 (clone M1/70; BioLegend), CD206-BV605 (clone C068C2; BioLegend), CD64-BV711 (clone X54-5/7.1; BioLegend), and CD4-BV785 (clone GK1.5; BioLegend). To discriminate positive versus negative expression of each marker, the fluorescence-minus-one (FMO) approach was used. Briefly, excess cell suspension was immunostained with all antibodies except the marker of interest. The threshold of positive versus negative expression of the marker of interest was then set at the level of the most highly fluorescent events in the marker's corresponding channel. Samples were run on a BD FACS Aria IIIu cytometer and data was analyzed using FlowJo software. Cells were immunophenotyped according to the following gating scheme: macrophage, $MerTK^{+}CD64^{+}$; dendritic cell, $NOT(MerTK^{+}CD64^{+})CD11c^{+}$; monocyte, $NOT(MerTK^{+}CD64^{+})CD11c^{-}CD11b^{+}SSC^{lo}$; neutrophil, $Ly6G^{+}SSC^{hi}$; T lymphocyte, $CD3^{+}$; helper T lymphocyte, $CD3^{+}CD4^{+}$; regulatory T lymphocyte, $CD3^{+}CD4^{+}CD25^{+}$. Metrics reporting cell count normalized to muscle mass were calculated according to the equation $N = N_g*B_a/(B_m*M)$, where N_g is the number of cells counted in the gate-of-interest, B_a is number of counting beads added to the sample, B_m is the number of counting beads measured by the cytometer, and M is the wet muscle mass. Metrics reporting frequency were calculated by dividing the number of cells in the gate-of-interest by the number of cells in a particular upstream gate.

5.4.3. Principal component analysis

Unsupervised principal component analysis was performed using Matlab. The following 11 variables from flow cytometry were used as inputs to the model: muscle mass, MΦ (% of cells), MO (% of cells), DC (% of cells), T lymphocyte (% of cells), neutrophil (% of cells), $CD206^+$ (% of MΦ), $CCR7^+$ (% of MΦ), $Ly6C^{lo}$ (% of MO), T_H ($CD4^+CD3^+$ % of $CD3^+$), and T_{reg} ($CD25^+CD4^+CD3^+$ % of $CD4^+CD3^+$). Ly6Chi (% of MO) was omitted because the value equals 1 – $Ly6C^{lo}$. Data were scaled to unit variance and mean centered. Regarding quality of fit, Hoetelling's T2 and DModX are less than critical values for all observations. For PC1, $R^2 = 0.575$ and $Q^2 = 0.431$. For PC2, $R^2 = 0.166$ and $Q^2 = 0.064$.

5.4.4. Clodronate-liposome administration and myofiber diameter analysis

Intravenous administration of liposomal clodronate causes complete depletion of blood MO within 6 h followed by recovery of the $Ly6C^{hi}$ and $Ly6C^{lo}$ MO populations at 2 and 7 days, respectively[178]. To deplete circulating monocytes in the present study, liposomal clodronate (100μL per 10g of body weight; Dr. Nico van Rooijen, clodronateliposomes.org) or saline control was administered i.v. via jugular vein injection every 2-3 days according to the timeline in Figure 32. Supraspinatus atrophy was assessed by wet mass and IHC analysis of myofiber cross-sectional area at day 21 post-injury. To prepare muscles for IHC, mouse vasculature was perfused with 0.9% saline followed by 4% paraformaldehyde and then muscles were harvested and snap frozen in liquid nitrogen-cooled 2-methylbutane. Muscle cross-sections (thickness: 10 μm) were acquired using a cryostat (Leica CryoStar NX70). Immunohistochemistry was performed on cross-sections

by staining with goat anti-collagen IV (Millipore AB769) and donkey anti-goat conjugated to DyLight 594 (abcam ab96933). Fluorescence was visualized at 594 nm excitation using a Zeiss LSM 710 NLO confocal microscope. Regions of interest were selected to include most of the muscle cross-section interior and exclude the periphery. Semi-automated quantification of myofiber diameter was performed in ImageJ by manually thresholding pixel intensity, automatically detecting edges using the "Find Edges" process, and quantifying diameter of each myofiber using the "WandAutoMeasure" tool. To account for variation in number of myofibers quantified, equal numbers of myofibers were randomly selected from each animal, pooled, and subjected to statistical analysis (n=964 across 4 animals per group).

5.4.5. Hep^{-N} microparticle fabrication

10 wt% Hep^{-N} microparticles were fabricated via water-and-oil single emulsion. 50.0 mg PEGDA and 0.92-1.85 mg dithiothreitol (DTT, 20-40 mM, Sigma) were added to 273 μL 10 wt% bovine serum albumin (BSA, Thermo) solution in PBS and incubated at 37°C for 30 mins to allow for Michael-type addition between PEGDA and DTT. Next, 5.6 mg Hep^{-N}MAm was added and the aqueous phase was incubated for an additional 30 mins.

27 μL of 0.05 wt% Irgacure 2959 photoinitiator (Ciba) was added, and the aqueous phase was pipetted drop-wise into an oil phase containing 5 mL mineral oil (Amresco) and 3.0-3.2 μL Span80 (TCI). The mixture homogenized at 4000 RPM (Polytron PT 3100, Kinematica) for 5 mins. The water-and-oil emulsion was nitrogen purged for 1 min and treated with UV irradiation (~15 mW/cm^2) for 10 mins to enable free radical

polymerization between PEGDA and Hep^{-N}MAm. Finally, the microparticle solution was separated from the oil phase by centrifugation and washed with dH_2O, then pipetted through 40 μm porous membrane strainers to remove microparticles under 40 μm in diameter.

Once fabricated, microparticles were sterilized in 70% ethanol for 30 mins and washed in sterile PBS. MPs were imaged via phase microscopy. Microparticles were stored in sterile PBS at 4°C and used within 2 weeks of fabrication.

5.4.6. SDF-1α loading and release from Hep^{-N} microparticles

To load SDF-1α onto Hep^{-N} microparticles, 1.0-1.2 μg human SDF-1α (R&D Systems) was added to 0.6 mg MPs in 50 μL 0.1 wt% BSA solution and incubated for 2 hours at 4°C, after which time microparticles were rinsed by adding an additional 450 μL 0.1 wt% BSA solution. Microparticles were centrifuged for 3 mins at 10,000 RCF and 495 μL supernatant was removed.

For *in vitro* SDF-1α release studies, the removed supernatant was replaced with fresh 0.1 wt% BSA solution and samples were incubated at 37°C until designated time points, when media was exchanged for protein analysis. SDF-1α protein was quantified using a human SDF-1α ELISA kit (R&D Systems).

FTY720-loaded PLGA microparticle fabrication

FTY720-loaded PLGA microparticles were fabricated using established single emulsion technique. Briefly, FTY720 (Cayman Chemical) dissolved in DMSO (20 mg/mL) was mixed at a mass ratio of 1:70 (9 week study) or 1:150 (7 day study) with PLGA (50:50 copolymer ratio) dissolved in methylene chloride (20% wt/v). Polymer solution was added dropwise to poly(vinyl alchohol) solution (2% w/v, aqueous) under constant homogenization at 4000 RPM for 1 min. Resultant microparticle suspension was stirred for 3 h to evaporate solvent, sieved through a porous membrane (40 μm pore size) to isolate particles larger than 40 μm, and washed 3 times in deionized water. Control PLGA microparticles were fabricated using the same process but with FTY720 absent from the initial DMSO solution. For *in vivo* studies, equivalent fractions of the total batch volume were taken from FTY720 and PLGA microparticle batches.

In vitro release of FTY720 from PLGA microparticles

FTY720-encapsulating PLGA microparticles were suspended in simulated body fluid with 4% fatty acid-free BSA and incubated at 37°C. Media was exchanged at designated time points to quantify FTY720. FTY720 was isolated from samples by lipid extraction. Briefly, samples were added to 2:1 CH_3OH:$CHCl_3$ solution and heated at 48°C overnight. Glycerophospholipids were degraded by heating at 37C for 2 h in the presence of KOH. The pH was neutralized with acetic acid, solvent was evaporated using a SpeedVac concentrator, and samples were dissolved in 72:29:1 CH_3OH:H_2O:HCOOH solution. For LC-MS/MS analysis, samples were injected into a C18 chromatography

column upstream of a Micromass Quattro LC triple quadrupole tandem mass spectrometer operating under electrospray ionization.

Intramuscular injection of therapeutics

Microparticles (20 μL volume) were injected directly into the SS muscle during surgery using insulin syringe. To administer soluble FTY720 daily, mice were anesthetized with vaporized isoflurane, the scapula was gently restrained, the insulin syringe was passed through the skin into the SS muscle, and FTY720 solution (20 μL sterile saline) was injected.

Multiplex cytokine immunoassay

SS muscles were minced, disaggregated physically in the presence of protease/phosphatase inhibitor, and lysed using cell lysis buffer (Cell Signaling Technology) for 45 min on ice. Protein supernatant was isolated after centrifugation at 14000 RPM for 15 min. A custom 22-plex protein immunoassay kit (R&D Systems) was used to quantify key cytokines and growth factors using Luminex MAGPIX® system. Each sample was run in duplicate and averaged. BCA assay was used to quantify total protein for data normalization.

Macrophage IHC

Muscles were snap frozen in liquid nitrogen-cooled isopentane, and frozen sections (10 μm thick) were acquired from the muscle belly via cryostat. Sections were blocked with 5% mouse serum for 1 h, washed, incubated with rat anti-mouse CD68-AF647 (1:200, AbSerotec) and CD206-AF488 (1:200, AbSerotec) in 2.5% mouse serum overnight at 4°C, washed, and mounted with Vectashield. Z-stacked confocal images were acquired using a Zeiss 710 NLO confocal microscope. To quantify $CD68^+$ MΦ and $CD206^+CD68^+$ M2-like MΦ, two representative regions of interest were selected in each section and cells were counted manually based on fluorescence intensity.

5.4.7. Statistical analysis

In Figure 26, Figure 27, Figure 28, and Figure 29, statistical comparisons were conducted in GraphPad Prism using repeated measures two-way ANOVA followed by Sidak multiple comparisons test. Figure 32 was analyzed by t-test (Panel c) and Mann-Whitney test (Panel e,f,g).

6. FUTURE DIRECTIONS

6.1. Immune cell characterization

While the present studies utilize well-accepted paradigms to characterize mononuclear phagocyte phenotypes, the field of immune biology continues to elucidate additional layers of heterogeneity and complexity within the mononuclear phagocyte system. For example, multiple subpopulations of M2 macrophages (M2a, b, c) have been identified from divergent polarization schemes *in vitro*. Future work could employ intracellular cytokine staining and additional extracellular markers to distinguish between M2a-c subpopulations. Nevertheless, it is unclear how well immunophenotypes *in vitro* describe cell functions *in vivo*. Macrophages integrate myriad signals in their microenvironment and are highly plastic cells. To determine changes in macrophage function and phenotype *in vivo* in response to perturbation, future studies could employ high-dimensional, single-cell analytical techniques such as single-cell qPCR and highly multiplexed mass cytometry. By analyzing a panel of genes governing established and putative macrophage functions, single-cell qPCR would enable evaluation of cell function at the transcription level and, using hierarchical clustering, identification of potentially novel functional subpopulations. Highly multiplexed mass cytometry may also enable identification of novel subpopulations at the level of surface marker expression.

6.2. Fractalkine aptagels

Future directions of the aptagel platform include further mechanistic investigation, material modifications, and evaluation in more clinically-relevant animal models. Although the present study demonstrated enrichment of endogenous fractalkine within aptagels, the gradient within surrounding tissue was unknown. Additional experiments could investigate the spatiotemporal dynamics of the endogenous fractalkine gradient using concentric biopsies and ELISA.

Toward the goal of clinical translation, future studies could employ computational modelling or experimentation with mutated or modified aptamers[86, 126] to identify if better enrichment kinetics exist and to enable enrichment of hFKN. The ability to alter formulations may enable application to diverse clinical contexts. For example, aptabeads or aptamer-functionalized nanoparticles[146] may be advantageous when injury occurs deep within tissue and bulk hydrogel implantation is not feasible, such as after brain injury (e.g. trauma or stroke). Elevated FKN is associated with improved healing after brain injury[80-82] but while FKN concentration rises initially and drives $CX3CR1^+$ cell recruitment, FKN levels soon fall rapidly[127]. FKN-aptabeads could prolong $CX3CR1^+$ cell recruitment by storing FKN during the early surplus and releasing it during later days as FKN levels decline. Other critical molecules can be targeted by identifying binding aptamers via SELEX and tuning aptamer kinetics via selection pressures, mutations, truncations, and additions[86]. Through this, combinations of aptamers could be immobilized on biomaterials to treat complex pathological conditions in which regulation or enrichment of multiple proteins is required. Lastly, DNAse dampened fractalkine-binding functionality in vitro in the present study, suggesting that incorporation of DNAse

resistant bases may further amplify FKN enrichment and consequent recruitment of $CX3CR1^{+}$ cells.

6.3. Heparin-functionalized hydrogels

To leverage the proangiogenic/proarteriogenic effects of heparin-functionalized hydrogels toward major unmet clinical indications, future studies could evaluate this platform in more rigorous and clinically-relevant animal models. Chronic ischemic pathologies, such as peripheral and cardiac arterial disease, are strategic targets because therapeutic arteriogenesis restores perfusion and because no existing therapies induce durable perfusion. Hindlimb ischemia via arterial ligation is the standard animal model of peripheral arterial disease. Future work could test whether local, intramuscular delivery of SDF-1 and/or FTY720 from degradable heparin-functionalized microparticles stimulates hindlimb arteriogenesis and perfusion. The proangiogenic hydrogel platform may also prove efficacious in wound healing indications in which neovascularization is critical, such as massive trauma to peripheral nerve, bone, and muscle. Broader applications include other contexts in which recruitment of anti-inflammatory immune cell subsets may be therapeutic by inducing tolerance or resolving inflammation, such as vascularized composite allografts (VCA), chronic cutaneous wounds, and chronic inflammatory diseases amenable to biomaterial implantation.

6.4. Muscle degeneration due to rotator cuff tear

Future studies related to rotator cuff injury should address outstanding questions about underlying immune biology, utilize a more clinically relevant injury paradigm, and investigate promising alternative immunomodulatory therapeutics. To assess how specific subpopulations affect rotator cuff muscle degeneration, loss- and gain-of-function techniques could be employed. The role of each circulating monocyte subpopulation can be implicated using $CCR2^{-/-}$ and $NR4A1^{-/-}$ transgenic mice, which present reduced circulating levels of Ly6Chi classical and Ly6Clo non-classical monocytes, respectively. To determine molecular mechanisms by which inflammation affects degeneration, putative catabolic cytokines (e.g. TNFα) could be knocked down via administration of siRNA, neutralizing antibodies, or small molecule inhibitors. Specific cell populations could be implicated in the production of degenerative factors via transgenic mice lacking expression of a target gene in a specific cell lineage; for example, crossing $Csf1r^{cre}$ mice with $Il6^{fl/fl}$ mice yields offspring lacking expression of IL-6 in monocytes and macrophages. Gain-of-function techniques include intramuscular injection of cytokines or macrophages pre-polarized toward divergent phenotypes such as M1 vs. M2a-c. The biological cascade connecting RCT-induced muscle unloading to chronic muscle degeneration is unknown. Given that muscle anabolism and catabolism are coupled to physical activity, mechanical unloading after RCT likely causes myofiber atrophy by shifting muscle metabolism from anabolic to catabolic processes. Future studies could investigate an immune-centric hypothesis whereby muscle unloading after RCT causes mitochondrial dysfunction, elaboration of damage associated molecular patterns (DAMPs), and recruitment of inflammatory cells that secrete factors that may have degenerative and/or protective effects.

Recapitulation of human disease characteristics in animal models is critical to improve the likelihood that preclinical data provide meaningful insight into clinical biology. In the present studies of rotator cuff injury, potential treatments are evaluated for their ability to modulate inflammation and protect against denaturation when the tendon and nerve remain transected. Although slowing degeneration is desirable, it is unlikely that therapeutic perturbations will produce durable responses in the absence of mechanical loading and innervation. In the clinic, diagnosis of RCT occurs late when muscle degeneration is progressed. The clinical treatment paradigm of muscle-focused therapies is likely to involve surgical tendon reattachment followed by intramuscular injections. Future studies should utilize rats or rabbits to investigate an experimental paradigm in which supraspinatus muscle is allowed to degenerate chronically after tenotomy and then reattached prior to treatment. To further increase translational relevance of the project, human muscle biopsy samples could be compared to rodents. Single cell qPCR analysis would provide high-dimensional insight into the phenotype and function of immune cells in human supraspinatus. Given the modest effects of SDF-1/FTY720 delivery in these rotator cuff studies, future work should investigate additional candidate therapeutics. For example, delivery of pro-resolving lipid mediators such as resolvin D1 (RvD1) has shown efficacy in other chronic inflammatory contexts.

APPENDIX

Publications

Note: [1] indicates co-first authorship

1. **Krieger J**, Tellier L, Ollukaren M, Botchwey E, Temenoff J. "Quantitative analysis of immune cell subset infiltration in the supraspinatus muscle after massive rotator cuff injury." *Regen Eng & Transl Med.* 2017. doi: 10.1007/s40883-017-0030-2.

2. Olingy C, San Emeterio C, Ogle M, **Krieger J**, Bruce A, Pfau D, Jordan B, Peirce S, Botchwey E. "Non-classical monocytes are biased progenitors of wound healing macrophages during soft tissue injury." *Sci Rep*. 2017 Mar 27;7(1):447. doi: 10.1038/s41598-017-00477-1.

3. Ogle M[1], **Krieger J[1]**, Tellier L, McFaline-Figueroa J, Temenoff J, Botchwey E. "Dual affinity heparin-based hydrogels achieve pro-regenerative inflammation and microvascular remodeling." *ACS Biomat Eng & Sci*. doi: 10.1021/acsbiomaterials.6b00706.

4. **Krieger J[1]**, Ogle M[1], McFaline-Figueroa J, Segar C, Temenoff J, Botchwey E. "Spatially localized recruitment of anti-inflammatory monocytes by SDF-1α-releasing hydrogels enhances microvascular network remodeling." *Biomaterials*. 2016 Jan;77:280-90. doi: 10.1016/j.biomaterials.2015.10.045.

5. Wang T[1], **Krieger J[1]**, Huang C, Das A, Francis MP, Ogle R, Botchwey E. "Enhanced osseous integration of human trabecular allografts following surface modification with bioactive lipids." *Drug Deliv Transl Res*. 2016 Apr;6(2):96-104. doi: 10.1007/s13346-015-0244-0.

6. Enam S[1], **Krieger J[1]**, Saxena T, Watts B, Botchwey E, Bellamkonda R. "*In vivo* enrichment of endogenous fractalkine and anti-inflammatory cells via aptamer-functionalized hydrogels." *Under review*.

REFERENCES

[1] L. Arnold, A. Henry, F. Poron, Y. Baba-Amer, N. van Rooijen, A. Plonquet, R.K. Gherardi, B. Chazaud, Inflammatory monocytes recruited after skeletal muscle injury switch into antiinflammatory macrophages to support myogenesis, J Exp Med 204(5) (2007) 1057-69.

[2] N. Mokarram, A. Merchant, V. Mukhatyar, G. Patel, R.V. Bellamkonda, Effect of modulating macrophage phenotype on peripheral nerve repair, Biomaterials 33(34) (2012) 8793-801.

[3] N. Mokarram, R.V. Bellamkonda, A perspective on immunomodulation and tissue repair, Ann Biomed Eng 42(2) (2014) 338-51.

[4] R. Shechter, A. London, C. Varol, C. Raposo, M. Cusimano, G. Yovel, A. Rolls, M. Mack, S. Pluchino, G. Martino, S. Jung, M. Schwartz, Infiltrating blood-derived macrophages are vital cells playing an anti-inflammatory role in recovery from spinal cord injury in mice, PLoS Med 6(7) (2009) e1000113.

[5] R. Shechter, M. Schwartz, Harnessing monocyte-derived macrophages to control central nervous system pathologies: no longer 'if' but 'how', J Pathol 229(2) (2013) 332-46.

[6] A.O. Awojoodu, M.E. Ogle, L.S. Sefcik, D.T. Bowers, K. Martin, K.L. Brayman, K.R. Lynch, S.M. Peirce-Cottler, E. Botchwey, Sphingosine 1-phosphate receptor 3 regulates recruitment of anti-inflammatory monocytes to microvessels during implant arteriogenesis, Proc Natl Acad Sci U S A 110(34) (2013) 13785-90.

[7] A.J. Clover, A.H. Kumar, N.M. Caplice, Deficiency of CX3CR1 delays burn wound healing and is associated with reduced myeloid cell recruitment and decreased sub-dermal angiogenesis, Burns 37(8) (2011) 1386-93.

[8] M. Nahrendorf, F.K. Swirski, E. Aikawa, L. Stangenberg, T. Wurdinger, J.L. Figueiredo, P. Libby, R. Weissleder, M.J. Pittet, The healing myocardium sequentially mobilizes two monocyte subsets with divergent and complementary functions, J Exp Med 204(12) (2007) 3037-47.

[9] A. ElAli, N. Jean LeBlanc, The Role of Monocytes in Ischemic Stroke Pathobiology: New Avenues to Explore, Front Aging Neurosci 8 (2016) 29.

[10] M.E. Ogle, C.E. Segar, S. Sridhar, E.A. Botchwey, Monocytes and macrophages in tissue repair: Implications for immunoregenerative biomaterial design, Exp Biol Med (Maywood) 241(10) (2016) 1084-97.

[11] D.M. Mosser, J.P. Edwards, Exploring the full spectrum of macrophage activation, Nat Rev Immunol 8(12) (2008) 958-69.

[12] J.W. Godwin, A.R. Pinto, N.A. Rosenthal, Macrophages are required for adult salamander limb regeneration, Proc Natl Acad Sci U S A 110(23) (2013) 9415-20.

[13] L. Li, B. Yan, Y.Q. Shi, W.Q. Zhang, Z.L. Wen, Live imaging reveals differing roles of macrophages and neutrophils during zebrafish tail fin regeneration, J Biol Chem 287(30) (2012) 25353-60.

[14] R. van Furth, Z.A. Cohn, The origin and kinetics of mononuclear phagocytes, J Exp Med 128(3) (1968) 415-35.

[15] F. Ginhoux, S. Jung, Monocytes and macrophages: developmental pathways and tissue homeostasis, Nat Rev Immunol 14(6) (2014) 392-404.

[16] S.J. Jenkins, D. Ruckerl, P.C. Cook, L.H. Jones, F.D. Finkelman, N. van Rooijen, A.S. MacDonald, J.E. Allen, Local macrophage proliferation, rather than recruitment from the blood, is a signature of TH2 inflammation, Science 332(6035) (2011) 1284-8.

[17] D. Hashimoto, A. Chow, C. Noizat, P. Teo, M.B. Beasley, M. Leboeuf, C.D. Becker, P. See, J. Price, D. Lucas, M. Greter, A. Mortha, S.W. Boyer, E.C. Forsberg, M. Tanaka, N. van Rooijen, A. Garcia-Sastre, E.R. Stanley, F. Ginhoux, P.S. Frenette, M. Merad, Tissue-resident macrophages self-maintain locally throughout adult life with minimal contribution from circulating monocytes, Immunity 38(4) (2013) 792-804.

[18] S. Yona, K.W. Kim, Y. Wolf, A. Mildner, D. Varol, M. Breker, D. Strauss-Ayali, S. Viukov, M. Guilliams, A. Misharin, D.A. Hume, H. Perlman, B. Malissen, E. Zelzer, S. Jung, Fate mapping reveals origins and dynamics of monocytes and tissue macrophages under homeostasis, Immunity 38(1) (2013) 79-91.

[19] U.M. Gundra, N.M. Girgis, D. Ruckerl, S. Jenkins, L.N. Ward, Z.D. Kurtz, K.E. Wiens, M.S. Tang, U. Basu-Roy, A. Mansukhani, J.E. Allen, P. Loke, Alternatively activated macrophages derived from monocytes and tissue macrophages are phenotypically and functionally distinct, Blood 123(20) (2014) e110-22.

[20] W. Kuswanto, D. Burzyn, M. Panduro, K.K. Wang, Y.C. Jang, A.J. Wagers, C. Benoist, D. Mathis, Poor Repair of Skeletal Muscle in Aging Mice Reflects a Defect in Local, Interleukin-33-Dependent Accumulation of Regulatory T Cells, Immunity 44(2) (2016) 355-67.

[21] A. Mantovani, A. Sica, S. Sozzani, P. Allavena, A. Vecchi, M. Locati, The chemokine system in diverse forms of macrophage activation and polarization, Trends Immunol 25(12) (2004) 677-86.

[22] K.L. Spiller, R.R. Anfang, K.J. Spiller, J. Ng, K.R. Nakazawa, J.W. Daulton, G. Vunjak-Novakovic, The role of macrophage phenotype in vascularization of tissue engineering scaffolds, Biomaterials 35(15) (2014) 4477-88.

[23] K.L. Spiller, S. Nassiri, C.E. Witherel, R.R. Anfang, J. Ng, K.R. Nakazawa, T. Yu, G. Vunjak-Novakovic, Sequential delivery of immunomodulatory cytokines to facilitate the

M1-to-M2 transition of macrophages and enhance vascularization of bone scaffolds, Biomaterials 37 (2015) 194-207.

[24] M.J. Crane, J.M. Daley, O. van Houtte, S.K. Brancato, W.L. Henry, Jr., J.E. Albina, The monocyte to macrophage transition in the murine sterile wound, PLoS One 9(1) (2014) e86660.

[25] F.O. Martinez, S. Gordon, M. Locati, A. Mantovani, Transcriptional profiling of the human monocyte-to-macrophage differentiation and polarization: new molecules and patterns of gene expression, J Immunol 177(10) (2006) 7303-11.

[26] A. Mantovani, S. Sozzani, M. Locati, P. Allavena, A. Sica, Macrophage polarization: tumor-associated macrophages as a paradigm for polarized M2 mononuclear phagocytes, Trends Immunol 23(11) (2002) 549-55.

[27] J.R. Krieger, M.E. Ogle, J. McFaline-Figueroa, C.E. Segar, J.S. Temenoff, E.A. Botchwey, Spatially localized recruitment of anti-inflammatory monocytes by SDF-1alpha-releasing hydrogels enhances microvascular network remodeling, Biomaterials 77 (2016) 280-90.

[28] K. Sadtler, K. Estrellas, B.W. Allen, M.T. Wolf, H. Fan, A.J. Tam, C.H. Patel, B.S. Luber, H. Wang, K.R. Wagner, J.D. Powell, F. Housseau, D.M. Pardoll, J.H. Elisseeff, Developing a pro-regenerative biomaterial scaffold microenvironment requires T helper 2 cells, Science 352(6283) (2016) 366-70.

[29] E. Zigmond, C. Varol, J. Farache, E. Elmaliah, A.T. Satpathy, G. Friedlander, M. Mack, N. Shpigel, I.G. Boneca, K.M. Murphy, G. Shakhar, Z. Halpern, S. Jung, Ly6C hi monocytes in the inflamed colon give rise to proinflammatory effector cells and migratory antigen-presenting cells, Immunity 37(6) (2012) 1076-90.

[30] I. Avraham-Davidi, S. Yona, M. Grunewald, L. Landsman, C. Cochain, J.S. Silvestre, H. Mizrahi, M. Faroja, D. Strauss-Ayali, M. Mack, S. Jung, E. Keshet, On-site education of VEGF-recruited monocytes improves their performance as angiogenic and arteriogenic accessory cells, J Exp Med 210(12) (2013) 2611-25.

[31] D. Dal-Secco, J. Wang, Z. Zeng, E. Kolaczkowska, C.H. Wong, B. Petri, R.M. Ransohoff, I.F. Charo, C.N. Jenne, P. Kubes, A dynamic spectrum of monocytes arising from the in situ reprogramming of CCR2+ monocytes at a site of sterile injury, J Exp Med 212(4) (2015) 447-56.

[32] L. Denney, W.L. Kok, S.L. Cole, S. Sanderson, A.J. McMichael, L.P. Ho, Activation of invariant NKT cells in early phase of experimental autoimmune encephalomyelitis results in differentiation of Ly6Chi inflammatory monocyte to M2 macrophages and improved outcome, J Immunol 189(2) (2012) 551-7.

[33] C.E. Olingy, C.L. San Emeterio, M.E. Ogle, J.R. Krieger, A.C. Bruce, D.D. Pfau, B.T. Jordan, S.M. Peirce, E.A. Botchwey, Non-classical monocytes are biased progenitors of wound healing macrophages during soft tissue injury, Sci Rep 7(1) (2017) 447.

[34] F. Geissmann, S. Jung, D.R. Littman, Blood monocytes consist of two principal subsets with distinct migratory properties, Immunity 19(1) (2003) 71-82.

[35] C. Shi, E.G. Pamer, Monocyte recruitment during infection and inflammation, Nat Rev Immunol 11(11) (2011) 762-74.

[36] J.L. Collison, L.M. Carlin, M. Eichmann, F. Geissmann, M. Peakman, Heterogeneity in the Locomotory Behavior of Human Monocyte Subsets over Human Vascular Endothelium In Vitro, J Immunol 195(3) (2015) 1162-70.

[37] C. Auffray, D. Fogg, M. Garfa, G. Elain, O. Join-Lambert, S. Kayal, S. Sarnacki, A. Cumano, G. Lauvau, F. Geissmann, Monitoring of blood vessels and tissues by a population of monocytes with patrolling behavior, Science 317(5838) (2007) 666-70.

[38] N. Ruparelia, J. Godec, R. Lee, J.T. Chai, E. Dall'Armellina, D. McAndrew, J.E. Digby, J.C. Forfar, B.D. Prendergast, R.K. Kharbanda, A.P. Banning, S. Neubauer, C.A. Lygate, K.M. Channon, N.W. Haining, R.P. Choudhury, Acute myocardial infarction activates distinct inflammation and proliferation pathways in circulating monocytes, prior to recruitment, and identified through conserved transcriptional responses in mice and humans, Eur Heart J 36(29) (2015) 1923-34.

[39] F.K. Swirski, M. Nahrendorf, M. Etzrodt, M. Wildgruber, V. Cortez-Retamozo, P. Panizzi, J.L. Figueiredo, R.H. Kohler, A. Chudnovskiy, P. Waterman, E. Aikawa, T.R. Mempel, P. Libby, R. Weissleder, M.J. Pittet, Identification of splenic reservoir monocytes and their deployment to inflammatory sites, Science 325(5940) (2009) 612-6.

[40] K. Rzeniewicz, A. Newe, A. Rey Gallardo, J. Davies, M.R. Holt, A. Patel, G.T. Charras, B. Stramer, C. Molenaar, T.F. Tedder, M. Parsons, A. Ivetic, L-selectin shedding is activated specifically within transmigrating pseudopods of monocytes to regulate cell polarity in vitro, Proc Natl Acad Sci U S A 112(12) (2015) E1461-70.

[41] F. Tacke, D. Alvarez, T.J. Kaplan, C. Jakubzick, R. Spanbroek, J. Llodra, A. Garin, J. Liu, M. Mack, N. van Rooijen, S.A. Lira, A.J. Habenicht, G.J. Randolph, Monocyte subsets differentially employ CCR2, CCR5, and CX3CR1 to accumulate within atherosclerotic plaques, J Clin Invest 117(1) (2007) 185-94.

[42] P. Ancuta, R. Rao, A. Moses, A. Mehle, S.K. Shaw, F.W. Luscinskas, D. Gabuzda, Fractalkine preferentially mediates arrest and migration of CD16+ monocytes, J Exp Med 197(12) (2003) 1701-7.

[43] C.E. Bergmann, I.E. Hoefer, B. Meder, H. Roth, N. van Royen, S.M. Breit, M.M. Jost, S. Aharinejad, S. Hartmann, I.R. Buschmann, Arteriogenesis depends on circulating monocytes and macrophage accumulation and is severely depressed in op/op mice, J Leukoc Biol 80(1) (2006) 59-65.

[44] M.M. Nickerson, J. Song, J.K. Meisner, S. Bajikar, C.W. Burke, C.W. Shuptrine, G.K. Owens, T.C. Skalak, R.J. Price, Bone marrow-derived cell-specific chemokine (C-C motif)

receptor-2 expression is required for arteriolar remodeling, Arterioscler Thromb Vasc Biol 29(11) (2009) 1794-801.

[45] W.D. Ito, M. Arras, B. Winkler, D. Scholz, J. Schaper, W. Schaper, Monocyte chemotactic protein-1 increases collateral and peripheral conductance after femoral artery occlusion, Circ Res 80(6) (1997) 829-37.

[46] M.H. Vries, A. Wagenaar, S.E. Verbruggen, D.G. Molin, I. Dijkgraaf, T.H. Hackeng, M.J. Post, CXCL1 promotes arteriogenesis through enhanced monocyte recruitment into the peri-collateral space, Angiogenesis 18(2) (2015) 163-71.

[47] N. Jetten, S. Verbruggen, M.J. Gijbels, M.J. Post, M.P. De Winther, M.M. Donners, Anti-inflammatory M2, but not pro-inflammatory M1 macrophages promote angiogenesis in vivo, Angiogenesis 17(1) (2014) 109-18.

[48] A. Fantin, J.M. Vieira, G. Gestri, L. Denti, Q. Schwarz, S. Prykhozhij, F. Peri, S.W. Wilson, C. Ruhrberg, Tissue macrophages act as cellular chaperones for vascular anastomosis downstream of VEGF-mediated endothelial tip cell induction, Blood 116(5) (2010) 829-40.

[49] H.H. Outtz, I.W. Tattersall, N.M. Kofler, N. Steinbach, J. Kitajewski, Notch1 controls macrophage recruitment and Notch signaling is activated at sites of endothelial cell anastomosis during retinal angiogenesis in mice, Blood 118(12) (2011) 3436-9.

[50] N.I. Moldovan, P.J. Goldschmidt-Clermont, J. Parker-Thornburg, S.D. Shapiro, P.E. Kolattukudy, Contribution of monocytes/macrophages to compensatory neovascularization: the drilling of metalloelastase-positive tunnels in ischemic myocardium, Circ Res 87(5) (2000) 378-84.

[51] C. Troidl, G. Jung, K. Troidl, J. Hoffmann, H. Mollmann, H. Nef, W. Schaper, C.W. Hamm, T. Schmitz-Rixen, The temporal and spatial distribution of macrophage subpopulations during arteriogenesis, Curr Vasc Pharmacol 11(1) (2013) 5-12.

[52] Y. Takeda, S. Costa, E. Delamarre, C. Roncal, R. Leite de Oliveira, M.L. Squadrito, V. Finisguerra, S. Deschoemaeker, F. Bruyere, M. Wenes, A. Hamm, J. Serneels, J. Magat, T. Bhattacharyya, A. Anisimov, B.F. Jordan, K. Alitalo, P. Maxwell, B. Gallez, Z.W. Zhuang, Y. Saito, M. Simons, M. De Palma, M. Mazzone, Macrophage skewing by Phd2 haplodeficiency prevents ischaemia by inducing arteriogenesis, Nature 479(7371) (2011) 122-6.

[53] M.E. Ogle, L.S. Sefcik, A.O. Awojoodu, N.F. Chiappa, K. Lynch, S. Peirce-Cottler, E.A. Botchwey, Engineering in vivo gradients of sphingosine-1-phosphate receptor ligands for localized microvascular remodeling and inflammatory cell positioning, Acta Biomater 10(11) (2014) 4704-14.

[54] P. Melgar-Lesmes, E.R. Edelman, Monocyte-endothelial cell interactions in the regulation of vascular sprouting and liver regeneration in mouse, J Hepatol 63(4) (2015) 917-25.

[55] M. Grunewald, I. Avraham, Y. Dor, E. Bachar-Lustig, A. Itin, S. Jung, S. Chimenti, L. Landsman, R. Abramovitch, E. Keshet, VEGF-induced adult neovascularization: recruitment, retention, and role of accessory cells, Cell 124(1) (2006) 175-89.

[56] S. Willenborg, T. Lucas, G. van Loo, J.A. Knipper, T. Krieg, I. Haase, B. Brachvogel, M. Hammerschmidt, A. Nagy, N. Ferrara, M. Pasparakis, S.A. Eming, CCR2 recruits an inflammatory macrophage subpopulation critical for angiogenesis in tissue repair, Blood 120(3) (2012) 613-25.

[57] A. Das, C.E. Segar, B.B. Hughley, D.T. Bowers, E.A. Botchwey, The promotion of mandibular defect healing by the targeting of S1P receptors and the recruitment of alternatively activated macrophages, Biomaterials 34(38) (2013) 9853-62.

[58] H. Yin, F. Price, M.A. Rudnicki, Satellite cells and the muscle stem cell niche, Physiol Rev 93(1) (2013) 23-67.

[59] H. Wang, D.W. Melton, L. Porter, Z.U. Sarwar, L.M. McManus, P.K. Shireman, Altered macrophage phenotype transition impairs skeletal muscle regeneration, Am J Pathol 184(4) (2014) 1167-84.

[60] M. Summan, G.L. Warren, R.R. Mercer, R. Chapman, T. Hulderman, N. Van Rooijen, P.P. Simeonova, Macrophages and skeletal muscle regeneration: a clodronate-containing liposome depletion study, Am J Physiol Regul Integr Comp Physiol 290(6) (2006) R1488-95.

[61] M. Saclier, H. Yacoub-Youssef, A.L. Mackey, L. Arnold, H. Ardjoune, M. Magnan, F. Sailhan, J. Chelly, G.K. Pavlath, R. Mounier, M. Kjaer, B. Chazaud, Differentially activated macrophages orchestrate myogenic precursor cell fate during human skeletal muscle regeneration, Stem Cells 31(2) (2013) 384-96.

[62] T. Varga, R. Mounier, A. Horvath, S. Cuvellier, F. Dumont, S. Poliska, H. Ardjoune, G. Juban, L. Nagy, B. Chazaud, Highly Dynamic Transcriptional Signature of Distinct Macrophage Subsets during Sterile Inflammation, Resolution, and Tissue Repair, J Immunol 196(11) (2016) 4771-82.

[63] J. Tonkin, L. Temmerman, R.D. Sampson, E. Gallego-Colon, L. Barberi, D. Bilbao, M.D. Schneider, A. Musaro, N. Rosenthal, Monocyte/Macrophage-derived IGF-1 Orchestrates Murine Skeletal Muscle Regeneration and Modulates Autocrine Polarization, Mol Ther 23(7) (2015) 1189-200.

[64] C.H. Lang, B.J. Krawiec, D. Huber, J.M. McCoy, R.A. Frost, Sepsis and inflammatory insults downregulate IGFBP-5, but not IGFBP-4, in skeletal muscle via a TNF-dependent mechanism, Am J Physiol Regul Integr Comp Physiol 290(4) (2006) R963-72.

[65] D. Costamagna, P. Costelli, M. Sampaolesi, F. Penna, Role of Inflammation in Muscle Homeostasis and Myogenesis, Mediators Inflamm 2015 (2015) 805172.

[66] S.C. Carvalho, L.M. Apolinario, S.M. Matheus, H. Santo Neto, M.J. Marques, EPA protects against muscle damage in the mdx mouse model of Duchenne muscular dystrophy by promoting a shift from the M1 to M2 macrophage phenotype, J Neuroimmunol 264(1-2) (2013) 41-7.

[67] J. Gumucio, M. Flood, J. Harning, A. Phan, S. Roche, E. Lynch, A. Bedi, C. Mendias, T lymphocytes are not required for the development of fatty degeneration after rotator cuff tear, Bone Joint Res 3(9) (2014) 262-72.

[68] J.P. Gumucio, M.E. Davis, J.R. Bradley, P.L. Stafford, C.J. Schiffman, E.B. Lynch, D.R. Claflin, A. Bedi, C.L. Mendias, Rotator cuff tear reduces muscle fiber specific force production and induces macrophage accumulation and autophagy, J Orthop Res 30(12) (2012) 1963-70.

[69] M.R. Davies, L. Lee, B.T. Feeley, H.T. Kim, X. Liu, Lysophosphatidic acid-induced RhoA signaling and prolonged macrophage infiltration worsens fibrosis and fatty infiltration following rotator cuff tears, J Orthop Res (2016).

[70] R. Shechter, O. Miller, G. Yovel, N. Rosenzweig, A. London, J. Ruckh, K.W. Kim, E. Klein, V. Kalchenko, P. Bendel, S.A. Lira, S. Jung, M. Schwartz, Recruitment of beneficial M2 macrophages to injured spinal cord is orchestrated by remote brain choroid plexus, Immunity 38(3) (2013) 555-69.

[71] K.A. Kigerl, J.C. Gensel, D.P. Ankeny, J.K. Alexander, D.J. Donnelly, P.G. Popovich, Identification of two distinct macrophage subsets with divergent effects causing either neurotoxicity or regeneration in the injured mouse spinal cord, J Neurosci 29(43) (2009) 13435-44.

[72] L.V. Blomster, F.H. Brennan, H.W. Lao, D.W. Harle, A.R. Harvey, M.J. Ruitenberg, Mobilisation of the splenic monocyte reservoir and peripheral CX(3)CR1 deficiency adversely affects recovery from spinal cord injury, Exp Neurol 247 (2013) 226-40.

[73] D.P. Vasconcelos, M. Costa, I.F. Amaral, M.A. Barbosa, A.P. Aguas, J.N. Barbosa, Development of an immunomodulatory biomaterial: using resolvin D1 to modulate inflammation, Biomaterials 53 (2015) 566-73.

[74] R. Blazquez, F.M. Sanchez-Margallo, V. Alvarez, A. Uson, J.G. Casado, Surgical meshes coated with mesenchymal stem cells provide an anti-inflammatory environment by a M2 macrophage polarization, Acta Biomater 31 (2016) 221-30.

[75] S.I. Lee, S.R. Jeong, Y.M. Kang, D.H. Han, B.K. Jin, U. Namgung, B.G. Kim, Endogenous expression of interleukin-4 regulates macrophage activation and confines cavity formation after traumatic spinal cord injury, J Neurosci Res 88(11) (2010) 2409-19.

[76] E. Shantsila, L.D. Tapp, B.J. Wrigley, S. Montoro-Garcia, G.Y. Lip, CXCR4 positive and angiogenic monocytes in myocardial infarction, Thromb Haemost 109(2) (2013) 255-62.

[77] E. Shantsila, B. Wrigley, L. Tapp, S. Apostolakis, S. Montoro-Garcia, M.T. Drayson, G.Y. Lip, Immunophenotypic characterization of human monocyte subsets: possible implications for cardiovascular disease pathophysiology, J Thromb Haemost 9(5) (2011) 1056-66.

[78] J.F. Bazan, K.B. Bacon, G. Hardiman, W. Wang, K. Soo, D. Rossi, D.R. Greaves, A. Zlotnik, T.J. Schall, A new class of membrane-bound chemokine with a CX3C motif, Nature 385(6617) (1997) 640-4.

[79] W. Qin, Z. Li, S. Luo, R. Wu, Z. Pei, R. Huang, Exogenous fractalkine enhances proliferation of endothelial cells, promotes migration of endothelial progenitor cells and improves neurological deficits in a rat model of ischemic stroke, Neurosci Lett 569 (2014) 80-4.

[80] R. Cipriani, P. Villa, G. Chece, C. Lauro, A. Paladini, E. Micotti, C. Perego, M.G. De Simoni, B.B. Fredholm, F. Eusebi, C. Limatola, CX3CL1 is neuroprotective in permanent focal cerebral ischemia in rodents, J Neurosci 31(45) (2011) 16327-35.

[81] P. Gaetani, P. Pisano, G. Solinas, P. Colombo, A. Destro, D. Levi, E. Aimar, R. Rodriguez, Y. Baena, P. Allavena, Immunohistohemical expression of the chemokine fractalkine and its receptor in the human brain cortex after severe traumatic brain injury and brain hemorrhage, J Neurosurg Sci 57(1) (2013) 55-62.

[82] M.M. Donohue, K. Cain, D. Zierath, D. Shibata, P.M. Tanzi, K.J. Becker, Higher plasma fractalkine is associated with better 6-month outcome from ischemic stroke, Stroke 43(9) (2012) 2300-6.

[83] A.D. Ellington, J.W. Szostak, Selection Invitro of Single-Stranded-DNA Molecules That Fold into Specific Ligand-Binding Structures, Nature 355(6363) (1992) 850-852.

[84] R.E. Wang, H. Wu, Y. Niu, J. Cai, Improving the stability of aptamers by chemical modification, Curr Med Chem 18(27) (2011) 4126-38.

[85] H.Y. Kong, J. Byun, Nucleic Acid aptamers: new methods for selection, stabilization, and application in biomedical science, Biomol Ther (Seoul) 21(6) (2013) 423-34.

[86] S. Gao, X. Zheng, B. Jiao, L. Wang, Post-SELEX optimization of aptamers, Anal Bioanal Chem 408(17) (2016) 4567-73.

[87] S.A. Lapa, A.V. Chudinov, E.N. Timofeev, The Toolbox for Modified Aptamers, Mol Biotechnol 58(2) (2016) 79-92.

[88] C. Acquah, M.K. Danquah, J.L. Yon, A. Sidhu, C.M. Ongkudon, A review on immobilised aptamers for high throughput biomolecular detection and screening, Anal Chim Acta 888 (2015) 10-8.

[89] M. Vorobyeva, P. Vorobjev, A. Venyaminova, Multivalent Aptamers: Versatile Tools for Diagnostic and Therapeutic Applications, Molecules 21(12) (2016).

[90] J. Hu, M. Ye, Z. Zhou, Aptamers: novel diagnostic and therapeutic tools for diabetes mellitus and metabolic diseases, J Mol Med (Berl) 95(3) (2017) 249-256.

[91] P.P. Hu, Recent Advances in Aptamers Targeting Immune System, Inflammation 40(1) (2017) 295-302.

[92] F. Zheng, Y. Cheng, J. Wang, J. Lu, B. Zhang, Y. Zhao, Z. Gu, Aptamer-functionalized barcode particles for the capture and detection of multiple types of circulating tumor cells, Adv Mater 26(43) (2014) 7333-8.

[93] A. Shastri, L.M. McGregor, Y. Liu, V. Harris, H. Nan, M. Mujica, Y. Vasquez, A. Bhattacharya, Y. Ma, M. Aizenberg, O. Kuksenok, A.C. Balazs, J. Aizenberg, X. He, An aptamer-functionalized chemomechanically modulated biomolecule catch-and-release system, Nat Chem 7(5) (2015) 447-54.

[94] Y.H. Lao, K.K. Phua, K.W. Leong, Aptamer nanomedicine for cancer therapeutics: barriers and potential for translation, ACS Nano 9(3) (2015) 2235-54.

[95] J.R. Kanwar, K. Roy, N.G. Maremanda, K. Subramanian, R.N. Veedu, R. Bawa, R.K. Kanwar, Nucleic acid-based aptamers: applications, development and clinical trials, Curr Med Chem 22(21) (2015) 2539-57.

[96] J. Zhou, J. Rossi, Aptamers as targeted therapeutics: current potential and challenges, Nat Rev Drug Discov 16(3) (2017) 181-202.

[97] M.M. Pabon, A.D. Bachstetter, C.E. Hudson, C. Gemma, P.C. Bickford, CX3CL1 reduces neurotoxicity and microglial activation in a rat model of Parkinson's disease, J Neuroinflammation 8 (2011) 9.

[98] M. He, S.M. Moochhala, S. Adhikari, M. Bhatia, Administration of exogenous fractalkine, a CX3C chemokine, is capable of modulating inflammatory response in cecal ligation and puncture-induced sepsis, Shock 31(1) (2009) 33-9.

[99] J. Slusarczyk, E. Trojan, K. Wydra, K. Glombik, K. Chamera, M. Kucharczyk, B. Budziszewska, M. Kubera, W. Lason, M. Filip, A. Basta-Kaim, Beneficial impact of intracerebroventricular fractalkine administration on behavioral and biochemical changes induced by prenatal stress in adult rats: Possible role of NLRP3 inflammasome pathway, Biochem Pharmacol 113 (2016) 45-56.

[100] L.R. Brown, Commercial challenges of protein drug delivery, Expert Opin Drug Deliv 2(1) (2005) 29-42.

[101] W.R. Strohl, Fusion Proteins for Half-Life Extension of Biologics as a Strategy to Make Biobetters, BioDrugs 29(4) (2015) 215-39.

[102] M. Werle, A. Bernkop-Schnurch, Strategies to improve plasma half life time of peptide and protein drugs, Amino Acids 30(4) (2006) 351-67.

[103] Y. Vugmeyster, X. Xu, F.P. Theil, L.A. Khawli, M.W. Leach, Pharmacokinetics and toxicology of therapeutic proteins: Advances and challenges, World J Biol Chem 3(4) (2012) 73-92.

[104] R.J. Sola, K. Griebenow, Glycosylation of therapeutic proteins: an effective strategy to optimize efficacy, BioDrugs 24(1) (2010) 9-21.

[105] H. Schellekens, Factors influencing the immunogenicity of therapeutic proteins, Nephrol Dial Transplant 20 Suppl 6 (2005) vi3-9.

[106] H. Schellekens, Immunogenicity of therapeutic proteins: clinical implications and future prospects, Clin Ther 24(11) (2002) 1720-40; discussion 1719.

[107] A. Smith, H. Manoli, S. Jaw, K. Frutoz, A.L. Epstein, L.A. Khawli, F.P. Theil, Unraveling the Effect of Immunogenicity on the PK/PD, Efficacy, and Safety of Therapeutic Proteins, J Immunol Res 2016 (2016) 2342187.

[108] Y. Omatsu, M. Seike, T. Sugiyama, T. Kume, T. Nagasawa, Foxc1 is a critical regulator of haematopoietic stem/progenitor cell niche formation, Nature 508(7497) (2014) 536-40.

[109] S. Otsuru, K. Tamai, T. Yamazaki, H. Yoshikawa, Y. Kaneda, Circulating bone marrow-derived osteoblast progenitor cells are recruited to the bone-forming site by the CXCR4/stromal cell-derived factor-1 pathway, Stem Cells 26(1) (2008) 223-34.

[110] F. Zemani, J.S. Silvestre, F. Fauvel-Lafeve, A. Bruel, J. Vilar, I. Bieche, I. Laurendeau, I. Galy-Fauroux, A.M. Fischer, C. Boisson-Vidal, Ex vivo priming of endothelial progenitor cells with SDF-1 before transplantation could increase their proangiogenic potential, Arterioscler Thromb Vasc Biol 28(4) (2008) 644-50.

[111] K. Stark, A. Eckart, S. Haidari, A. Tirniceriu, M. Lorenz, M.L. von Bruhl, F. Gartner, A.G. Khandoga, K.R. Legate, R. Pless, I. Hepper, K. Lauber, B. Walzog, S. Massberg, Capillary and arteriolar pericytes attract innate leukocytes exiting through venules and 'instruct' them with pattern-recognition and motility programs, Nat Immunol 14(1) (2013) 41-51.

[112] J. Ehling, M. Bartneck, X. Wei, F. Gremse, V. Fech, D. Mockel, C. Baeck, K. Hittatiya, D. Eulberg, T. Luedde, F. Kiessling, C. Trautwein, T. Lammers, F. Tacke, CCL2-dependent infiltrating macrophages promote angiogenesis in progressive liver fibrosis, Gut 63(12) (2014) 1960-71.

[113] M.H. Hettiaratchi, T. Miller, J.S. Temenoff, R.E. Guldberg, T.C. McDevitt, Heparin microparticle effects on presentation and bioactivity of bone morphogenetic protein-2, Biomaterials 35(25) (2014) 7228-38.

[114] S.P. Seto, T. Miller, J.S. Temenoff, Effect of selective heparin desulfation on preservation of bone morphogenetic protein-2 bioactivity after thermal stress, Bioconjug Chem 26(2) (2015) 286-93.

[115] L.E. Tellier, T. Miller, T.C. McDevitt, J.S. Temenoff, Hydrolysis and Sulfation Pattern Effects on Release of Bioactive Bone Morphogenetic Protein-2 from Heparin-Based Microparticles, J Mater Chem B Mater Biol Med 3(40) (2015) 8001-8009.

[116] R. Sadir, F. Baleux, A. Grosdidier, A. Imberty, H. Lortat-Jacob, Characterization of the stromal cell-derived factor-1alpha-heparin complex, J Biol Chem 276(11) (2001) 8288-96.

[117] T. Miller, M.C. Goude, T.C. McDevitt, J.S. Temenoff, Molecular engineering of glycosaminoglycan chemistry for biomolecule delivery, Acta Biomater 10(4) (2014) 1705-19.

[118] Y. Inoue, K. Nagasawa, Selective N-desulfation of heparin with dimethyl sulfoxide containing water or methanol, Carbohydr Res 46(1) (1976) 87-95.

[119] M. Hricovini, M. Guerrini, A. Bisio, G. Torri, A. Naggi, B. Casu, Active conformations of glycosaminoglycans. NMR determination of the conformation of heparin sequences complexed with antithrombin and fibroblast growth factors in solution, Semin Thromb Hemost 28(4) (2002) 325-34.

[120] L. Levy, F.J. Petracek, Chemical and pharmacological studies on N-resulfated heparin, Proc Soc Exp Biol Med 109 (1962) 901-5.

[121] S. Nakamura, M. Ishihara, K. Obara, K. Masuoka, T. Ishizuka, Y. Kanatani, B. Takase, T. Matsui, H. Hattori, T. Sato, Y. Kariya, T. Maehara, Controlled release of fibroblast growth factor-2 from an injectable 6-O-desulfated heparin hydrogel and subsequent effect on in vivo vascularization, J Biomed Mater Res A 78(2) (2006) 364-71.

[122] S. Roy, H. Lai, R. Zouaoui, J. Duffner, H. Zhou, P.J. L, G. Zhao, T. Ganguly, T.K. Kishimoto, G. Venkataraman, Bioactivity screening of partially desulfated low-molecular-weight heparins: a structure/activity relationship study, Glycobiology 21(9) (2011) 1194-205.

[123] A. Hawe, W. Friess, Stabilization of a hydrophobic recombinant cytokine by human serum albumin, J Pharm Sci 96(11) (2007) 2987-99.

[124] M. Zamani, M.P. Prabhakaran, E.S. Thian, S. Ramakrishna, Controlled delivery of stromal derived factor-1alpha from poly lactic-co-glycolic acid core-shell particles to recruit mesenchymal stem cells for cardiac regeneration, J Colloid Interface Sci 451 (2015) 144-52.

[125] B. Waybrant, T.R. Pearce, P. Wang, S. Sreevatsan, E. Kokkoli, Development and characterization of an aptamer binding ligand of fractalkine using domain targeted SELEX, Chem Commun (Camb) 48(80) (2012) 10043-5.

[126] B. Waybrant, T.R. Pearce, E. Kokkoli, Effect of polyethylene glycol, alkyl, and oligonucleotide spacers on the binding, secondary structure, and self-assembly of fractalkine binding FKN-S2 aptamer-amphiphiles, Langmuir 30(25) (2014) 7465-74.

[127] M. Rancan, N. Bye, V.I. Otto, O. Trentz, T. Kossmann, S. Frentzel, M.C. Morganti-Kossmann, The chemokine fractalkine in patients with severe traumatic brain injury and a mouse model of closed head injury, J Cereb Blood Flow Metab 24(10) (2004) 1110-8.

[128] L.M. Carlin, C. Auffray, F. Geissmann, Measuring intravascular migration of mouse Ly6C(low) monocytes in vivo using intravital microscopy, Curr Protoc Immunol Chapter 14 (2013) Unit 14 33 1-16.

[129] A.C. Bruce, M.R. Kelly-Goss, J.L. Heuslein, J.K. Meisner, R.J. Price, S.M. Peirce, Monocytes are recruited from venules during arteriogenesis in the murine spinotrapezius ligation model, Arterioscler Thromb Vasc Biol 34(9) (2014) 2012-22.

[130] C.L. San Emeterio, C.E. Olingy, Y. Chu, E.A. Botchwey, Selective recruitment of non-classical monocytes promotes skeletal muscle repair, Biomaterials 117 (2017) 32-43.

[131] Y. Ishida, J.L. Gao, P.M. Murphy, Chemokine receptor CX3CR1 mediates skin wound healing by promoting macrophage and fibroblast accumulation and function, J Immunol 180(1) (2008) 569-79.

[132] I. Francos-Quijorna, J. Amo-Aparicio, A. Martinez-Muriana, R. Lopez-Vales, IL-4 drives microglia and macrophages toward a phenotype conducive for tissue repair and functional recovery after spinal cord injury, Glia 64(12) (2016) 2079-2092.

[133] A. Das, C.E. Segar, Y. Chu, T.W. Wang, Y. Lin, C. Yang, X. Du, R.C. Ogle, Q. Cui, E.A. Botchwey, Bioactive lipid coating of bone allografts directs engraftment and fate determination of bone marrow-derived cells in rat GFP chimeras, Biomaterials 64 (2015) 98-107.

[134] I. Hilgendorf, L.M. Gerhardt, T.C. Tan, C. Winter, T.A. Holderried, B.G. Chousterman, Y. Iwamoto, R. Liao, A. Zirlik, M. Scherer-Crosbie, C.C. Hedrick, P. Libby, M. Nahrendorf, R. Weissleder, F.K. Swirski, Ly-6Chigh monocytes depend on Nr4a1 to balance both inflammatory and reparative phases in the infarcted myocardium, Circ Res 114(10) (2014) 1611-22.

[135] J.C. Ryu, B.P. Davidson, A. Xie, Y. Qi, D. Zha, J.T. Belcik, E.S. Caplan, J.M. Woda, C.C. Hedrick, R.N. Hanna, N. Lehman, Y. Zhao, A. Ting, J.R. Lindner, Molecular imaging of the paracrine proangiogenic effects of progenitor cell therapy in limb ischemia, Circulation 127(6) (2013) 710-9.

[136] J. Li, Y. Liu, H. Xu, Q. Fu, Nanoparticle-Delivered IRF5 siRNA Facilitates M1 to M2 Transition, Reduces Demyelination and Neurofilament Loss, and Promotes Functional Recovery After Spinal Cord Injury in Mice, Inflammation 39(5) (2016) 1704-17.

[137] M.J. Lee, J. Kim, K.I. Lee, J.M. Shin, J.I. Chae, H.M. Chung, Enhancement of wound healing by secretory factors of endothelial precursor cells derived from human embryonic stem cells, Cytotherapy 13(2) (2011) 165-78.

[138] D.D. Dickey, P.H. Giangrande, Oligonucleotide aptamers: A next-generation technology for the capture and detection of circulating tumor cells, Methods 97 (2016) 94-103.

[139] L.A. Truman, C.A. Ford, M. Pasikowska, J.D. Pound, S.J. Wilkinson, I.E. Dumitriu, L. Melville, L.A. Melrose, C.A. Ogden, R. Nibbs, G. Graham, C. Combadiere, C.D. Gregory, CX3CL1/fractalkine is released from apoptotic lymphocytes to stimulate macrophage chemotaxis, Blood 112(13) (2008) 5026-36.

[140] J.C. Gevrey, B.M. Isaac, D. Cox, Syk is required for monocyte/macrophage chemotaxis to CX3CL1 (Fractalkine), J Immunol 175(6) (2005) 3737-45.

[141] G.E. White, E. McNeill, K.M. Channon, D.R. Greaves, Fractalkine promotes human monocyte survival via a reduction in oxidative stress, Arterioscler Thromb Vasc Biol 34(12) (2014) 2554-62.

[142] K.R. Karlmark, H.W. Zimmermann, C. Roderburg, N. Gassler, H.E. Wasmuth, T. Luedde, C. Trautwein, F. Tacke, The fractalkine receptor CX(3)CR1 protects against liver fibrosis by controlling differentiation and survival of infiltrating hepatic monocytes, Hepatology 52(5) (2010) 1769-82.

[143] C.A. Panek, M.V. Ramos, M.P. Mejias, M.J. Abrey-Recalde, R.J. Fernandez-Brando, M.S. Gori, G.V. Salamone, M.S. Palermo, Differential expression of the fractalkine chemokine receptor (CX3CR1) in human monocytes during differentiation, Cell Mol Immunol 12(6) (2015) 669-80.

[144] T. Imai, K. Hieshima, C. Haskell, M. Baba, M. Nagira, M. Nishimura, M. Kakizaki, S. Takagi, H. Nomiyama, T.J. Schall, O. Yoshie, Identification and molecular characterization of fractalkine receptor CX3CR1, which mediates both leukocyte migration and adhesion, Cell 91(4) (1997) 521-30.

[145] Y. Pan, C. Lloyd, H. Zhou, S. Dolich, J. Deeds, J.A. Gonzalo, J. Vath, M. Gosselin, J. Ma, B. Dussault, E. Woolf, G. Alperin, J. Culpepper, J.C. Gutierrez-Ramos, D. Gearing, Neurotactin, a membrane-anchored chemokine upregulated in brain inflammation, Nature 387(6633) (1997) 611-7.

[146] B. Liu, J. Zhang, J. Liao, J. Liu, K. Chen, G. Tong, P. Yuan, Z. Liu, Y. Pu, H. Liu, Aptamer-functionalized nanoparticles for drug delivery, J Biomed Nanotechnol 10(11) (2014) 3189-203.

[147] M.Z. Ratajczak, C.H. Kim, A. Abdel-Latif, G. Schneider, M. Kucia, A.J. Morris, M.J. Laughlin, J. Ratajczak, A novel perspective on stem cell homing and mobilization: review on bioactive lipids as potent chemoattractants and cationic peptides as underappreciated modulators of responsiveness to SDF-1 gradients, Leukemia 26(1) (2012) 63-72.

[148] M.Z. Ratajczak, E. Zuba-Surma, M. Kucia, R. Reca, W. Wojakowski, J. Ratajczak, The pleiotropic effects of the SDF-1-CXCR4 axis in organogenesis, regeneration and tumorigenesis, Leukemia 20(11) (2006) 1915-24.

[149] M. Arras, W.D. Ito, D. Scholz, B. Winkler, J. Schaper, W. Schaper, Monocyte activation in angiogenesis and collateral growth in the rabbit hindlimb, J Clin Invest 101(1) (1998) 40-50.

[150] M.R. Battig, Y. Huang, N. Chen, Y. Wang, Aptamer-functionalized superporous hydrogels for sequestration and release of growth factors regulated via molecular recognition, Biomaterials 35(27) (2014) 8040-8.

[151] L.S. Sefcik, C.E. Aronin, A.O. Awojoodu, S.J. Shin, F. Mac Gabhann, T.L. MacDonald, B.R. Wamhoff, K.R. Lynch, S.M. Peirce, E.A. Botchwey, Selective activation of sphingosine 1-phosphate receptors 1 and 3 promotes local microvascular network growth, Tissue Eng Part A 17(5-6) (2011) 617-29.

[152] L.S. Sefcik, C.E. Petrie Aronin, K.A. Wieghaus, E.A. Botchwey, Sustained release of sphingosine 1-phosphate for therapeutic arteriogenesis and bone tissue engineering, Biomaterials 29(19) (2008) 2869-77.

[153] C. Petrie, S. Tholpady, R. Ogle, E. Botchwey, Proliferative capacity and osteogenic potential of novel dura mater stem cells on poly-lactic-co-glycolic acid, J Biomed Mater Res A 85(1) (2008) 61-71.

[154] S.L. Lin, A.P. Castano, B.T. Nowlin, M.L. Lupher, Jr., J.S. Duffield, Bone marrow Ly6Chigh monocytes are selectively recruited to injured kidney and differentiate into functionally distinct populations, J Immunol 183(10) (2009) 6733-43.

[155] L. Arnold, H. Perrin, C.B. de Chanville, M. Saclier, P. Hermand, L. Poupel, E. Guyon, F. Licata, W. Carpentier, J. Vilar, R. Mounier, B. Chazaud, N. Benhabiles, A. Boissonnas, B. Combadiere, C. Combadiere, CX3CR1 deficiency promotes muscle repair and regeneration by enhancing macrophage ApoE production, Nat Commun 6 (2015) 8972.

[156] S. Nassiri, I. Zakeri, M.S. Weingarten, K.L. Spiller, Relative Expression of Proinflammatory and Antiinflammatory Genes Reveals Differences between Healing and Nonhealing Human Chronic Diabetic Foot Ulcers, J Invest Dermatol 135(6) (2015) 1700-3.

[157] I. Petit, D. Jin, S. Rafii, The SDF-1-CXCR4 signaling pathway: a molecular hub modulating neo-angiogenesis, Trends Immunol 28(7) (2007) 299-307.

[158] D.H. Walter, U. Rochwalsky, J. Reinhold, F. Seeger, A. Aicher, C. Urbich, I. Spyridopoulos, J. Chun, V. Brinkmann, P. Keul, B. Levkau, A.M. Zeiher, S. Dimmeler, J. Haendeler, Sphingosine-1-phosphate stimulates the functional capacity of progenitor cells by activation of the CXCR4-dependent signaling pathway via the S1P3 receptor, Arterioscler Thromb Vasc Biol 27(2) (2007) 275-82.

[159] J.-P.P. Lai, Jagan; Men, Angela, Clinical Pharmacology and Biopharmaceutics Review (Fingolimod), Center for Drug Evaluation and Research (2010).

[160] E.L. Gautier, T. Shay, J. Miller, M. Greter, C. Jakubzick, S. Ivanov, J. Helft, A. Chow, K.G. Elpek, S. Gordonov, A.R. Mazloom, A. Ma'ayan, W.J. Chua, T.H. Hansen, S.J. Turley, M. Merad, G.J. Randolph, C. Immunological Genome, Gene-expression profiles and transcriptional regulatory pathways that underlie the identity and diversity of mouse tissue macrophages, Nat Immunol 13(11) (2012) 1118-28.

[161] S. Tamoutounour, M. Guilliams, F. Montanana Sanchis, H. Liu, D. Terhorst, C. Malosse, E. Pollet, L. Ardouin, H. Luche, C. Sanchez, M. Dalod, B. Malissen, S. Henri, Origins and functional specialization of macrophages and of conventional and monocyte-derived dendritic cells in mouse skin, Immunity 39(5) (2013) 925-38.

[162] S. Jung, J. Aliberti, P. Graemmel, M.J. Sunshine, G.W. Kreutzberg, A. Sher, D.R. Littman, Analysis of fractalkine receptor CX(3)CR1 function by targeted deletion and green fluorescent protein reporter gene insertion, Mol Cell Biol 20(11) (2000) 4106-14.

[163] M. Heil, T. Ziegelhoeffer, S. Wagner, B. Fernandez, A. Helisch, S. Martin, S. Tribulova, W.A. Kuziel, G. Bachmann, W. Schaper, Collateral artery growth (arteriogenesis) after experimental arterial occlusion is impaired in mice lacking CC-chemokine receptor-2, Circ Res 94(5) (2004) 671-7.

[164] S. Galvani, M. Sanson, V.A. Blaho, S.L. Swendeman, H. Obinata, H. Conger, B. Dahlback, M. Kono, R.L. Proia, J.D. Smith, T. Hla, HDL-bound sphingosine 1-phosphate acts as a biased agonist for the endothelial cell receptor S1P1 to limit vascular inflammation, Sci Signal 8(389) (2015) ra79.

[165] P.J. Wermuth, S.A. Jimenez, The significance of macrophage polarization subtypes for animal models of tissue fibrosis and human fibrotic diseases, Clin Transl Med 4 (2015) 2.

[166] A. Hamm, L. Veschini, Y. Takeda, S. Costa, E. Delamarre, M.L. Squadrito, A.T. Henze, M. Wenes, J. Serneels, F. Pucci, C. Roncal, A. Anisimov, K. Alitalo, M. De Palma, M. Mazzone, PHD2 regulates arteriogenic macrophages through TIE2 signalling, EMBO Mol Med 5(6) (2013) 843-57.

[167] E. Fung, A. Helisch, Macrophages in collateral arteriogenesis, Front Physiol 3 (2012) 353.

[168] G. Christoffersson, E. Vagesjo, J. Vandooren, M. Liden, S. Massena, R.B. Reinert, M. Brissova, A.C. Powers, G. Opdenakker, M. Phillipson, VEGF-A recruits a proangiogenic MMP-9-delivering neutrophil subset that induces angiogenesis in transplanted hypoxic tissue, Blood 120(23) (2012) 4653-62.

[169] H. Minagawa, N. Yamamoto, H. Abe, M. Fukuda, N. Seki, K. Kikuchi, H. Kijima, E. Itoi, Prevalence of symptomatic and asymptomatic rotator cuff tears in the general population: From mass-screening in one village, J Orthop 10(1) (2013) 8-12.

[170] J. Ozaki, S. Fujimoto, Y. Nakagawa, K. Masuhara, S. Tamai, Tears of the rotator cuff of the shoulder associated with pathological changes in the acromion. A study in cadavera, J Bone Joint Surg Am 70(8) (1988) 1224-30.

[171] K. Yamaguchi, K. Ditsios, W.D. Middleton, C.F. Hildebolt, L.M. Galatz, S.A. Teefey, The demographic and morphological features of rotator cuff disease. A comparison of asymptomatic and symptomatic shoulders, J Bone Joint Surg Am 88(8) (2006) 1699-704.

[172] S.N. Sambandam, V. Khanna, A. Gul, V. Mounasamy, Rotator cuff tears: An evidence based approach, World J Orthop 6(11) (2015) 902-18.

[173] J. Hsu, J.D. Keener, Natural History of Rotator Cuff Disease and Implications on Management, Oper Tech Orthop 25(1) (2015) 2-9.

[174] S. Tempelhof, S. Rupp, R. Seil, Age-related prevalence of rotator cuff tears in asymptomatic shoulders, J Shoulder Elbow Surg 8(4) (1999) 296-9.

[175] J.N. Gladstone, J.Y. Bishop, I.K. Lo, E.L. Flatow, Fatty infiltration and atrophy of the rotator cuff do not improve after rotator cuff repair and correlate with poor functional outcome, Am J Sports Med 35(5) (2007) 719-28.

[176] C. Gerber, A.G. Schneeberger, H. Hoppeler, D.C. Meyer, Correlation of atrophy and fatty infiltration on strength and integrity of rotator cuff repairs: a study in thirteen patients, J Shoulder Elbow Surg 16(6) (2007) 691-6.

[177] C. Jakubzick, E.L. Gautier, S.L. Gibbings, D.K. Sojka, A. Schlitzer, T.E. Johnson, S. Ivanov, Q. Duan, S. Bala, T. Condon, N. van Rooijen, J.R. Grainger, Y. Belkaid, A. Ma'ayan, D.W. Riches, W.M. Yokoyama, F. Ginhoux, P.M. Henson, G.J. Randolph, Minimal differentiation of classical monocytes as they survey steady-state tissues and transport antigen to lymph nodes, Immunity 39(3) (2013) 599-610.

[178] C. Sunderkotter, T. Nikolic, M.J. Dillon, N. Van Rooijen, M. Stehling, D.A. Drevets, P.J. Leenen, Subpopulations of mouse blood monocytes differ in maturation stage and inflammatory response, J Immunol 172(7) (2004) 4410-7.

[179] N. van Rooijen, E. van Kesteren-Hendrikx, Clodronate liposomes: perspectives in research and therapeutics, J Liposome Res 12(1-2) (2002) 81-94.

[180] S.P. Samagh, E.J. Kramer, G. Melkus, D. Laron, B.M. Bodendorfer, K. Natsuhara, H.T. Kim, X. Liu, B.T. Feeley, MRI quantification of fatty infiltration and muscle atrophy in a mouse model of rotator cuff tears, J Orthop Res 31(3) (2013) 421-6.

[181] M.R. Davies, X. Liu, L. Lee, D. Laron, A.Y. Ning, H.T. Kim, B.T. Feeley, TGF-beta Small Molecule Inhibitor SB431542 Reduces Rotator Cuff Muscle Fibrosis and Fatty Infiltration By Promoting Fibro/Adipogenic Progenitor Apoptosis, PLoS One 11(5) (2016) e0155486.

[182] X. Liu, D. Laron, K. Natsuhara, G. Manzano, H.T. Kim, B.T. Feeley, A mouse model of massive rotator cuff tears, J Bone Joint Surg Am 94(7) (2012) e41.

[183] A. Das, D.A. Barker, T. Wang, C.M. Lau, Y. Lin, E.A. Botchwey, Delivery of bioactive lipids from composite microgel-microsphere injectable scaffolds enhances stem cell recruitment and skeletal repair, PLoS One 9(7) (2014) e101276.

[184] J. Bishop, S. Klepps, I.K. Lo, J. Bird, J.N. Gladstone, E.L. Flatow, Cuff integrity after arthroscopic versus open rotator cuff repair: a prospective study, J Shoulder Elbow Surg 15(3) (2006) 290-9.

[185] S. Klepps, J. Bishop, J. Lin, O. Cahlon, A. Strauss, P. Hayes, E.L. Flatow, Prospective evaluation of the effect of rotator cuff integrity on the outcome of open rotator cuff repairs, Am J Sports Med 32(7) (2004) 1716-22.

[186] L.M. Galatz, C.M. Ball, S.A. Teefey, W.D. Middleton, K. Yamaguchi, The outcome and repair integrity of completely arthroscopically repaired large and massive rotator cuff tears, J Bone Joint Surg Am 86-A(2) (2004) 219-24.

[187] J.P. Iannotti, M.J. Codsi, Y.W. Kwon, K. Derwin, J. Ciccone, J.J. Brems, Porcine small intestine submucosa augmentation of surgical repair of chronic two-tendon rotator cuff tears. A randomized, controlled trial, J Bone Joint Surg Am 88(6) (2006) 1238-44.

[188] S.G. Sclamberg, J.E. Tibone, J.M. Itamura, S. Kasraeian, Six-month magnetic resonance imaging follow-up of large and massive rotator cuff repairs reinforced with porcine small intestinal submucosa, J Shoulder Elbow Surg 13(5) (2004) 538-41.

[189] T. Thangarajah, C.J. Pendegrass, S. Shahbazi, S. Lambert, S. Alexander, G.W. Blunn, Augmentation of Rotator Cuff Repair With Soft Tissue Scaffolds, Orthop J Sports Med 3(6) (2015) 2325967115587495.

[190] F. Leuschner, P.J. Rauch, T. Ueno, R. Gorbatov, B. Marinelli, W.W. Lee, P. Dutta, Y. Wei, C. Robbins, Y. Iwamoto, B. Sena, A. Chudnovskiy, P. Panizzi, E. Keliher, J.M. Higgins, P. Libby, M.A. Moskowitz, M.J. Pittet, F.K. Swirski, R. Weissleder, M. Nahrendorf, Rapid monocyte kinetics in acute myocardial infarction are sustained by extramedullary monocytopoiesis, J Exp Med 209(1) (2012) 123-37.

[191] N. Dumont, J. Frenette, Macrophages protect against muscle atrophy and promote muscle recovery in vivo and in vitro: a mechanism partly dependent on the insulin-like growth factor-1 signaling molecule, Am J Pathol 176(5) (2010) 2228-35.

[192] K. Mojumdar, F. Liang, C. Giordano, C. Lemaire, G. Danialou, T. Okazaki, J. Bourdon, M. Rafei, J. Galipeau, M. Divangahi, B.J. Petrof, Inflammatory monocytes promote progression of Duchenne muscular dystrophy and can be therapeutically targeted via CCR2, EMBO Mol Med 6(11) (2014) 1476-92.

[193] J.R. Krieger, L.E. Tellier, M.T. Ollukaren, J.S. Temenoff, E.A. Botchwey, Quantitative Analysis of Immune Cell Subset Infiltration of Supraspinatus Muscle After

Severe Rotator Cuff Injury, Regenerative Engineering and Translational Medicine (2017) 1-12.

[194] W. Zhao, X. Wang, R.M. Ransohoff, L. Zhou, CCR2 deficiency does not provide sustained improvement of muscular dystrophy in mdx5cv mice, FASEB J 31(1) (2017) 35-46.

[195] B. Deng, M. Wehling-Henricks, S.A. Villalta, Y. Wang, J.G. Tidball, IL-10 triggers changes in macrophage phenotype that promote muscle growth and regeneration, J Immunol 189(7) (2012) 3669-80.

[196] T.T. Lau, D.A. Wang, Stromal cell-derived factor-1 (SDF-1): homing factor for engineered regenerative medicine, Expert Opin Biol Ther 11(2) (2011) 189-97.

[197] L. Pelosi, C. Giacinti, C. Nardis, G. Borsellino, E. Rizzuto, C. Nicoletti, F. Wannenes, L. Battistini, N. Rosenthal, M. Molinaro, A. Musaro, Local expression of IGF-1 accelerates muscle regeneration by rapidly modulating inflammatory cytokines and chemokines, FASEB J 21(7) (2007) 1393-402.

[198] A.S. Brack, M.J. Conboy, S. Roy, M. Lee, C.J. Kuo, C. Keller, T.A. Rando, Increased Wnt signaling during aging alters muscle stem cell fate and increases fibrosis, Science 317(5839) (2007) 807-10.

[199] C.J. Mann, E. Perdiguero, Y. Kharraz, S. Aguilar, P. Pessina, A.L. Serrano, P. Munoz-Canoves, Aberrant repair and fibrosis development in skeletal muscle, Skelet Muscle 1(1) (2011) 21.

[200] M. Guthridge, M. Wilson, J. Cowling, J. Bertolini, M.T. Hearn, The role of basic fibroblast growth factor in skeletal muscle regeneration, Growth Factors 6(1) (1992) 53-63.

[201] E. Abdel-Salam, I. Abdel-Meguid, S.S. Korraa, Markers of degeneration and regeneration in Duchenne muscular dystrophy, Acta Myol 28(3) (2009) 94-100.

[202] J.E. Anderson, L. Liu, E. Kardami, Distinctive patterns of basic fibroblast growth factor (bFGF) distribution in degenerating and regenerating areas of dystrophic (mdx) striated muscles, Dev Biol 147(1) (1991) 96-109.

[203] J.G. Costouros, M. Porramatikul, D.T. Lie, J.J. Warner, Reversal of suprascapular neuropathy following arthroscopic repair of massive supraspinatus and infraspinatus rotator cuff tears, Arthroscopy 23(11) (2007) 1152-61.

[204] W.J. Mallon, R.J. Wilson, C.J. Basamania, The association of suprascapular neuropathy with massive rotator cuff tears: a preliminary report, J Shoulder Elbow Surg 15(4) (2006) 395-8.

[205] L.L. Shi, R.E. Boykin, A. Lin, J.J. Warner, Association of suprascapular neuropathy with rotator cuff tendon tears and fatty degeneration, J Shoulder Elbow Surg 23(3) (2014) 339-46.

[206] V.B. Vad, D. Southern, R.F. Warren, D.W. Altchek, D. Dines, Prevalence of peripheral neurologic injuries in rotator cuff tears with atrophy, J Shoulder Elbow Surg 12(4) (2003) 333-6.

[207] P. Collin, T. Treseder, A. Ladermann, T. Benkalfate, R. Mourtada, O. Courage, L. Favard, Neuropathy of the suprascapular nerve and massive rotator cuff tears: a prospective electromyographic study, J Shoulder Elbow Surg 23(1) (2014) 28-34.

[208] M.J. Albritton, R.D. Graham, R.S. Richards, 2nd, C.J. Basamania, An anatomic study of the effects on the suprascapular nerve due to retraction of the supraspinatus muscle after a rotator cuff tear, J Shoulder Elbow Surg 12(5) (2003) 497-500.

[209] L.E. Leclere, L.L. Shi, A. Lin, P. Yannopoulos, L.D. Higgins, J.J. Warner, Complete Fatty infiltration of intact rotator cuffs caused by suprascapular neuropathy, Arthroscopy 30(5) (2014) 639-44.

[210] E. Cho, Y. Zhang, A. Pruznak, H.M. Kim, Effect of tamoxifen on fatty degeneration and atrophy of rotator cuff muscles in chronic rotator cuff tear: An animal model study, J Orthop Res 33(12) (2015) 1846-53.

[211] P.J. Atherton, P.L. Greenhaff, S.M. Phillips, S.C. Bodine, C.M. Adams, C.H. Lang, Control of skeletal muscle atrophy in response to disuse: clinical/preclinical contentions and fallacies of evidence, Am J Physiol Endocrinol Metab 311(3) (2016) E594-604.

[212] F. Yajid, J.G. Mercier, B.M. Mercier, H. Dubouchaud, C. Prefaut, Effects of 4 wk of hindlimb suspension on skeletal muscle mitochondrial respiration in rats, J Appl Physiol (1985) 84(2) (1998) 479-85.

[213] D. Burzyn, W. Kuswanto, D. Kolodin, J.L. Shadrach, M. Cerletti, Y. Jang, E. Sefik, T.G. Tan, A.J. Wagers, C. Benoist, D. Mathis, A special population of regulatory T cells potentiates muscle repair, Cell 155(6) (2013) 1282-95.

[214] X.H. Wang, W.E. Mitch, Mechanisms of muscle wasting in chronic kidney disease, Nat Rev Nephrol 10(9) (2014) 504-16.

[215] M.E. Ogle, J.R. Krieger, L.E. Tellier, J. McFaline-Figueroa, J.S. Temenoff, E.A. Botchwey, Dual Affinity Heparin-Based Hydrogels Achieve Pro-Regenerative Immunomodulation and Microvascular Remodeling, ACS Biomaterials Science & Engineering (2017).